

# Mechanism of Abrasion in Nonwovens and Strategies for Abrasion Resilient Nonwovens

by  
Dandan Wang

A dissertation submitted in partial fulfillment  
of the requirements for the degree of  
Doctor of Philosophy  
(Materials Science and Engineering)  
in The University of Michigan  
2020

Doctoral Committee:

Professor Wei Lu, Co-chair  
Professor Michael Thouless, Co-chair  
Professor James Barber  
Professor Greg Hulbert  
Assistant Professor Liang Qi

Dandan Wang  
dandanw@umich.edu  
ORCID iD: 0000-0002-8486-4273  
© Dandan Wang 2020

To my parents and friends

## ACKNOWLEDGEMENTS

I would like to thank my adviser Professor Michael Thouless, Professor James Barber and Professor Wei Lu. They are smart and earnest researchers in the area of mechanics and materials science. More importantly, they are good advisors to help young researcher like me to start my career. I am so lucky to have them to guide me in different perspectives. I still remember the first time I talked to Professor Thouless. He talked about his previous research and also his projects that I could work on. There was one this concern that I was from Materials Science and I did not have too much background in Solid Mechanics. He was very nice to take me in his class ME 211 to catch up. There was one time, one of the hard drive broke without a clear reason (I have the habit to back up all my data into several hard drives, but some experimental data in the drive I did not back up). I was so depressed. IT told me that it could cost a lot and Prof. Thouless said ‘I will take care of it and do not let this influence you’. I always want to say that a good advisor is someone teaches you how to run research but also tells you how to be a good person. I think he is that kind of advisor. I can not thank more for Professor Barber’s ‘knock door’ policy. I was very shy for the first year and was afraid of asking questions. He encouraged me that if I have some problems or questions that I cannot solve, I should talk to him even though it is not the scheduled meeting time. You cannot imagine how I appreciate that. It makes everything easier. He shared a lot of stories based on



his experience, which inspired me to be a better and also more confident researcher. I can not appreciate more for Professor Lu's help on detail instructions about the motors, Arduino and strain gauge. You really can not imagine that full professor will go to our lab and work with you to solve the specific problems. I also want to appreciate the opportunities that professor Lu provided to help group members and students from other universities, other group members to run some experiments, which make me to know lots of interesting research and meet lots of good friends. I want to thank my committee members Professor Liang Qi, Professor Greg Hulbert for your support, guidance and discussions in UM. I also want to thank Dr. Richard Hamm, Dr. Isele Olaf, Dr. Don Kearney, Dr. Han Xu. I am so fortunate to be funded by P&G and to be part of this collaborative and innovative team. I also want to thank my advisor when I am doing summer intern in P&G, Dr. Peter Koenig and Dr. Andrei Bureiko, who teach me a lot how to give a presentation, how to conduct a experiments in R&D and how to purchase the equipment in the company. All the skills are so useful and I can not appreciate more.

I want to appreciate Dr. Yi-Li Wu, who taught me more than two years English, culture, life, and more one-on-one. She is an excellent teacher and researcher. She also has the passion to make the people around her to work hard and work smart. She is one of my friends that no words can express my gratitude.

I also want to thank all my dearest colleagues: Hai Wang, Zhupan Hu, Fanbo Meng, Guangyu Liu, Zhouzhou Zhao, Isha Gupta, Bin Wu, Jiangyu Zhang, Kisik Hong, James Gorman, Marie Rice, Callan Luetkemeyer, Jon Estrada, Will LePage, who gave me a lot of good ideas, help and fun in the office. I also want to thank my friends Ruiming, Mingfei, Yan, Patrick, Judy, Qianying, Tianjiao, Jipu, Xin, Yuguo. Thank you for all of your support and encouragement.

Last but not least, I want to thank my parents. You are the best parents who do not care how high I fly but how hard it can be. You are the smartest parents who do not care how smart I am but how I can understand the world, science, economy, politics. You are the coolest parents who do not care what the tradition is but what is the right way to advance the society and make people, friends and family happy. I love you.

## TABLE OF CONTENTS

DEDICATION . . . . .	ii
ACKNOWLEDGEMENTS . . . . .	iii
LIST OF FIGURES . . . . .	viii
ABSTRACT . . . . .	xiii
CHAPTER	
<b>I. Introduction . . . . .</b>	<b>1</b>
1.1 Overview . . . . .	1
1.2 Research advances in abrasion mechanism of fabrics . . . . .	3
1.3 Research advances in objective evaluation of fabric damage . . . . .	5
1.3.1 Binary by pixel-based brightness . . . . .	6
1.3.2 Fast Fourier transform techniques . . . . .	6
1.3.3 Wavelet analysis techniques . . . . .	7
1.4 Research advances in fiber modeling . . . . .	8
1.4.1 Geometric model: Serret-Frenet frame . . . . .	8
1.4.2 Mathematical and physical model: Kirchhoff Theory . . . . .	8
1.4.3 Finite element method and finite difference method . . . . .	10
1.4.4 Rayleigh-Ritz method . . . . .	10
1.4.5 Previous study about the evolution of fiber shape . . . . .	11
1.5 Structure of dissertation . . . . .	12
<b>II. <i>In-situ</i> Observations of Abrasion Mechanisms of Nonwoven Fabric . . . . .</b>	<b>15</b>
2.1 Introduction . . . . .	15
2.2 Experimental methods . . . . .	17
2.2.1 Set-up 1 for large magnification . . . . .	17
2.2.2 Fabric samples . . . . .	20
2.2.3 Choice of abradant . . . . .	21
2.3 Results and discussion . . . . .	22
2.3.1 <i>In-situ</i> observation of the abrasion process . . . . .	22
2.3.2 Morphology of fuzziness . . . . .	23
2.3.3 Pill precursors . . . . .	25
2.3.4 Pill morphology and correlation with precursors . . . . .	27
2.3.5 Effect of bonding temperature . . . . .	30
2.3.6 Effect of fiber diameter . . . . .	32
2.4 Conclusions . . . . .	33

<b>III. Use of Wavelet Analysis for an Objective Evaluation of the Formation of Pills in Nonwoven Fabrics</b> . . . . .	34
3.1 Introduction . . . . .	34
3.2 Reconstruction of pill information . . . . .	38
3.3 Experimental methods . . . . .	44
3.4 Results . . . . .	46
3.5 Discussion . . . . .	49
3.6 Conclusion . . . . .	53
<b>IV. Generation of Perversions in Fibers with Intrinsic Curvature</b> . . . . .	55
4.1 Introduction . . . . .	55
4.2 Mathematical model . . . . .	57
4.2.1 Dimensionless formulation . . . . .	59
4.3 Uniform helix solution . . . . .	60
4.4 Shape of the perversion . . . . .	63
4.4.1 Rayleigh-Ritz approximation to the shape . . . . .	68
4.4.2 Energetic considerations . . . . .	72
4.5 Persistence of perversions . . . . .	75
4.6 Conclusions . . . . .	82
<b>V. Fabric Design Based on Finite Element Method</b> . . . . .	84
5.1 Introduction . . . . .	84
5.2 Conditional random walk to generate fibers . . . . .	84
5.3 Algorithm of generating bonding site . . . . .	86
5.4 The average material properties of fabric . . . . .	88
5.4.1 Different material properties for fiber and bonding site . . . . .	89
5.4.2 Different material properties between individual fibers . . . . .	90
5.4.3 Abrasion models considering different abrasants . . . . .	91
5.5 Quantification method for degree of fuzziness and degree of damage . . . . .	93
5.5.1 Degree of fuzziness . . . . .	93
5.5.2 Degree of damage . . . . .	94
5.6 Design of simulations . . . . .	95
5.7 Conclusion . . . . .	96
<b>VI. Conclusion and Preliminary Results for Future Work</b> . . . . .	97
6.1 Conclusion . . . . .	97
6.2 Limitation . . . . .	99
6.3 Future work . . . . .	100
6.4 Fiber-level model for intrinsic twist . . . . .	101
6.4.1 Dynamic or static Kirchhoff equation . . . . .	101
6.4.2 Newton's equation . . . . .	103
6.4.3 Moment equation . . . . .	104
6.4.4 Energy method . . . . .	108
<b>BIBLIOGRAPHY</b> . . . . .	110

## LIST OF FIGURES

### Figure

2.1	A schematic illustration of the system used to study the mechanism of pill formation <i>in-situ</i> during abrasion. The bottom camera records the morphology of the fabric when the abradant moves. . . . .	18
2.2	Loading devices for <i>In-situ</i> set-up (SU1) for larger magnification with sample size of $20 \times 20 \text{ mm}^2$ . . . . .	19
2.3	A schematic illustration of the system used to study the mechanism of pill formation <i>in-situ</i> during abrasion. Camera from top and side records the morphology of the fabric from different angles. . . . .	20
2.4	Optical image of fabric bonded (A) at 135 °C and (B) at 153 °C, before abrasion. Corresponding SEM images are shown in (C) and (D) respectively, and suggest less complete fusing of the fibers at the lower bonding temperature. . . . .	21
2.5	Qualitative results showed that pills are formed more readily when the abradant is fibrous, presumably because of the possibility of entanglement between the fibers of the fabric. . . . .	22
2.6	Top view (A-1, B-1, C-1) and side view (A-2, B-2, C-2) of the fabric bonded at 135 °C, after 10, 20 and 30 minutes of abrasion respectively with a soft toothbrush. . . . .	23
2.7	Forms of fabric damage associated with fuzziness: Type 1: Fiber fracture between bond sites; Type 2: fiber fracture at a bond site; Type 3: Pull-out of a locally unbonded fiber; Type 4: Detachment of an unbroken fiber from one or more bond sites. The cartoon insets give a clearer picture of these mechanisms. . . . .	24
2.8	Higher magnification optical image of fuzziness. The blue arrows (i) identify damaged regions on fibers pulled out from bond sites [Type 4] and the red arrow (ii) indicates an unbonded and unbroken fiber [Type 3]. . . . .	25
2.9	Types of precursor morphology. . . . .	26
2.10	Types of precursor morphology. . . . .	27
2.11	Morphology of ball pills [A,B] and long pills [C,D]. . . . .	28
2.12	Silicone rubber abradant [A] and resulting entanglements [B]. . . . .	29

2.13	[A] Long pills form initially along the machine direction, indicated by the dashed line, but after continued sliding [B], they become approximately perpendicular to the sliding direction, indicated by the arrow. . . . .	30
2.14	Force-extension curves and representative images for peel tests on fabrics bonded at 135 °C (A) and 153 °C (B). . . . .	31
2.15	Precursor and pill formation for larger diameter fibers. . . . .	32
3.1	Illustration of the difference between a two-dimensional, discrete-Fourier-transform and a two-dimensional, discrete-wavelet transform based on a sinusoid with a small perturbation. The limitation for two-dimensional, discrete-Fourier-transforms is that, since the signal is diluted during the transform, small perturbations or localized features may be missed. In order to capture localized data in both the frequency and spatial domains, a wavelet analysis has been introduced to analyze digital images of fabrics. . . . .	36
3.2	(A) Image of fabric before abrasion. The periodic structure that can be observed in this image results from the thermal bonding sites. (B) Image of fabric after abrasion, showing the presence of pills of few millimeters in length. It is these features that our technique focuses on, not the loss of periodicity at the smaller scale.	38
3.3	(A) Image of non-woven fabric after abrasion; (B-H) Decomposition of the original image after subtraction of the digital information at increasingly fine scales. . . . .	40
3.4	The mother wavelet used to create the images of Figure 2. . . . .	41
3.5	Relation between the size of wavelet and the size of pill. If the size of the shifted and scaled version of the wavelet matches the size of pill, the pill information will be picked up by returning a large coefficient. . . . .	42
3.6	Reconstruction of the signals corresponding to levels 5 and 6 results in the image on the right (B). This can be compared to the unfiltered image of the abraded specimen on the left (A) to show that this reconstructed image broadly captures the pills. . . . .	43
3.7	Hardware set-up for wavelet analysis. The hardware set-up was composed of an optical microscope, an LED light, a digital camera, and a computer. The magnification of the microscope and the resolution of the camera was matched by a one-time calibration process as described in Section 2. The appropriate magnification of the microscope and camera resolution was such that the region of interest can be imaged to a size of 512 by 512 pixels or larger. This required a digital camera with a resolution of 0.3 <i>M</i> pixels or higher. . . . .	45
3.8	Gray value, <i>P</i> , of a pure digital, white image, paper-based materials, and fiber-based materials. . . . .	47
3.9	The measured gray-value ratio, $\delta$ correlates well with a traditional rating method. (Independent measurements, the "traditional ratings" are courtesy of P&G.) . . . .	49
3.10	Six different mother wavelets used to study the effect of the choice of wavelet. . . . .	50

3.11	In order to further optimize the wavelet analysis for a non-woven fabric, a range of candidate wavelets were used to test the influence of different mother wavelets. The six wavelets chosen were from two wavelet families: Daubechies and Coiflets (see Figure 3.10 in the main text for the key to the shapes of the wavelets). The samples from the five groups analyzed in Figure 3.9 were used for this analysis. The error bars represent one standard deviation for the results from the different samples. The plot shows that the choice of mother wavelet has a negligible effect on the choice of wavelet. . . . .	51
3.12	Rotation of the fabric had negligible effect on the analysis method. A non-woven does not have as obvious a periodic structure as a woven fabric does. However, for the non-woven fabric in the present studies, there were several factors that could lead to anisotropy. The first was the bonding pattern, which had a hexagonal close packing form. The second was the production orientation, which was along the close packed direction of the bond sites. The third was the wear direction. Despite these effects, the difference of degree of damage before and after rotation was only around 6%. The error bars represent one standard deviation in the variation for the five different specimens analyzed from each of the sets of samples used to obtain the data of Figure 3.9. . . . .	53
4.1	(a) The shape of a fiber abraded in a central segment; (b) Enlarged perspective view of the abraded segment showing two helices separated by a perversion. . . . .	56
4.2	A fiber loaded by equal and opposite forces at its ends. We define a path coordinate $s$ and a director basis $\{\mathbf{d}_1(s), \mathbf{d}_2(s), \mathbf{d}_3(s)\}$ . We also define the end-to-end distance $h$ . 58	58
4.3	(a) Normalized curvature $\tilde{k}_1$ and twist $\tilde{k}_3$ , and (b) force $\tilde{P}$ and strain energy $\tilde{U}$ for a uniform helix as functions of end-to-end distance $h/L$ . . . . .	63
4.4	The normalized strain energy of a helix segment as a function of the end-to-end distance from finite-element calculations (points) and the analytical solution from Eqn. 4.19(line). The numerical uncertainties in this plot are smaller than the data points. . . . .	65
4.5	Two views of a typical ABAQUS output showing helical coils of opposite chirality separated by a perversion. $h/L = 0.78$ . . . . .	66
4.6	(a) Finite-element results (points) for $\tilde{k}_1$ , $\tilde{k}_2$ and $\tilde{k}_3$ in the perversion segment as functions of $\tilde{s}$ for $h/L = 0.88$ . The solid lines are obtained from McMillan and Goriely's perturbation solution for a value of $\mu = -0.19$ , corresponding to $h/L = 0.88$ . (b) The same results plotted in $\tilde{k}_3 - \tilde{k}$ space, where $\tilde{k} = \sqrt{\tilde{k}_1^2 + \tilde{k}_2^2}$ . The dashed line represents the locus of fixed points defined by the pure helix relation (4.19) <sub>2</sub> . We also present a similar comparison for $h/L = 0.95$ (corresponding to $\mu = -0.095$ ), for which the agreement with the perturbation solution is much closer. The numerical uncertainties in this plot are smaller than the data points. . . . .	67
4.7	Rayleigh-Ritz approximations with five parameters for the curvature and twist functions $\tilde{k}_1$ , $\tilde{k}_2$ and $\tilde{k}_3$ (lines) compared with finite element results (points) for (a) $h/L = 0.88$ and (b) $h/L = 0.78$ . The numerical uncertainties in these plots are smaller than the data points. . . . .	70
4.8	Comparison of the predicted fiber morphology from finite element and Rayleigh-Ritz calculations for $h/L = 0.78$ . . . . .	71

4.9	Rayleigh-Ritz solution (solid line) (a) using Eqns. 4.15, 4.16 and 4.17 with five parameters, and (b) using Eqns. 4.19, 4.20 and 4.21 with eleven parameters, compared with finite-element results (points) for $h/L = 0.32$ . The numerical uncertainties in these plots are smaller than the data points. . . . .	72
4.10	The change in normalized end-to-end distance $\Delta\tilde{h} = k_1^{(0)}\Delta h$ between a pure helix and a coil with a perversion, showing results obtained by both finite-element calculations and the Rayleigh-Ritz method. The introduction of a perversion causes shrinkage of the fiber if $h/L$ is less than about 0.5. It should also be noted that the 5-parameter Rayleigh-Ritz solution works very well for values of $h/L$ greater than about 0.7. . . . .	74
4.11	(a) The difference in strain energy between a purely helical portion of the fiber and the same length of fiber containing a single perversion. Once again, the results are well described by the 5-parameter Rayleigh-Ritz approximation of Eqns. 4.15, 4.16 and 4.17) for $0.65 < h/L < 1$ , and by the 11-parameter approximation below this range. (b) The difference in total energy between a purely helical portion of the fiber and the same length of fiber containing a single perversion. This plot is calculated using the 11-parameter Rayleigh-Ritz solution. . . . .	75
4.12	Perversions are identified by sign changes in $\tilde{k}_3(\tilde{s})$ . Those at A D and E are annihilated as $h/L$ is reduced. . . . .	77
4.13	Evolution of perversions during unloading to $h/L = 0.953$ followed by reloading to $h/L = 0.972$ . Notice that perversions D and E are not regenerated during reloading, and B moves to the left-hand end and disappears. . . . .	79
4.14	The velocity at which the ends of the fiber are relaxed influences the number of perversions that are retained at $h/L = 0.5$ . $d\tilde{h}/dt =$ (a) $3.5 \times 10^{-7}$ , (b) $9.7 \times 10^{-7}$ , (c) $9.7 \times 10^{-6}$ and (d) $2.43 \times 10^{-5}$ . Notice that (b) corresponds to the conditions under which Fig. 4.12 was obtained, and the perversions B, C and F have been retained down to $h/L = 0.5$ . . . . .	81
5.1	Random walk to generate natural fibers. . . . .	85
5.2	Conditional random walk to generate a piece of fabric. . . . .	85
5.3	The algorithm to generate the fabric. . . . .	86
5.4	Algorithm of generating bonding site . . . . .	87
5.5	Here is one example of bonding site used in the simulation before and after merge in ABAQUS. Bonding site can be easily changed based on the design. . . . .	88
5.6	Material properties of individual fiber are obtained from the test and then are added into the ABAQUS model. The material properties can also be changed based on the design. . . . .	89
5.7	Material properties of individual fiber are obtained from the test and then are added into the ABAQUS model. The material properties can also be changed based on the design. . . . .	90
5.8	Normal distribution of material properties of individual fiber. . . . .	90



5.9	The fields in ABAQUS are assigned by FORTRAN code 'VUSDFLD' so that each element can have its own material properties. The material properties can be changed based on the distribution functions. . . . .	91
5.10	Abrasion model with abradant of toothbrush. . . . .	92
5.11	Abrasion model with abradant of silicon rubber. . . . .	92
5.12	The morphology of fabric after abrasion from our simulation are similar to experimental results, where obvious fuzziness is observed on the surface of fabric. . . . .	93
5.13	Degree of fuzziness using distribution of fiber height after abrasion. . . . .	94
5.14	Degree of damage using the average damage of all elements. . . . .	95
5.15	Design of simulation and parameter optimization using abrasion model. . . . .	96
6.1	Positive $\sigma$ are found so that the helical solution is not stable. . . . .	108

## ABSTRACT

Fabric abrasion, especially pilling is a problem in textile industry. Pills on the fabric surface are the result of damage to the garment, which cause unappealing appearance. One of the requirements for the use of fabric in many applications is high abrasion resistance.

In order to study the evolution of damage process during usage, and further investigate the relation between macro and micro mechanisms of abrasion, we performed in-situ experiments on nonwoven fabric. At macroscopic scale, different morphology of fabric have been identified when fabric rubs against a non-fiber abradant as well as against a fiber abradant. At the microscopic scale, four abrasion mechanisms at the individual fiber level have been identified. In addition, the correlation between two types of pills and six types of precursors have been found.

To evaluate abrasion of nonwoven fabrics with minimal human interpretation, we apply two-dimensional, discrete-wavelet transforms to the images of nonwoven fabrics. We describe the degree of damage in terms of a gray-value ratio that is extracted from the details of the wavelet characterization, and show that this parameter correlates well with an independent qualitative assessment of the damage.

In order to propose the next-generation design of fabric with better damage resistance, a fiber-level model is established using Rayleigh-Ritz and Finite-Element method based on Kirchhoff-rod theory. We have investigated the generation and

evolution of perversions (an inversion of chirality) between helical segments of a fiber with uniform intrinsic curvature when the ends are restrained against rotation. The twist function  $k_3$  changes sign in passing through a perversion and this provides a convenient way to identify and approximate the morphology in more complex situations. The shape of an isolated perversion is well approximated by a simple Rayleigh-Ritz trial function. The lowest energy state is one in which perversions occur only when they are geometrically necessary because of the end restraint against rotation. However, the energy differential is small when the fiber is almost straight, so additional perversions may be introduced by noise in the early stages of unloading when the fiber is almost straight. If the fiber is further unloaded, perversion pairs may approach and annihilate each other, but if the perversions are too far from each other or from the fiber ends, an effective energy barrier exists so that they may persist well below the loading conditions where the energy differential is significant. A sufficiently rapid unloading resulted in a higher density of perversions being frozen into the fiber, than that obtained by slower rates of unloading, suggesting an analogy to the retention of defects in solids after thermal quenching.

## CHAPTER I

### Introduction

#### 1.1 Overview

Fabric as a human necessity has such a long history that even historians can only roughly estimate the dates of fabric as an integral part of human daily life (at least back to the late Stone Age, approximately 100,000 years ago). Methods of fabric production have continuously been developed such as knitting, braiding, weaving and non-weaving [75]. In addition, the sources of fabric have been also extended from traditional natural materials like animals, plants or minerals to petroleum-derived synthetic fibers for instance nylon, acrylic, spandex, polyester. With the burgeoning of synthetic fibers, the usage of fabrics in modern society becomes more and more extensive.

Extensive use of fabric in home supplies, hygiene, and even industry have expedited perpetual development of low-cost, environment-friendly and robotized technique in the textile industry. In the past 40 years, nonwoven has been developed in an overwhelming rate since it can be synthesized directly from raw materials in a continuous production line. This process economizes previous tedious conventional textile operations such as braiding, weaving or knitting [8, 68, 24]. The inexpensive, simplicity and high-yield advantage enable the nonwoven to compete with traditional

fabrics and occupy more market shares.

However, for either traditional knitted or woven fabrics or booming nonwoven fabrics, fabric pilling during usage or laundering is a serious fabric fault that has been recognized as a stubborn problem in many industry fields. For example, in apparel and textile, since the development of pilling on a fabric surface not only causes the abrasion or even damage of garment but also results in unshapely appearance which makes customers feel uncomfortable.

When it comes to hygiene like baby's diaper, it is severer since it is related to the baby's health. As we all know, disposable diapers provide a great convenience in the modern life. Disposable diapers are generally composed of a top sheet, absorption part and waterproof sheet. The top sheet, which is usually made of nonwoven fabrics, is critical since it is in direct contact with the baby's skin and the improper material or defects such as fuzziness and pillings on the surface of the fabrics not only pose an artistic problem but also may cause diaper dermatitis[73, 37].

However, research focusing on the abrasion property of nonwovens fabric is insufficient, and the possible mechanisms of abrasion (fuzziness and pilling) have not been fully understood. Besides, the quantification of damage still relies on the traditional methods. Moreover, the strategies of evaluating and improving abrasion resilience in nonwovens also need to be further investigated. Therefore, there are three main problems we need to solve:

- What is the abrasion mechanism of nonwoven fabric and which one is the dominant mechanism;
- How to quantify the damage of nonwoven fabric;
- How to understand more physics behind the behavior so that we can design

next-generation fabric.

## 1.2 Research advances in abrasion mechanism of fabrics

One of the main causes of fabric deterioration is fabric fuzziness or pilling which occurs during abrasion. Abrasion will eventually terminate the use of products, however, the service life or the end state of one specific fabric highly depends on people's requirements which can differ case by case. Many groups have studied the possible abrasion mechanisms of different fabrics in various applications[21, 18, 19, 2, 20].

Mechanism of wear is complicated when related to a real condition in daily life. Under fixed normal stress, the procedure of wear can be divided into three different stages: primary stage during which surfaces adapt to each other and the wear rate might vary between high and low, steady stage when the wear rate is constant and tertiary stage when the deterioration is rapid [21]. Different surface condition can result in varied wear mechanisms, for example, the abrasion mechanism of textile materials rub against soft materials may not be the same with that against hard materials.

Similarly, the abrasion mechanism of textile material rub against flat surface may be different from that rub against rough surface. According to previous studies, wear mechanisms of materials include: adhesive wear, abrasive wear, fretting wear, erosive wear and surface fatigue [12]. Among these wear types, adhesive wear, abrasive wear and surface fatigue mechanisms play important roles in the abrasion mechanism of fabrics.

Adhesive wear occurs during frictional contact and generally refers to unwanted displacement and attachment of wear debris and surface material from one surface to

another, which is caused by strong adhesive forces between atoms and accumulation of energy in the plastic zone between the asperities during relative motion [13]. The adhesive wear is harmful to the fabrics because it can lead to transfer of material which can be a part of pillings and accelerate pilling formation.

Abrasive wear occurs when a hard rough surface slides across a softer surface like fabrics [11]. ASTM International (formerly American Society for Testing and Materials) defines it as the loss of material due to hard particles or hard protuberances that are forced against and move along a solid surface [60]. There are two modes of abrasive wear, one is two-body abrasive wear and another is three-body abrasive wear. Two-body wear happens when the material is constrained and displaced by a cutting or plowing operation, while in three-body wear material, the material is free to slide or roll down a surface [26].

Fatigue wear occurs when contacts between asperities with repeated local stress during sliding or rolling and the applied load is higher than the fatigue strength of the materials. High plastic deformation causes crack initiation, crack growth, and fracture. Fatigue crack starts at the single fiber surface and spread to the subsurface regions. These cracks may connect with each other, resulting in delamination of the single fiber pieces. Previous studies found unexpected but considerable fatigue damage during fiber entanglement [20, 17]. And the presence of a certain amount of fatigue breakdown and wear off prior to pilling formation will reduce density of fuzzy fiber for potential pilling growth. In addition, the fatigue zone also acts as hinges since fatigued fibers have substantially lower bending rigidities than the intact fibers.

During usage or laundering, fabrics are subject to a variety of different forces which may result in combination of abrasion mechanism. Abrasion changes the surface property, then damages the internal structure of fabrics and eventually results in

fabric failure. Fabric failure can be caused by the gradual breakdown of the fabric geometry integrity and can also be related to the gradual deterioration of individual fibers.

From energy perspective, abrasion resistance depends more on a high energy of rupture than on a high tenacity at break [1]. Thus, to prevent abrasion damage, the material must be capable of absorbing energy and releasing that energy upon the removal of load. Energy under tension, compression, shear and bending should be of great concern for the evaluation of surface abrasion; however, these energies are unknown, and therefore understanding the evolution of energy under tension permits at least a quantitative interpretation of abrasive damage in fabrics.

### **1.3 Research advances in objective evaluation of fabric damage**

Although observation of fabric during friction test give us different damage morphology and abrasion mechanism, we still need to know the degree of damage from both scientific and industrial point of view. In the current industry, the degree of pilling based on a visual comparison of the sample with a set of standard pilling images to determine the degree of pilling on a level ranging from 1 (very severe pilling) to 5 (no pilling) [23]. Former subjective evaluation could be inconsistent and inaccurate. Since it largely depends on human's proficiency, pilling rating may vary from one person to person. Developing reliable, accurate and simple objective evaluation methods is necessary and urgent for current textile industry. Fuzziness and pillings are the main features in the damage rating procedure [15, 48, 46, 47].

For a used fabric with fuzziness and pilling, their images by digital camera or optical microscope usually include information such as illumination, fabric surface unevenness, texture and pillings. The goal of image analysis or laser scanning is to



try separating different parts of information. Objective pilling assessment methods, such as image analysis techniques [82, 84] and laser scanning [86] have been reported before. For image analysis, pilling and fuzziness can be extracted directly from the spatial domain by analyzing pixel-based brightness value. It can also be obtained in frequency domain by fast Fourier Transfer (FFT), Short-time Fourier Transfer (Gabor) and Wavelet Analysis [87, 83, 54].

### **1.3.1 Binary by pixel-based brightness**

A binary image is a digital image that has only two possible values (0 or 1) for each pixel. Typically, the pixel with value of 0 is black while the pixel with value of 1 is white. Binary images often arise in digital image processing such as segmentation, thresholding, and dithering. With the images' contrast enhanced by histogram equalization and noise reducing depended on the pattern of neighboring pixels, binary pattern can be obtained by the thresholding process . We can clearly observe the locations of warp and weft yarns and spaces between them for woven fibers [42]. It is very useful for woven fabrics, however, study related to nonwoven fabrics is sparse and may need more deep explorations.

### **1.3.2 Fast Fourier transform techniques**

The Fourier transform (FT) and the inverse transform provide an approach to allow a 2 dimensional (2D) image to be mutually converted between time domain and frequency domain. Fast Fourier Transform (FFT) algorithms significantly enhance the calculation efficiency. FT is one of useful technique for image processing such as image enhancement and measurement. Images taken during the friction test contains fuzziness, pillings, periodic structure (woven), nonperiodic information, light unevenness and noise elements. It is quite difficult to separate different components

of information in the spatial domain while in frequency domain, the information will inevitably be decomposed into different components or peaks, especially for the woven fabrics with desired periodic structure. Xu in 1997 has already demonstrated that FFT is a useful tool in identifying fabric structures [84]. However, the vital shortcoming of FFT is that the spatial information will be lost when image is transformed into the frequency domain, is applied low-frequency filter and then is reconstructed into a new image that only contains pilling information. It is also very hard to select a dynamic filter to obtain only pilling information with minimum background elements. So FFT cannot provide enough information to localize and detect pillings [23].

### 1.3.3 Wavelet analysis techniques

Image processing algorithms in previous report cannot achieve accurate pilling prediction since it cannot separate the pilling and fuzziness information from fabrics pattern information, illumination and fabric surface unevenness, especially when the fabric pattern interfere with the ambiguous fuzz or small pillings. The multi-scale transform is an effective tool to objective pilling ratings [23]. Wang and Palmer in 2004 came up with a reasonable method in which the pilling intensity can be identified by standard deviation (STD) of the detail coefficient of two-dimensional discrete wavelet transform (2DDWT). Images with more fuzziness and pillings will have a higher STD of detail coefficient[70]. However, this methods is sensitive to rotation of the image and dilation of the image under analysis [70]. Kim and Kang proposed the image reconstruction approach for fabrics with repetitive pattern based on undecimated discrete wavelet transform (UDWT). The global repetitive pattern can be attenuated and only pillings are emphasized at an appropriate decomposition level [48]. Wang further suggests a multi-scale two-dimensional dual-tree complex

wavelet transform (CWT) method to extract the pilling information and it can decompose the images into six orientations at different scales and then only the pilling information will be reconstructed. Energy analysis methods have been employed for optimal image decomposition and dynamically discriminate pilling information from the obtained original image [23]. However, most research focus on the woven fabric with periodic background.

## 1.4 Research advances in fiber modeling

### 1.4.1 Geometric model: Serret-Frenet frame

In Serret-Frenet frame, only geometric information of fiber is considered. A fixed right-handed Cartesian basis  $\{\mathbf{E}_1, \mathbf{E}_2, \mathbf{E}_3\}$  is defined in Euclidean 3D space  $\mathbb{E}^3$ . To describe a 3D curve, We further defined a position vector  $\mathbf{r} = x_1\mathbf{E}_1 + x_2\mathbf{E}_2 + x_3\mathbf{E}_3$  Frenet triad  $\{\mathbf{e}_t, \mathbf{e}_n, \mathbf{e}_b\}$  with curvature  $k$  and torsion  $\tau$ . Therefore we have:

$$(1.1) \quad \frac{\partial \mathbf{e}_t}{\partial s} = k\mathbf{e}_n \quad \frac{\partial \mathbf{e}_n}{\partial s} = -k\mathbf{e}_t + \tau\mathbf{e}_b \quad \frac{\partial \mathbf{e}_b}{\partial s} = -\tau\mathbf{e}_n$$

where  $\mathbf{e}_t = \frac{\partial \mathbf{r}}{\partial s}$ . The curvature  $k$  and torsion  $\tau$  can be calculated based on the definition.

$$(1.2) \quad k = \left\| \frac{\partial \mathbf{e}_t}{\partial s} \right\| = \left\| \frac{\partial^2 \mathbf{r}}{\partial s^2} \right\| \quad \tau = \frac{1}{k^2} \left[ \frac{\partial \mathbf{r}}{\partial s}, \frac{\partial^2 \mathbf{r}}{\partial s^2}, \frac{\partial^3 \mathbf{r}}{\partial s^3} \right]$$

For example, if the constant curvature  $k \neq 0$  and twist  $\tau = 0$ , then we have a plane curve. If both curvature  $k$  and twist  $\tau$  are constant and not equal to zero, then we obtained a circular helix.

### 1.4.2 Mathematical and physical model: Kirchhoff Theory

The string model are limited to the assumption of complete flexibility. To resist bending and torsion, we need to relate the material properties into the model. Therefore, the Kirchhoff theory and the director basis are proposed.

The Kirchhoff model provides a mathematical framework to describe the deformation of a thin fiber in bending and torsion. We assume that the fiber is inextensible, and define a path-length coordinate,  $s$ , such that the location of a point on the fiber is defined by the position vector  $\mathbf{r}(s)$ . We also define a director basis  $\{\mathbf{d}_1(s), \mathbf{d}_2(s), \mathbf{d}_3(s)\}$ , such that  $\mathbf{d}_3(s)$  is the unit vector in direction  $\mathbf{r}'(s)$ , where the prime denotes the derivative with respect to  $s$ . The unit vectors  $\mathbf{d}_1(s)$  and  $\mathbf{d}_2(s)$  are defined so as to align with the principal axes of the cross-section, for which the second moments of area are  $I_1$  and  $I_2$ , respectively. The local curvature and twist of the fiber can be combined in a vector  $\mathbf{k}(s)$ , defined such that

$$(1.3) \quad \mathbf{d}'_i = \mathbf{k} \times \mathbf{d}_i; \quad i = 1, 2, 3.$$

In the unloaded state, the shape of the fiber is defined by an intrinsic curvature vector  $\mathbf{k}^{(0)}(s) = \{k_1^{(0)}, k_2^{(0)}, k_3^{(0)}\}$ .

The conservative of linear and angular momentum leads to the Kirchhoff equations

$$(1.4) \quad \mathbf{F}' = \int \int_{S(s)} \rho \ddot{\mathbf{X}} dS$$

$$(1.5) \quad \mathbf{M}' + \mathbf{x}' \times \mathbf{F} = \int \int_{S(s)} \rho \mathbf{r} \times \ddot{\mathbf{X}} dS$$

where  $S(s)$  is the cross-section,  $\rho$  is the mass density per unit area,  $\mathbf{r}$  is the position vector,  $\mathbf{F}$  is the force,  $\mathbf{M}$  is the moment and  $\mathbf{X}(s, x_1, x_2, t) \equiv \mathbf{x}(s, t) + \mathbf{r}(s, t)$ . Assume that the rod has a uniform circular cross-section and hence the two principle moment of inertia  $I_1$  and  $I_2$  are equal to each other, therefore,

$$(1.6) \quad \mathbf{F}'' = \rho A \ddot{\mathbf{d}}_3$$

$$(1.7) \quad \mathbf{M}' + \mathbf{d}_3 \times \mathbf{F} = \rho I (\mathbf{d}_1 \times \ddot{\mathbf{d}}_1 + \mathbf{d}_2 \times \ddot{\mathbf{d}}_2)$$

where  $I = I_1 = I_2$  is the moment of inertia and  $A$  is the area of cross-section.

### 1.4.3 Finite element method and finite difference method

Finite element method (FEM) is the most widely used method for solving engineering or mathematical problems [88]. The FEM is a numerical method for solving partial differential equations (PDEs). The FEM divides the whole system into smaller parts (Finite elements) and generates a system of simple algebraic equations.

Finite difference method (FDM) are also used for solving ordinary differential equations (ODE) or non-linear partial differential equations (PDE) [58]. It approximate the differential equations with difference equations that finite differences approximate the derivatives and generates a system of equations that can be solved by matrix algebra techniques.

In this thesis, we use the commercial software ‘ABAQUS’ to run the simulations. This software covers stress/strain or force/displacement simulations, concentrating on both linear and nonlinear static analyses as well as dynamic analyses.

This software has different modules for different functions, such as part, property, section, profile, assembly and step.

### 1.4.4 Rayleigh-Ritz method

Ritz methods are a class of methods for converting a continuous operator problem to a discrete problem. In principle, it is the equivalent of applying the method of variation of parameters to a function space, by converting the equation to a weak formulation. Typically one then applies some constraints on the function space to characterize the space with a finite set of basis functions.

For Rayleigh-Ritz method, we can use the principle of stationary potential energy to develop an approximate solution to the problem. We first assume some approximate

form for the solution, containing a number of arbitrary constants, which constitute the degrees of freedom in the solution. We then use the stationary potential energy theorem to determine ‘optimal’ values for these constants. This is known as the Rayleigh-Ritz method. It is similar to the process of fitting the best curve to a set of data points, where ‘best’ is here interpreted in the sense of minimizing some measure of error [9].

In this thesis, we use MATLAB to develop the Rayleigh-Ritz code.

#### 1.4.5 Previous study about the evolution of fiber shape

Understanding the morphology and mechanics of long thin fiber structure undergoing large spatial deformation has been a central goal in the study of filaments in nature and technology. This ranges from micro-structure like supramolecular helices [85], nanobelts [25], DNA [62], polymer chain [81] to macro-structure: organs [5, 77], for example, guts [74], flagella [29], plant tendrils [34, 27, 79], cables [35]. They can generate similar shapes due to the twist and bend of the fibers.

The non-linear nature of Kirchoff equations can describe the behavior of fiber within the framework of thin elastic one dimensional structure [32, 66, 14]. A variety of solutions exist considering an infinitely long fiber, with different initial condition or boundary conditions:

The first case is intrinsically straight fiber under tension or compression without or with twist [76, 64]. Due to the growing interest about DNA, lots of research try to understand the evolution of DNA structure and how that could related to functionality of DNA. With similar boundary condition and also mechanical behaviors, marine pipe and cables are also wildly studied.

Despite the significant difference in length scale and applications, some fundamental similarities exist. The early studies focus on the static mechanics using Euler-

Bernoulli beam theory (ref). For example, Gere and Timoshenko described the linear buckling analyses of rod under prescribed tension/compression and torsion. 'Elastica' model are also explored to describe the large rotation of the rod cross-section using linear elastic constitutive law for both bending and torsion (Antman 29 Love 30). 'Loop' and 'pop-out' stability analysis are conducted using equilibrium rod theory(P29). Further a bifurcation theory are used to interpret the stability of rod with twist and tension. Later, Professor Perkins and lots of group further study the evolution of fiber based on the Kirchhoff theory using numerical approach().

The second case is intrinsically curved fiber under tension [34, 59]. Goriely et.al. considered a stationary solution within the frame of the Kirchoff equations and studied the linear stability of the fiber, and they applied this method to address the problems for both intrinsically straight fiber and curved fiber with constant intrinsic curvature [34, 31]. Once the tendril attached to a support, the net twist has to be zero based on the topological term that Darwin proposed [59]. Two helices with opposite handedness formed and are connected by an inversion. Later, Liu et.al. further used finite element method to perform the post-buckling analysis and concluded that the geometry ratio between height and width is one of the key factors that influence the final shape of rubber stripes [39, 55].

However, no mathematical or physical model is established for the application of abrasion.

## 1.5 Structure of dissertation

The main part of this dissertation (Chapters 2-4) is composed of three separate investigations as we mentioned above. They have been published or submitted to peer-reviewed journals. As such, there might be some redundant information in these

chapters. However, as a dissertation, I would like to put more details and thinking in each chapters and hope it can help people who are interested.

In Chapter 2, I will first briefly talk about the research gap exists in non-woven fabric. To fill the gap, we established an *in-situ* set-up to study the abrasion mechanism. Based on the set-up, we summarized a systematic abrasion mechanism for fabric rub against different abrasants. and then we discovered the both micro-level and macro-level abrasion mechanism of pilling formation. We further correlate the microscopic abrasion mechanism with the macroscopic abrasion mechanism.

Chapter 3 explores quantification method for nonwoven fabric. We talked about how we choose the image processing technique. And how we successfully use the wavelet transform to obtain the damage level of nonwoven fabric. We further discussed how different parameters might influence the results. And lastly I also talked about how we developed both hardware and software for the potential application in the industry.

In Chapter 4, a mathematical framework is presented and applied to the fiber under abrasion. Both finite-element method and Rayleigh-Ritz method are used to describe the shape of perversion due to the intrinsic curvature generated during the abrasion. Further energy calculation shows that the geometrically-necessary perversion is not energetically favorable in comparison with geometrically-necessary dislocation. Multiple perversions can be generated due to random noise or perturbation. The properties of perversion are discussed. Perversions can annihilate each other but can also be persistent. And the evolution of perversions is also history-dependent.

Chapter 5 discuss the fabric design based on finite element method. And chapter 6 summarizes the major conclusion presented in Chapters 2-4, and I will also provides possible directions that I am currently interested. Some of the work I already have



some preliminary results for future study in the field.

## CHAPTER II

### *In-situ* Observations of Abrasion Mechanisms of Nonwoven Fabric

#### 2.1 Introduction

Fabric abrasion, and the resultant pilling, is a significant problem in the textile industry [37, 10, 53]. Pills are balls of tangled fibers, often connected to the surface of a fabric by anchoring fibers, and resulting from damage to the garment [40].

They degrade the appearance of the fabric and, in some applications, can cause health concerns [7]. The formation of pills in knitted and woven fabrics has been studied, and categorized into four stages. First, the free ends of fibers are pulled out of the yarn to create areas of ‘fuzz’ [28]. Second, these free fibers form permanent entanglements as a result of back-and-forth motion, and then tighten into balls [20]. Third, the fibers that anchor these balls to the structure of the yarn are pulled out to form discrete pills [20]. Fourth, these pills can fall off the fabric if the anchoring fibers fail.

The last three stages of pill formation may be similar for woven, knitted or non-woven fabrics, once there are enough long, fuzzy fibers on the surface of the fabric [17, 18, 19, 75]. However, the mechanisms by which the fibers form the initial fuzz are expected to be different between woven and non-woven fabrics. In a woven or knitted fabric made from a yarn, the fuzz can be formed if the free ends of the fibers

are brushed out of the yarn, or if fiber loops pulled out of the yarn are broken [20]. Once a fiber is broken, it can be pulled out of the yarn if the frictional force between the fibers is overcome.

In a thermo-bonded non-woven fabric, the individual fibers are not formed into a yarn, but are joined together at discrete bonding sites. Therefore, the length of a free fiber that might be formed when a fiber breaks is determined by the distance to the nearest bond site to which it is attached, which can be longer than the distance between neighboring bonds, particularly if the bond sites themselves can be broken. This fundamental difference in the basic structure of the two classes of fabric motivated the present study to investigate the formation of fuzziness and pills in non-woven fabrics.

Many studies of the abrasion of non-woven fabrics focus on parameter optimization using the Martindale test [41]. Samples are evaluated by comparing images [10, 52, 44] or by measuring weight loss [37, 44], but these results provide no insight into the mechanism of damage. Wang *et al.* [80] made SEM observations of a bi-component fabric after abrasion and identified two damage mechanisms. The polypropylene (PP) sheath of a bi-component fiber can peel and wear away owing to thermal-induced shrinkage and thermal oxidative degradation of the PP. Also, as with woven fabrics, fibers can be pulled out and rolled up during abrasion. However, the mechanism of fuzziness formation at the initial stage of abrasion for non-woven fabrics is still poorly understood.

In the present paper, we explore this question using experiments in which early stages of the abrasion process can be observed *in-situ*.

## 2.2 Experimental methods

To observe the abrasion process through the microscope when it happens, an *in-situ* set-up (SU1) with larger magnification for samples of  $20 \times 20 \text{ mm}^2$  (Figure 2.1) and another *in-situ* set-up (SU2) for test of larger fabric specimen with size of  $200 \times 200 \text{ mm}^2$  (Figure 2.3) was designed.

### 2.2.1 Set-up 1 for large magnification

The ‘SU1’ is designed based on an optical microscope with 40X-1500X phase contrast inverted microscope. The ‘SU1’ focuses on small samples with size of  $20 \times 20 \text{ mm}^2$  in rotation mode to observe the surface change of individual fibers during the formation of pills.

The SU1 for abrasion experiments of one-direction and back-and-forth was established. A transparent stationary frame was designed by software Solidworks and manufactured by laser cutting machine to support the motor, loading devices and transparent bulk to attach fabrics. A transparent glass disk with a diameter of  $120 \text{ mm}$  was connected to the motor to provide the rotational movement. It allows us to run the abrasion experiments by one-direction and also back-and-forth rotation with the speed in the range of 0 cycles/min to 60 cycles/min.

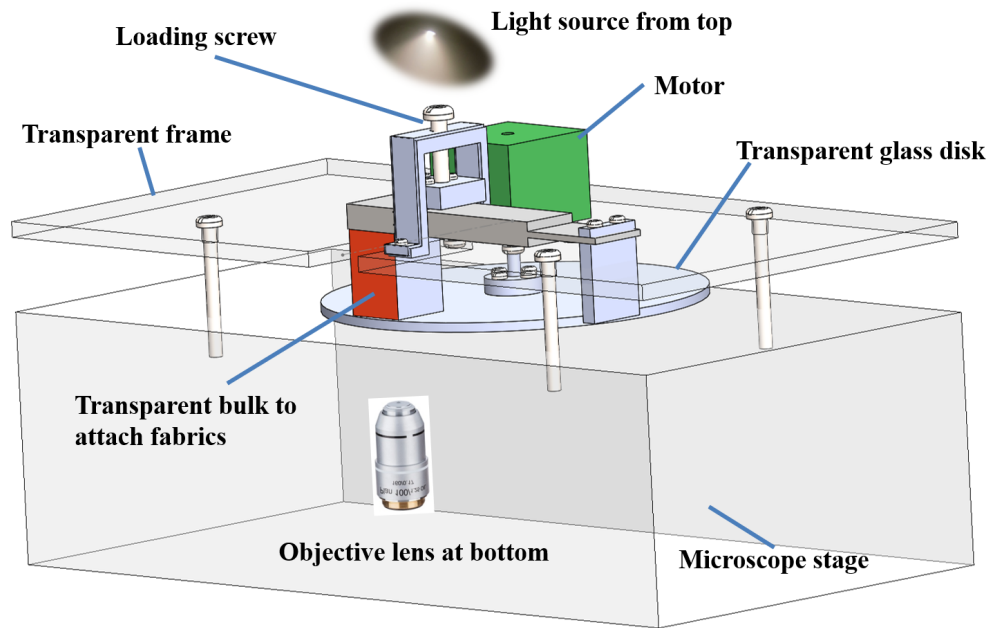


Figure 2.1: A schematic illustration of the system used to study the mechanism of pill formation *in-situ* during abrasion. The bottom camera records the morphology of the fabric when the abradant moves.

The load is applied on the top of the transparent bulk (fabric was attached on the bottom) by adjusting force of springs (Figure 2.2). The fabric was pressed down against varied abrasive substances and cameras were set from the bottom to record the abrasion process as shown in Figure 1. For this set-up, we can easily observe the movements of several fibers or individual fiber. And it also allows us to observe the surface change of individual fiber during the abrasion process. During the formation of pills, we found the surface of fibers did not change significantly, therefore, it is not one of the main factors that leads to the fuzziness and pills.

The experimental system used for *in-situ* abrasion observations (SU2) is shown in Figure 2.3. A fabric sample of dimensions 200 mm  $\times$  200 mm was attached to the top surface of a stationary frame and an abradant was moved over the fabric using

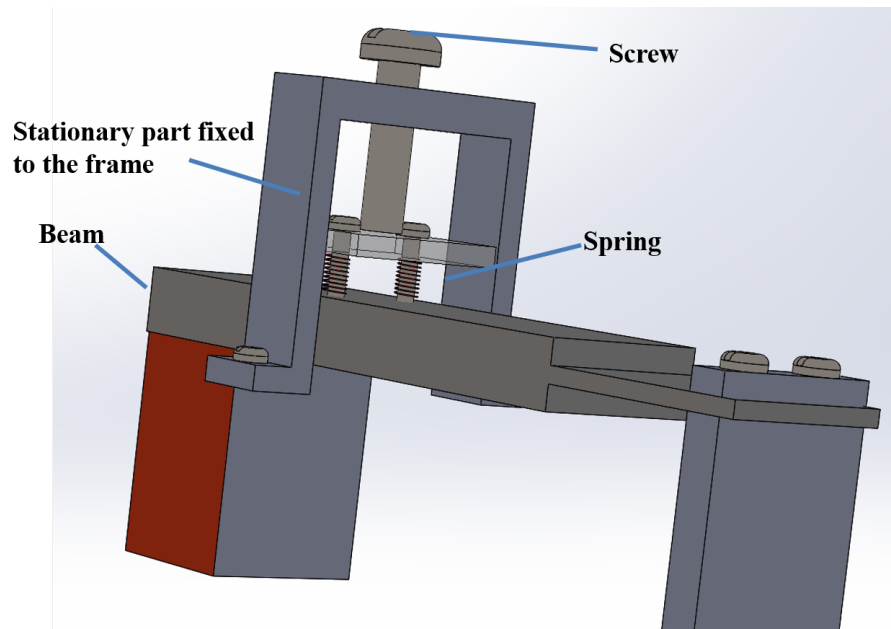


Figure 2.2: Loading devices for *In-situ* set-up (SU1) for larger magnification with sample size of  $20 \times 20 \text{ mm}^2$ .

a computer-numerical-control [CNC] machine with a changeable head. This system is capable of executing any abrasion pattern within the fabric sample, including the lissajous figures used in the Martindale test, but here we chose a simple 120 mm back and forth pattern in the  $x$ -direction, as shown in Figure 2.3. During abrasion, the surface of the fabric can be viewed from above, through an optical microscope, and also from the side, using a digital camera. A nominal contact pressure of 690 Pa was used, which is consistent with that used in the Matindale test (0.1 psi). To assess the variability of the observed phenomena, six experiments were conducted for each test condition.

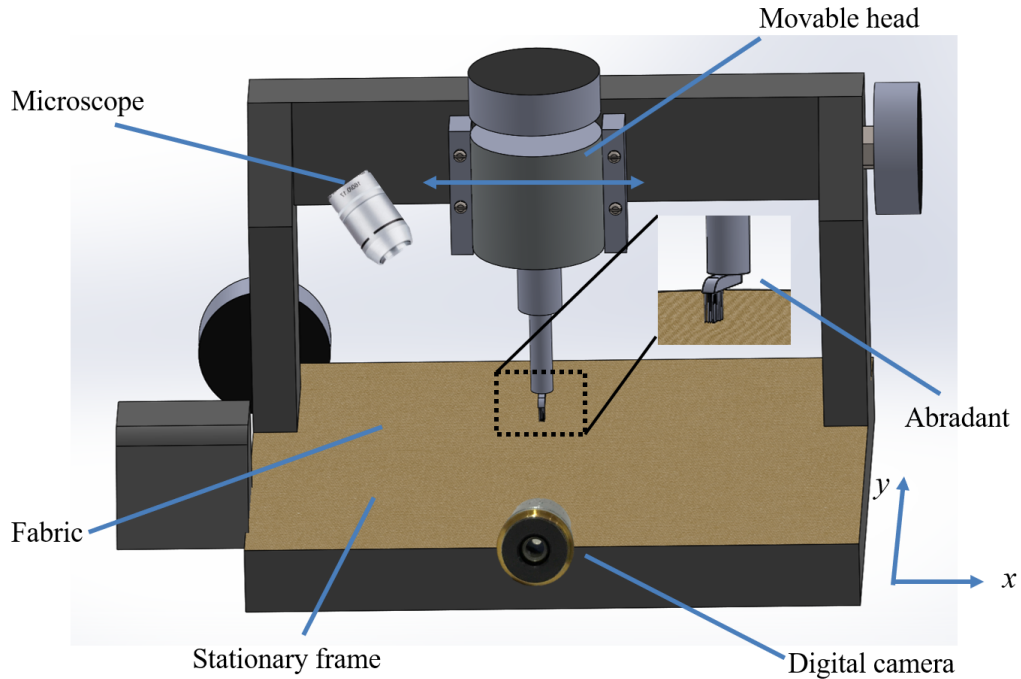


Figure 2.3: A schematic illustration of the system used to study the mechanism of pill formation *in-situ* during abrasion. Camera from top and side records the morphology of the fabric from different angles.

### 2.2.2 Fabric samples

The fabric samples that were tested were manufactured from single-component polypropylene fibers of  $20 \pm 2 \mu\text{m}$  diameter, bonded by a calender heat press. The density of the samples was  $15 \pm 0.5 \text{ g/m}^2$ , and the thickness of the fabrics was  $0.10 \pm 0.03 \text{ mm}$ . The tests were conducted at  $23 \text{ }^\circ\text{C} \pm 1 \text{ }^\circ\text{C}$  and relative humidity of  $45\% \pm 5\%$ . Figure 2.4 shows representative optical and scanning-electron-microscope [SEM] images of fabrics bonded at  $135 \text{ }^\circ\text{C}$  and  $153 \text{ }^\circ\text{C}$ , respectively. The SEM images were obtained using an FEI Helios 650 Nanolab SEM/FIB. The bonding sites can be clearly seen in the images, with a center-to-center distance of about 1.5 mm. While the morphology of these two samples appear to be similar in the optical images, the SEM suggests less complete fusing in the fabric that was bonded at the lower

temperature.

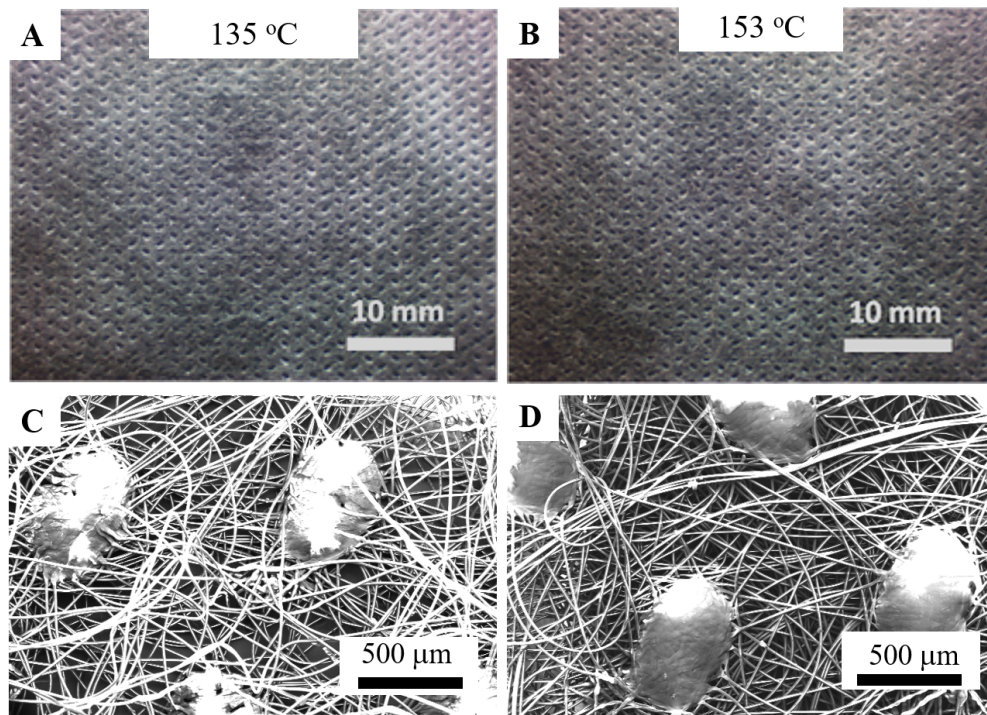


Figure 2.4: Optical image of fabric bonded (A) at 135 °C and (B) at 153 °C, before abrasion. Corresponding SEM images are shown in (C) and (D) respectively, and suggest less complete fusing of the fibers at the lower bonding temperature.

### 2.2.3 Choice of abrasant

In preliminary experiments, we used a wide range of abrasants, including both fibrous materials [non-woven fabric, knitted fabric and toothbrush] and non-fibrous [silicon carbide, glass]. Qualitative results showed that pills are formed more readily when the abrasant is fibrous, presumably because of the possibility of entanglement between the fibers of the fabric and those of the abrasant shown in Figure 2.5. It is advantageous to use an abrasant with a relatively small nominal contact area, since the abraded surface can only be imaged after the abrasant has passed. We therefore used a ‘soft’ toothbrush with a nominal contact area of length 26 mm in the sliding direction and 11 mm perpendicular to the sliding direction. There were  $6.5 \pm 0.3$



bristles/mm<sup>2</sup>, each of length 9.5 mm and diameter  $0.13 \pm 0.02$  mm.

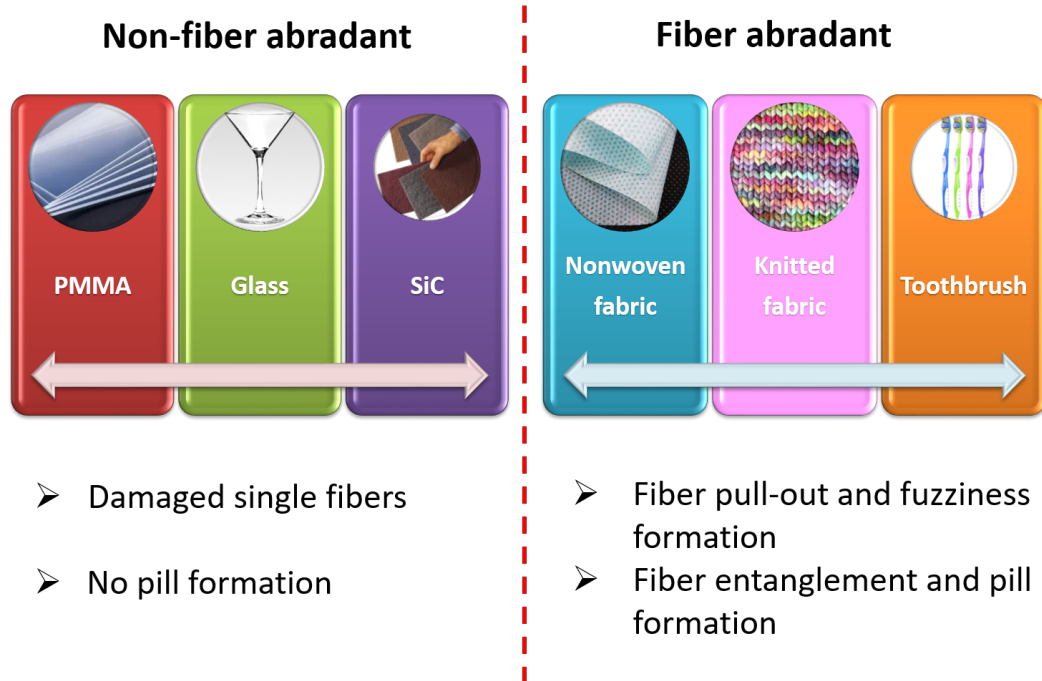


Figure 2.5: Qualitative results showed that pills are formed more readily when the abrasant is fibrous, presumably because of the possibility of entanglement between the fibers of the fabric.

## 2.3 Results and discussion

### 2.3.1 *In-situ* observation of the abrasion process

Abrasion experiments were performed on the fabric bonded at 135 °C, and the top and side views were recorded on video. A nominal contact pressure of 690 Pa was used, which is consistent with that used in the Martindale test (0.1 psi). Back-and-forth motion was imposed over a range of 120 mm at 5 cycles per minute, with a uniform nominal speed of 20 mm/s.

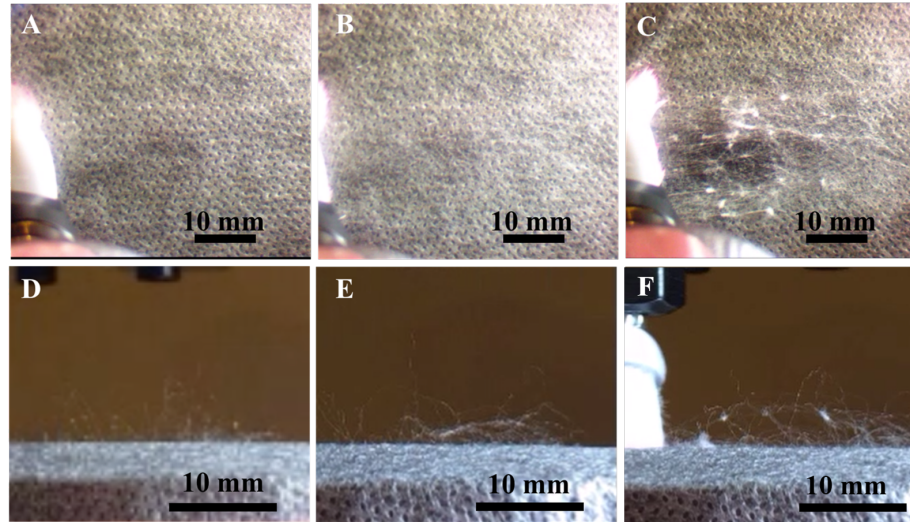


Figure 2.6: Top view (A-1, B-1, C-1) and side view (A-2, B-2, C-2) of the fabric bonded at 135 °C, after 10, 20 and 30 minutes of abrasion respectively with a soft toothbrush.

Figure 2.6 (A,B,C) shows selected frames from the *in-situ* video after 10, 20 and 30 minutes of abrasion respectively, representing three stages in the pill formation process. Figure 2.6A [10 minutes, 50 cycles] shows the development of ‘fuzziness’ consisting of fibers pulled out from the fabric. In Figure 2.6B [20 minutes, 100 cycles], entanglement and twisting of these pulled-out fibers can be observed. This is regarded as a precursor to pill formation. Finally, in Figure 2.6C [30 minutes, 150 cycles], we see the development of pills attached to the fabric by a few fibers. With continued abrasion beyond 150 cycles, some of the pills become detached, but also new pills form.

### 2.3.2 Morphology of fuzziness

Fuzziness can result from fiber fracture, or from fibers being pulled out of the fabric without fracture. Fabric specimens abraded to the initial stage of fuzziness [Figure 2.6A] were examined under the SEM to determine which mechanism is the most prevalent. Four distinct mechanisms were identified. These are characterized

by the inset cartoons in Figure 2.7, and exemplified by representative SEM images.

Type 1 and 2 involve fiber fracture, between bond sites [Type 1] or adjacent to a bond site [Type 2]. In both cases, the fracture is identified by a circle in Figure 2.7. Notice that for Type 2, the fracture exhibits a locally damaged or fused region, whereas for Type 1, the fracture is clean.

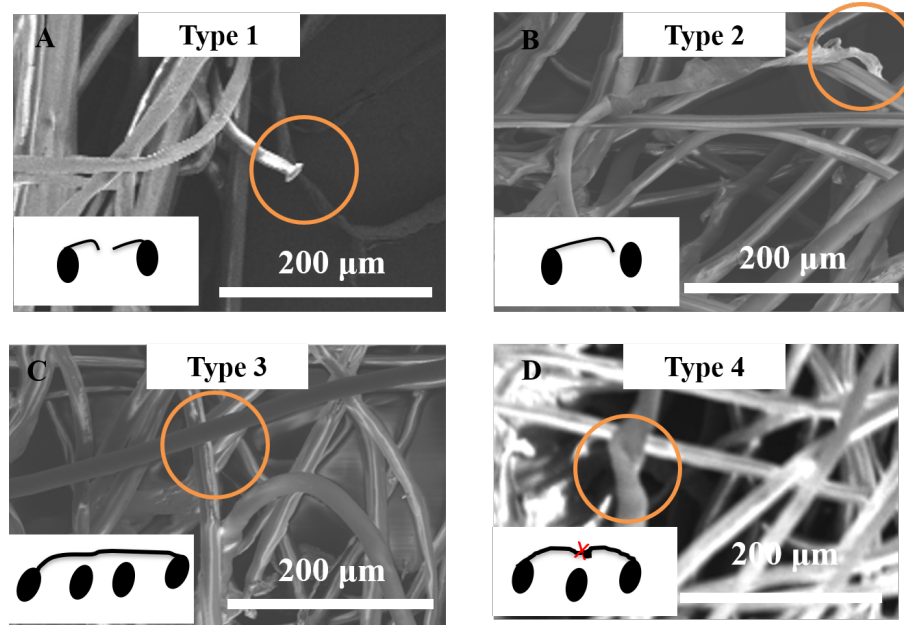


Figure 2.7: Forms of fabric damage associated with fuzziness: Type 1: Fiber fracture between bond sites; Type 2: fiber fracture at a bond site; Type 3: Pull-out of a locally unbonded fiber; Type 4: Detachment of an unbroken fiber from one or more bond sites. The cartoon insets give a clearer picture of these mechanisms.

Types 3 and 4 describe situations where a fiber is pulled from the fabric without fracture. In Type 4 the fiber is separated from one or more bond sites as shown by the existence of locally damaged regions. By contrast, Type 3 describes fibers that exhibit no such regions, indicating that they probably ‘by-passed’ several potential bond sites in the original fabric manufacturing process. The fiber direction is somewhat influenced by the manufacturing direction, but the fiber length between bond sites has a broad distribution and indeed fibers passing between bond sites without attachment are clearly visible in the SEM images of Figure 2.7 [C and D].

This distinction is seen more clearly in higher magnification optical images such as Figure 2.8, which is a top view of fibers pulled out to a location above the main body of the fabric. The blue arrows (i) in this figure indicate regions where an unbroken fiber has been detached from a bond site, whereas the red arrow (ii) indicates a fiber which is longer than the bond spacing [1.5 mm], but which shows no sign of bond site detachment. Examination of a large number of images of this kind show that Types 3 and 4 occur more frequently than Types 1 and 2. In other words, the fuzziness generated consists primarily of pulled out unbroken fibers at this stage.

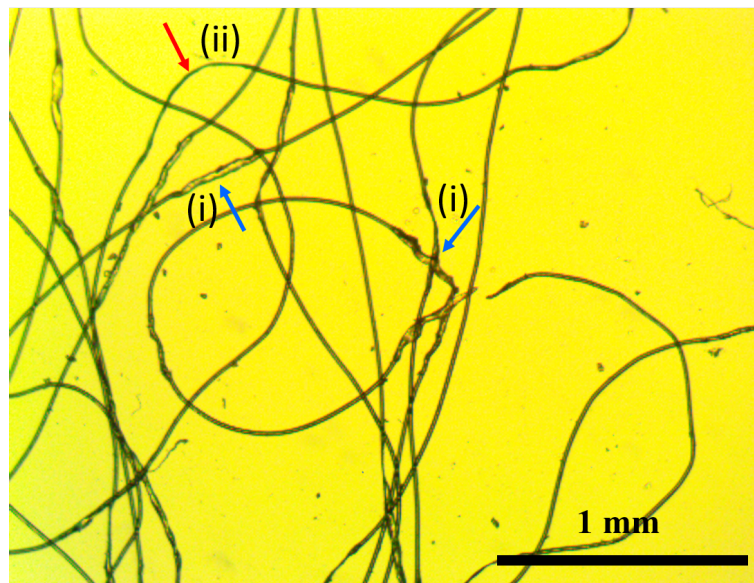


Figure 2.8: Higher magnification optical image of fuzziness. The blue arrows (i) identify damaged regions on fibers pulled out from bond sites [Type 4] and the red arrow (ii) indicates an unbonded and unbroken fiber [Type 3].

### 2.3.3 Pill precursors

We recall from Section 2.3.1 and image C of Figure 2.6 that pill formation is generally preceded by fiber entanglement and other morphological features that may be regarded as pill precursors. Some typical forms are shown in Figure 2.9. Here we tend to classify the precursors based on the intrinsic curvature and twist related to

our simulation work in Chapter 4.

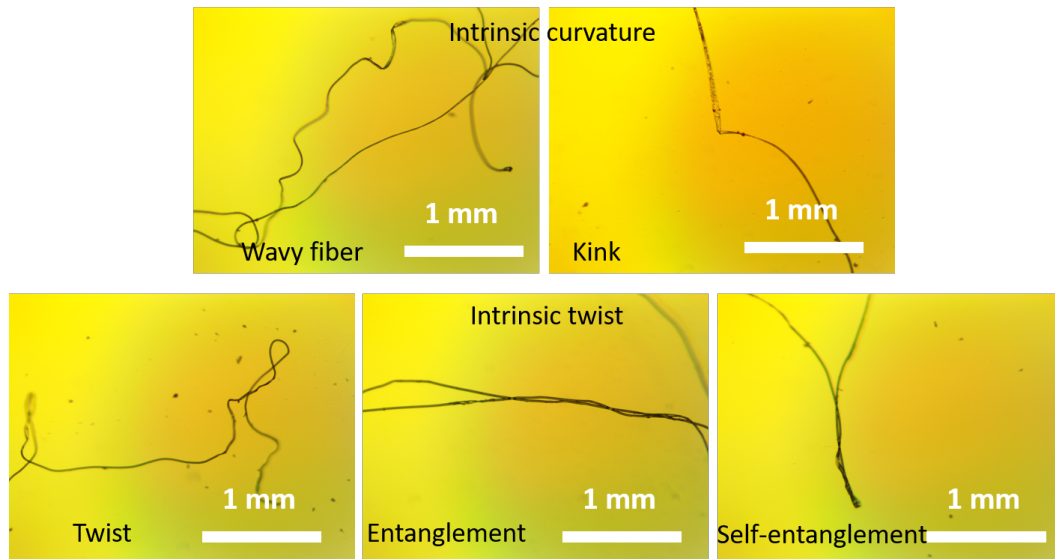


Figure 2.9: Types of precursor morphology.

We further summarized the probability of each precursor generated during the abrasion experiment in Figure 2.10. We found that wavy fibers account for about half of observed precursors, and twisted fibers for about 25%. We can see that the wavy fiber, helical fiber and kink with free end could be related to the intrinsic curvature, and twist, entanglement and self-entanglement is related to the intrinsic twist. The definition of precursor here is purely based on our observation, it will be given a more rigorous definition when it comes to simulation part.



Figure 2.10: Types of precursor morphology.

#### 2.3.4 Pill morphology and correlation with precursors

Figure 2.11 shows typical pills formed in the abrasion process. These can be characterized as *ball pills* [Figure 2.11A], which are approximately equi-axed, or *long pills* [Figure 2.11C], in which one dimension is significantly larger than the other two.

Ball pills are typically anchored to the fabric by only a few fibers, as shown in Figure 2.11B. By contrast, long pills are anchored at both ends, as shown in Figure 2.11D, and most of the fibers in the pill are approximately aligned with the long dimension.

In the experiments described in Section 2.3.1, most of the pills formed are ball pills, and we recall that wavy fibers are the most common precursors observed. In



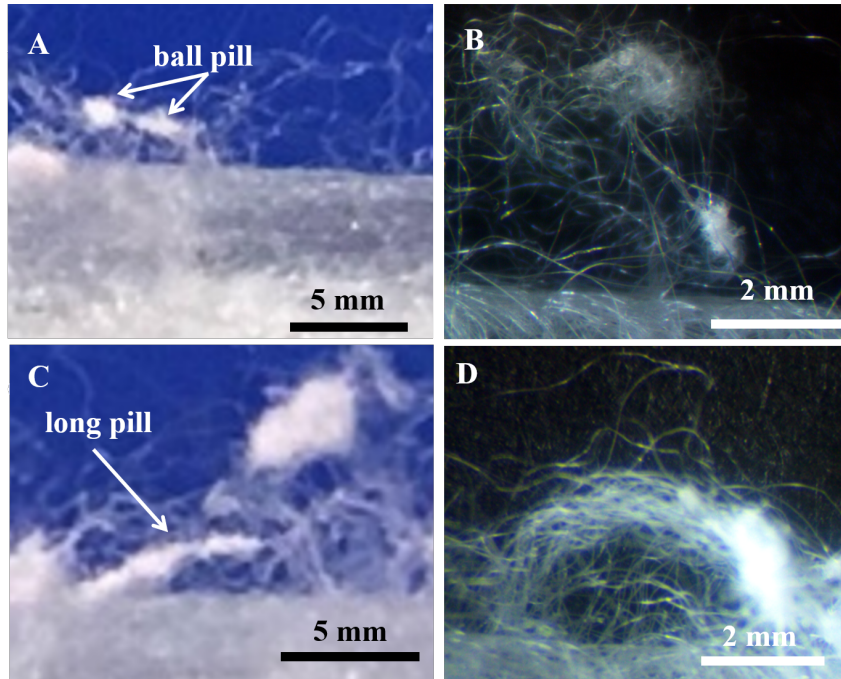


Figure 2.11: Morphology of ball pills [A,B] and long pills [C,D].

fact, all kinds of precursors can often be seen in the vicinity of a partially formed ball pill.

Geometrical considerations suggest that entanglements should be the most appropriate precursor for long pills, but the relative scarcity of these makes it impossible to establish such a correlation from the results of Section 2.3.1. We therefore experimented with different abrasants to find one that generates a preponderance of long pills, the most effective being a small pad of silicone rubber, as shown in Figure 2.12A. Back-and-forth motion of amplitude approximately equal to the length of this pad in the sliding direction ( $\approx 7$  mm) then generates more than 50% entanglement precursors, a typical example being shown in Figure 2.12B. The resulting long pills are shown in Figure 2.12B.

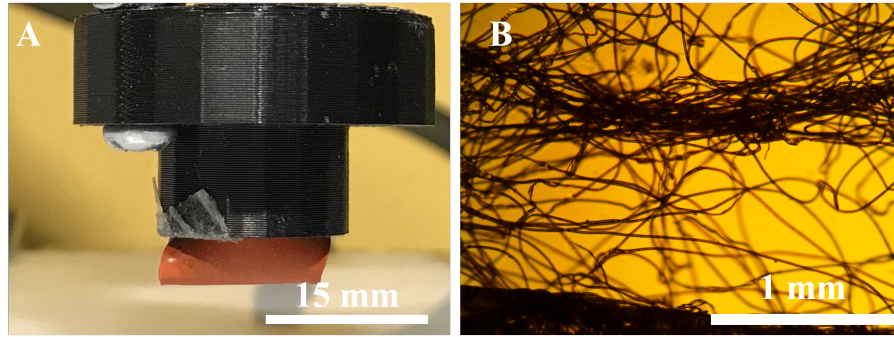


Figure 2.12: Silicone rubber abrasant [A] and resulting entanglements [B].

Long pills generally tend to align with their long axes perpendicular to the direction of sliding, but this conclusion is somewhat modified by fabric anisotropy. Examination of unworn fabric shows that fiber orientation is preferentially aligned with the direction of manufacture. In the early stages of abrasion [Figure 2.13A], long pills tend to align with this direction, indicated by the dashed line. However, as abrasion proceeds they tend to rotate towards an orientation approximately perpendicular to the sliding direction, indicated by the arrow in Figure 2.13B. Notice also that the pills become ‘thicker’ as abrasion proceeds, indicating that more fibers are entangled. These experiments were repeated with 12 different equispaced sliding directions relative to the machine direction, and in all cases long pills tended to become oriented approximately perpendicular to the sliding direction. We also note that the numbers of ball pills and long pills generated was not found to depend upon sliding direction.



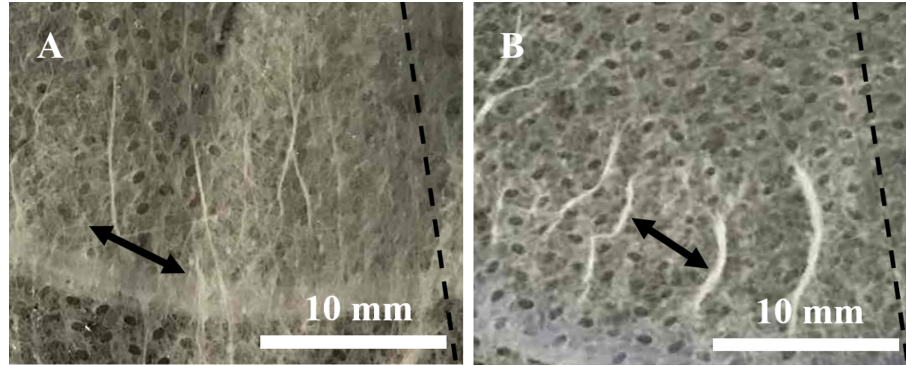


Figure 2.13: [A] Long pills form initially along the machine direction, indicated by the dashed line, but after continued sliding [B], they become approximately perpendicular to the sliding direction, indicated by the arrow.

### 2.3.5 Effect of bonding temperature

The abrasion experiments described so far involve the fabric of Figure 2.4 (A,C) that was manufactured using a bonding temperature of 135 °C. Corresponding experiments on a fabric bonded at a higher temperature of 153 °C show an initial stage of fuzziness, but this does not then typically lead to significant pill formation.

It should be noted however that this improvement in abrasion resistance comes at a cost, in that the resulting fabric is less ‘qualitatively soft’ to the touch, and hence less attractive in applications involving contact with the skin [16], but while the possibility of an optimization between softness and wear resistance is an important question, it is beyond the scope of this paper.

We recall from Section 2.3.2 that abrasion damage for the 135 °C fabric often starts from a Type 4 process [Figures 2.6, 2.7], in which a fiber is detached from one or more bond sites without fiber fracture, and then is pulled out from the fabric. Clearly this process is less likely if the bonding strength is increased.

To test this hypothesis, we performed peel tests on the two fabrics. Several fibers were grasped by a sprung stall clamp and these were then pulled from the fabric

using an Instron machine (5940 Series Single Column Table Top System). Figure 2.14 shows the force-extension curve and representative images at various stages of loading. The maximum force reached is an order of magnitude lower for the 135 °C fabric [Figure 2.14A] than for the 153 °C fabric [Figure 2.14B] and since the fibers are the same for the two fabrics, we attribute this to the greater bond strength achieved at 153 °C. If a fiber becomes detached from a bond site without breakage, it will again contribute to the force once the extension increases sufficiently to take up the slack. This behaviour explains the numerous downward jumps in the force extension curve in Figure 2.14A], and also the greater extension to failure. By contrast, in Figure 2.14B], most of the fibers break at or near the maximum load point.

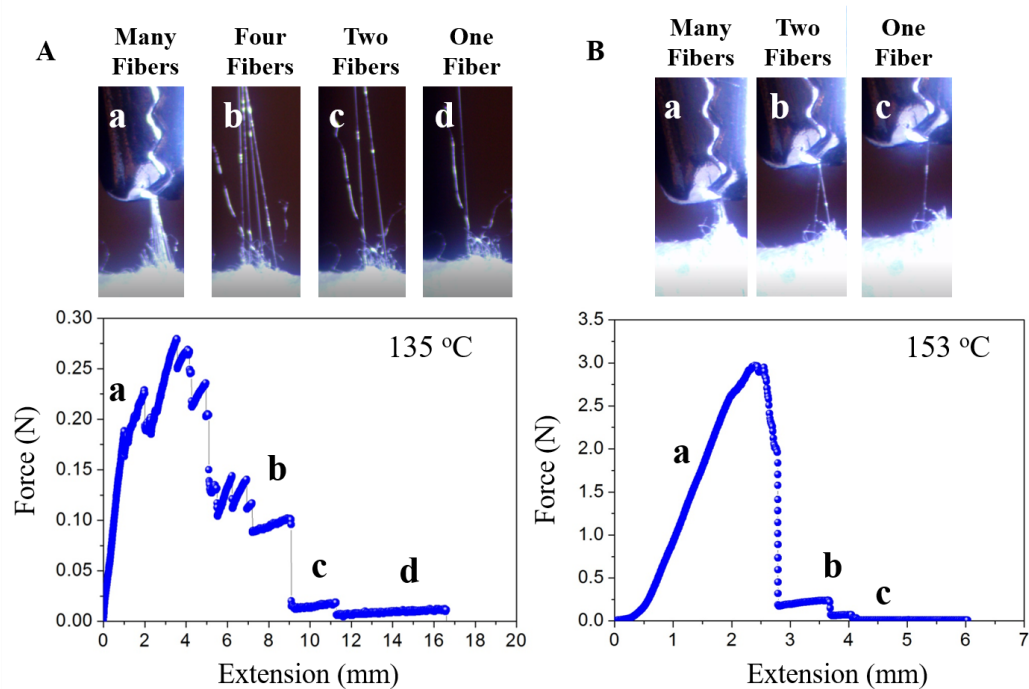


Figure 2.14: Force-extension curves and representative images for peel tests on fabrics bonded at 135 °C (A) and 153 °C (B).

### 2.3.6 Effect of fiber diameter

Since the fabrics tested comprise fibers of very small diameter [ $\approx 20 \mu\text{m}$ ], it might reasonably be hypothesised that intermolecular [e.g. van der Waals'] forces are involved in the development of pills. We therefore performed some ‘qualitative’ experiments on fibers of larger diameter, notably human hair [ $\approx 50 \mu\text{m}$ ] and cotton yarn [ $\approx 1 \text{ mm}$ ]. Rolling a group of these fibers between two fingers, twist and entanglement precursors similar to those in Figure 2.9 are obtained [Figure 2.15(A,B)], and indeed similar morphologies could be obtained even with a 3 mm cable (C). With the cotton yarn, further ‘abrasion’ leads to the development of a ball pill [Figure 2.15(D–F)] if the ends are left free, but a long pill [Figure 2.15(G)] if the ends are fixed. These results suggest that intermolecular forces do not play a significant rôle in pill formation. Friction may also play a significant rôle in the entanglement and self-adhesion of these fibers. We hope to investigate this mechanism in future research.

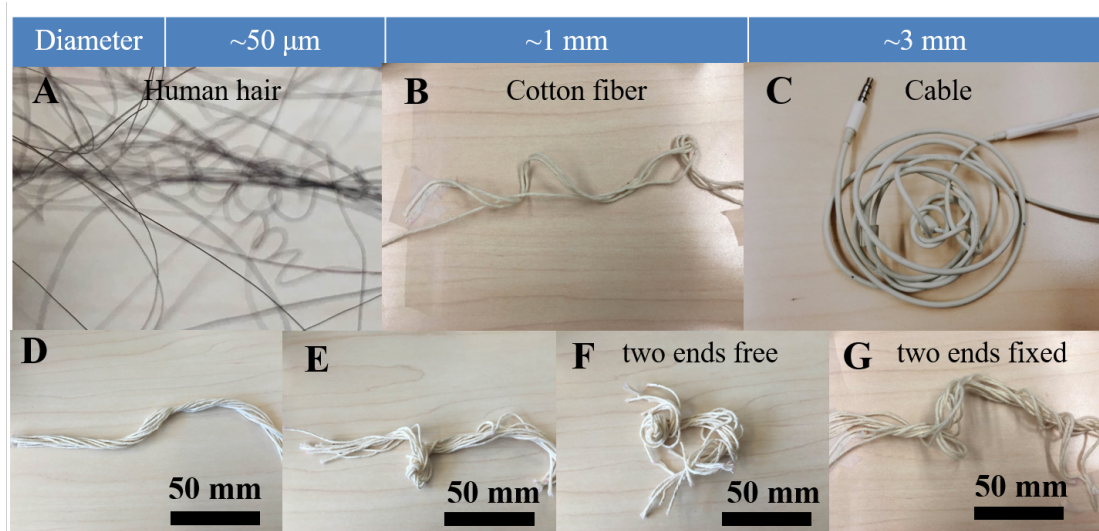


Figure 2.15: Precursor and pill formation for larger diameter fibers.

## 2.4 Conclusions

The development of abrasive damage to a non-woven fabric has been observed using an *in-situ* experimental system. Fuzziness precedes the development of pills and is characterized by pull-out of unbonded fibers or by separation of a fiber from a bond site without fracture. For this reason, increased bond strength obtained by a higher bonding temperature during manufacture reduces abrasion damage.

Various types of pill precursor have been identified. Small amplitude back-and-forth abrasion using a silicone rubber abradant generates ‘entanglement’ precursors, and leads to the development of long pills, with the long axis perpendicular to the direction of motion. Larger amplitude motion with a fibrous abradant generates a wider range of precursors and leads to a predominance of equi-axed ball pills.

Experiments with larger diameter fibers suggest that adhesive forces between fibers is not a significant factor in pill generation.

## CHAPTER III

# Use of Wavelet Analysis for an Objective Evaluation of the Formation of Pills in Nonwoven Fabrics

### 3.1 Introduction

Over the past 40 years, nonwoven fabrics have become an independent and technically sophisticated portion of the textile industry, playing a leading role in many market segments [3]. The global market for nonwoven fabrics is rapidly growing, worth 47 billion in 2018, up from 33 billion in 2013 [61]. The use of non-woven fabrics has increased significantly because they can be produced directly from raw materials, and manufactured in a continuous fashion that avoids complex conventional textile operations such as braiding, weaving or knitting [72, 57, 45]. Non-woven fabrics are used as the basis for more than 10 billion disposable diapers sold every year for infants and toddlers. They are also used for other applications including clothing, filtration products, and seat cushions.

During service both knitted and nonwoven fabrics experience fretting and abrasion. This can lead to damage such as "fuzz", in which fiber ends protrude from the surface of a fabric [4, 40], and "pills", which are balls of tangled fibers held to the surface of the fabric by one or more fibers [4, 40]. This damage is undesirable since it degrades both the appearance and texture of a fabric in consumer applications, as well as reducing the integrity and function in both consumer and industrial

applications. The applications for which non-woven fabrics are used can be just as sensitive to concerns about wear from an appearance or texture perspective, as are the applications for which woven fabrics are used.

The development of pill-resistant fabrics for both woven and non-woven fabrics will require a fundamental understanding of the mechanics of wear mechanisms to understand the formation of pills. However, these mechanisms are expected to be somewhat different for woven and non-woven fabrics. For either case, there is a need to develop quantitative methods to evaluate the formation of pills. While such methods have been developed for woven fabrics, these rely on the underlying periodic structure of the woven fabric. Such periodicity does not occur in non-woven fabrics, and the current industry standard of ASTM 4970 [41] for evaluating pilling requires the subjective opinion of trained experts. The only other technique that has been described in the literature that could be used to evaluate pilling is to scan the surface of a fabric from point to point using a laser, and to detect the presence of pills from changes in the surface topography[86]. However, this entails the use of expensive equipment, and is not very efficient. In this paper we describe a simple digital-image approach that requires a minimal amount of human intervention, and can be used for evaluating pills in non-woven fabrics.

Digital-image analyses have been explored previously for the purpose of identifying pills[54, 83, 84, 82, 87, 70, 69, 38, 47, 48, 51, 49]. However, the inherent challenge with digital-image techniques is developing methods to separate the signals associated with the presence of pills from other confounding signals, such as differences in illumination, unevenness of the fabric surface, and the texture.

One approach is to use a two-dimensional, discrete-Fourier-transform method [83, 84] to separate the periodic structure of woven and knitted fabrics from the

non-periodic structure of pills. However, this technique can only give frequency information over the entire domain, so if, for example, small perturbations or localized features exist, such as isolated pills, they may be missed because the signal is diluted during the transform procedure (Figure 3.1). Furthermore, the method does not give any information about the location of pills. It can only identify whether there are pills in the domain. Finally, it relies on a distinction between the periodic structure of a woven fabric, and the non-periodic structure of pills. Therefore, it cannot be used for identifying pills in non-woven fabrics.

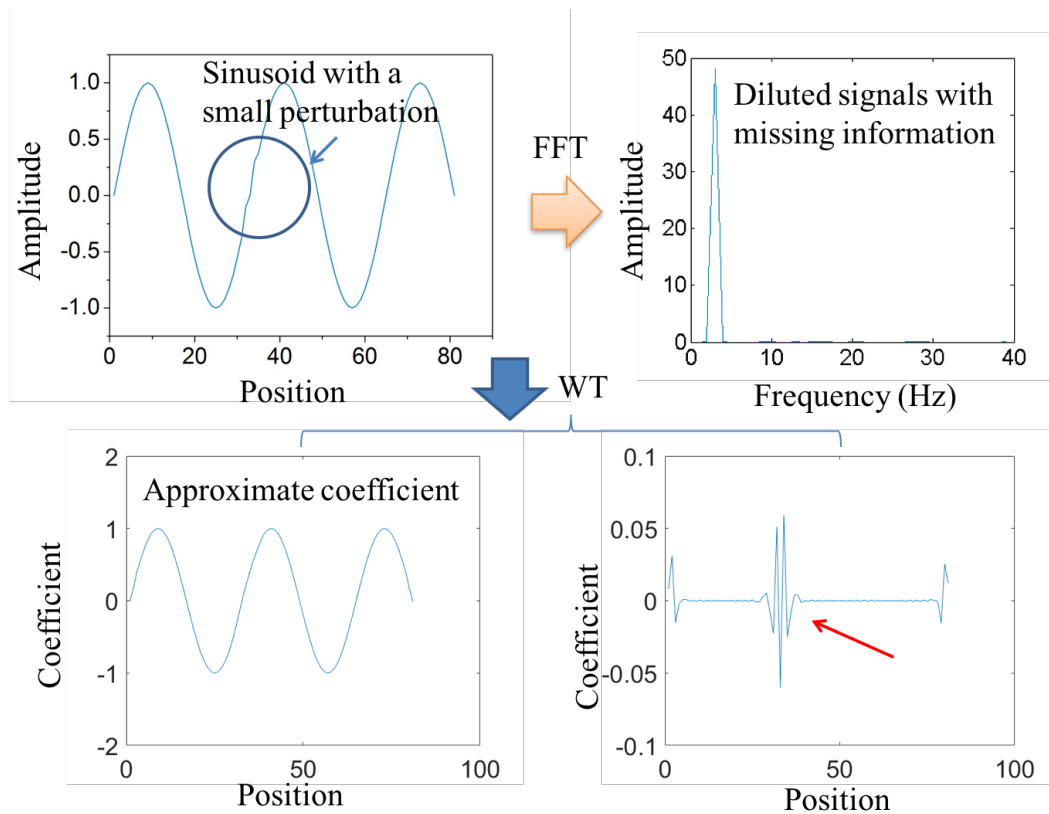


Figure 3.1: Illustration of the difference between a two-dimensional, discrete-Fourier-transform and a two-dimensional, discrete-wavelet transform based on a sinusoid with a small perturbation. The limitation for two-dimensional, discrete-Fourier-transforms is that, since the signal is diluted during the transform, small perturbations or localized features may be missed. In order to capture localized data in both the frequency and spatial domains, a wavelet analysis has been introduced to analyze digital images of fabrics.

To capture localized data in both the frequency and spatial domains, wavelet analyses have been used, mainly for woven or knitted fabrics [82, 87, 70, 69, 38, 47, 48, 51, 49, 23, 54]. One advantage of these techniques is that frequency information is not lost during the inverse transformation. The technique works by describing the digital image in terms of shifted and scaled versions of finite-length or fast-decaying oscillating waveforms called "mother wavelets." Selections of data are compared to the wavelets, producing coefficients that evaluate the degree of matching between the data and wavelets. The presence of a disturbance at a suitable scale, such as a pill, can then be identified.

In previous work, the standard deviation of the matching coefficients for scales that corresponded to the periodic pitch of the fabric was used to quantify the degree of damage. The concept behind this approach is that if data with the periodicity of original pattern are compared to the wavelet, the coefficients will be similar. Therefore, the standard deviation of these coefficients should be relatively small for images of undamaged fabrics. Conversely, if there is a pill on the surface of the fabric, the standard deviation of the coefficients should increase since any pills will disrupt the underlying periodicity of the fabric.

The approach described above relies on the presence of a periodic structure, which may not be present in a nonwoven fabric. By contrast, the technique described in this paper focuses on capturing the pill information directly, rather than the modification of a periodic texture. Although the fabrics used in this study do actually have an underlying pattern associated with the array of bonding pins, this pattern is not used in the analysis. The present approach focuses on an analysis at the scale of the pills that are to be described. So, the analysis is performed at the specific scale associated with the pills, and the signals associated with other scales are removed. This concept



is used to develop a parameter based on a wavelet analysis that provides an objective assessment for the degree of damage.

### 3.2 Reconstruction of pill information

Figure 3.2(A) shows an optical image of a nonwoven fabric before abrasion. The hexagonal close-packed pattern of spots that can be seen is the result of the hot pressing process used to bond the fibers together. Figure 3.2(B) shows an optical image of a similar piece of fabric with a number of pills that formed after abrasion. Although the pills are clearly visible to an observer, it is not obvious how to describe the extent of pilling in a non-subjective fashion. A quantifiable method to describe the pilling, in a fashion that is independent of the perceptions of an observer, was the goal of this study.

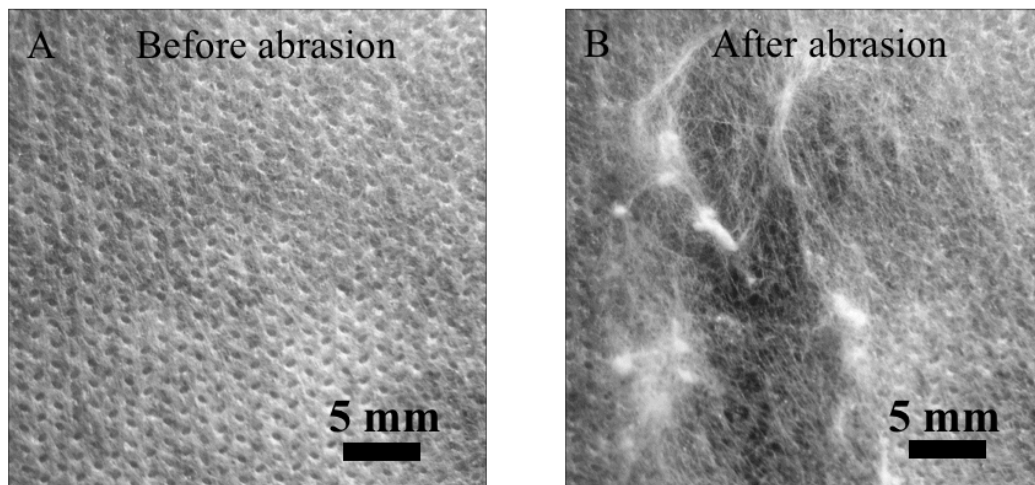


Figure 3.2: (A) Image of fabric before abrasion. The periodic structure that can be observed in this image results from the thermal bonding sites. (B) Image of fabric after abrasion, showing the presence of pills of few millimeters in length. It is these features that our technique focuses on, not the loss of periodicity at the smaller scale.

A wavelet analysis involves correlating a single waveform of a given wavelength, known as the "mother wavelet." with the digital signal of interest. In a fashion similar to Fourier analysis, wavelet analysis involves decomposing the original signal into shifted and scaled forms of the mother wavelet[63]. The process starts with the finest scale of wavelet, and the correlated portion is subtracted from the original signal. The image recreated from the subtracted portion of this first step is referred to as "level 1" in the images that follow. The remnant signal is then operated upon by a wavelet with twice the wavelength of the previous one, and the image recreated from this second signal is referred to as "level 2." This process is repeated until the wavelength of the wavelet applied to the remaining signal is much coarser than any scale of interest. In the present case, seven frequency scales were used, with the finest corresponding to  $1/256th$  of the image length, and the coarsest level corresponding to a quarter of the image length.

The process of correlation and subtraction filters the signal into components that incorporate information about features with characteristic sizes. The effect of this digital manipulation on the image of an abraded sample shown in Fig 3.2(B) is illustrated in Figure 3.3. This figure shows a sequence of images resulting from a wavelet analysis from the final coarse levels (low frequency) to the initial fine levels (high frequency).

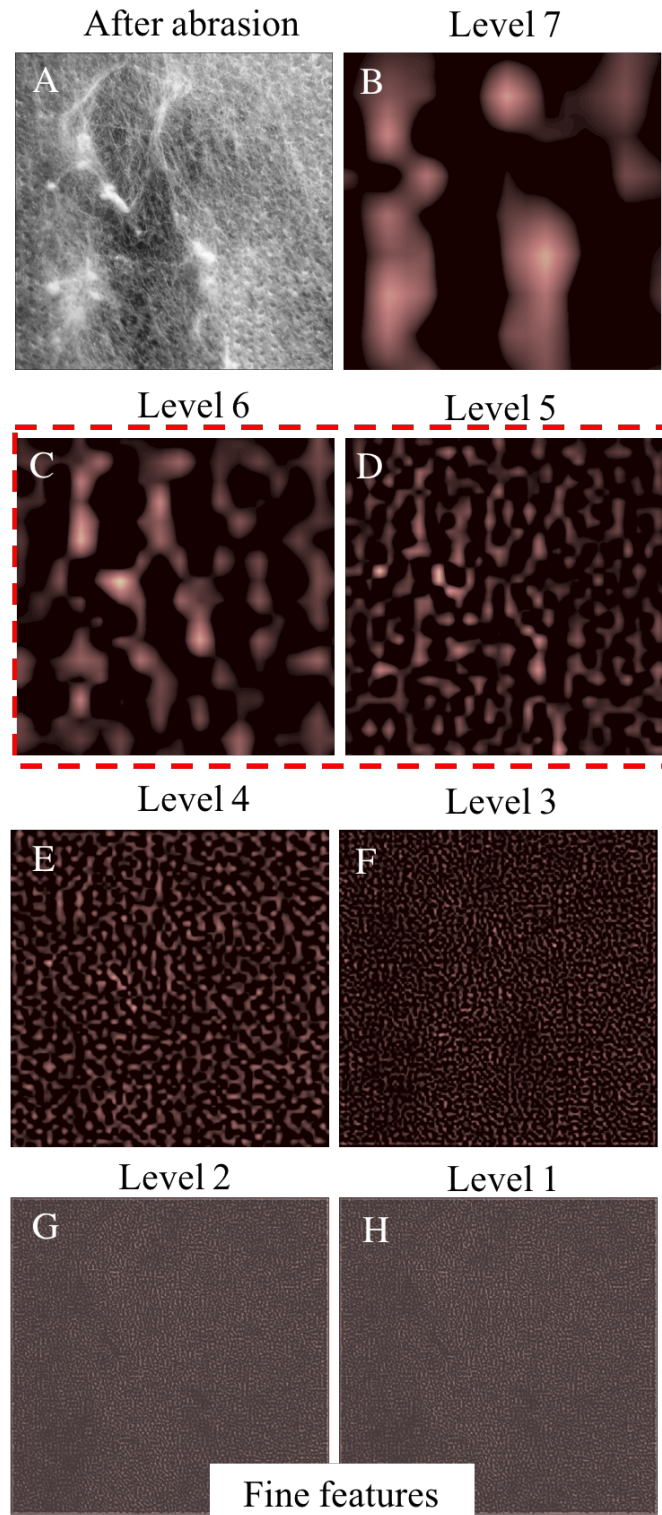


Figure 3.3: (A) Image of non-woven fabric after abrasion; (B-H) Decomposition of the original image after subtraction of the digital information at increasingly fine scales.

The specific form of the wavelet used to generate these images is shown in Figure 3.4. However, it is important to appreciate that the results do not depend on the precise shape of the wavelet chosen.

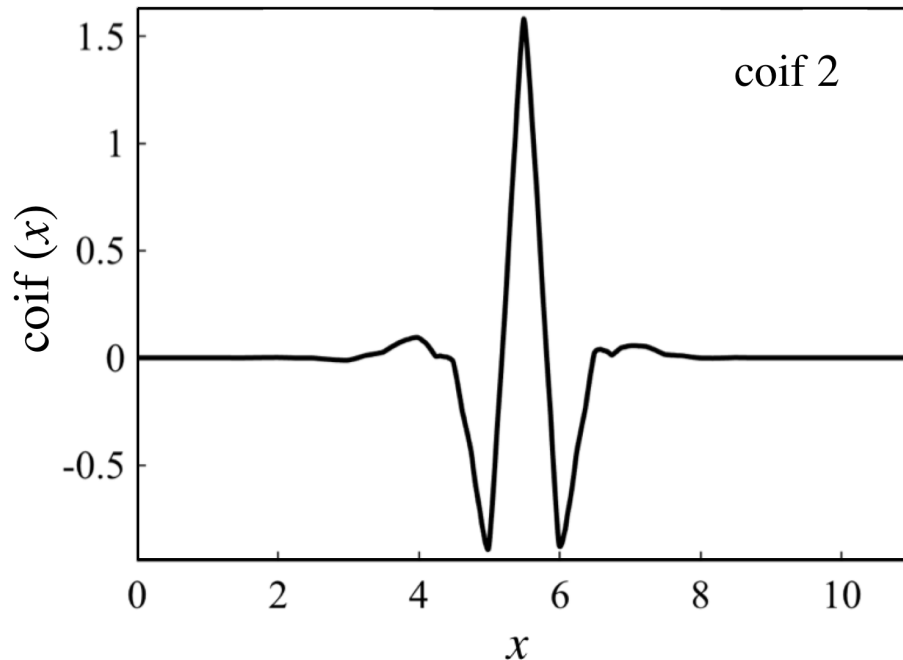


Figure 3.4: The mother wavelet used to create the images of Figure 2.

The major issue of this technique that needs to be addressed is how to determine the level or combination of levels that best characterizes the features of interest, without excessive contamination from other features. This is the only step of the process in which some human intervention is required: determining the appropriate scale of the features. However, once this is decided, the process proceeds by recognizing that each level of wavelet detects features with dimensions that approximately match their wavelengths (Figure 3.5). For example, consider a case in which the physical size of the portion of the fabric contributing to an image is  $a \times a \text{ mm}^2$ , the digital size of the corresponding image is  $m \times m \text{ pixels}^2$ , and the features of interest

have a physical size of  $d$  mm. Since the features of interest in this case are captured by  $m \times d/a$  pixels in the image, a wavelet level of  $N_c$ , given by

$$(3.1) \quad N_c = \log_2\left(\frac{md}{a}\right)$$

will return coefficients whose magnitudes reflect the density of features at this size scale.

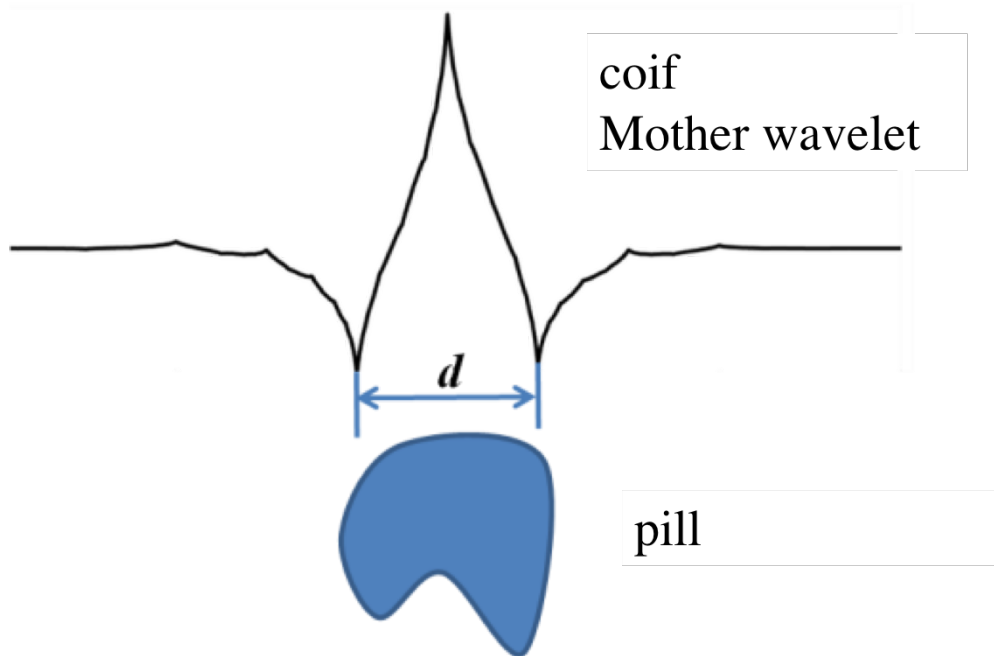


Figure 3.5: Relation between the size of wavelet and the size of pill. If the size of the shifted and scaled version of the wavelet matches the size of pill, the pill information will be picked up by returning a large coefficient.

For the specific sample considered in this paper, the pills that form in the fabric are in the range of 2.5 mm to 5 mm. The images of the fabric were cropped to a size of  $512 \times 512$  pixels<sup>2</sup>. This was found to provide a satisfactory level of resolution, and amenable to a wavelet analysis. The microscope was calibrated so that a digital image of this size image corresponded to a physical domain of  $40 \times 40$  mm<sup>2</sup>. Therefore,

using Eqn.3.1, a level of  $N = 5$  detects features of about  $2.5 \text{ mm}$ , and a level of  $N = 6$  detects features of about  $5 \text{ mm}$ . After the wavelet coefficients at these two levels ( $N= 5, 6$ ) were determined, the coefficients at the other levels were discarded. The chosen coefficients were used to synthesize a new image matrix by an inverse wavelet transform. A visualization of the synthesized image matrix is shown in Figure 3.6(B), and compared to the original unfiltered image, Figure 3.6(A). Notice that the reconstructed image broadly captures the morphology of the pills.

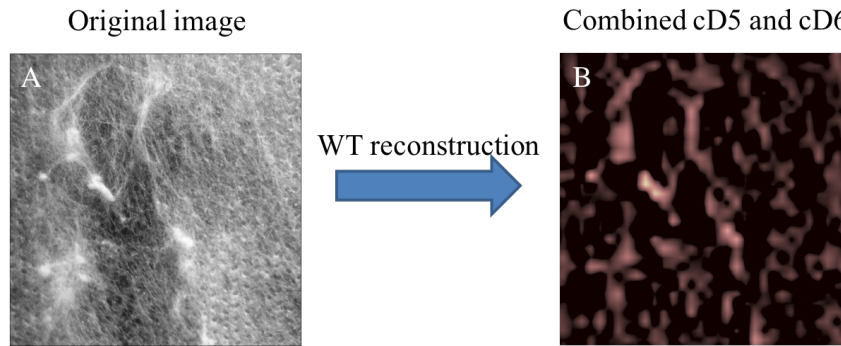


Figure 3.6: Reconstruction of the signals corresponding to levels 5 and 6 results in the image on the right (B). This can be compared to the unfiltered image of the abraded specimen on the left (A) to show that this reconstructed image broadly captures the pills.

The coefficients corresponding to the wavelets at levels 5 and 6 increase in magnitude with an increasing number of pills on a given area of fabric. This motivated the use of a parameter  $P$ , defined as the sum of all positive elements in the coefficient matrix of the synthesized image divided by the total number of the elements in that matrix. It will be shown that this parameter correlates with the extent of damage, in the form of pills, after an abrasion test.

In order to further compare the fabric before and after abrasion,  $P$  was normalized by its initial value,  $P_o$ , obtained from an unworn fabric that would usually be available

as a reference sample. This normalized quantity is identified as the "gray-value ratio":

$$(3.2) \quad \delta = \frac{P}{P_o}$$

It is the gray-value ratio,  $\delta$  that is used to provide a quantitative measure of the damage.

### 3.3 Experimental methods

The hardware used included an optical microscope, a light source consisting of a light-emitting diode, a digital camera, and a computer (Fig 3.7). The magnification of the microscope and the resolution of the camera were matched by a one-time calibration process to ensure that a  $40 \times 40 \text{ mm}^2$  area corresponded to a  $512 \times 512 \text{ pixels}^2$  image.

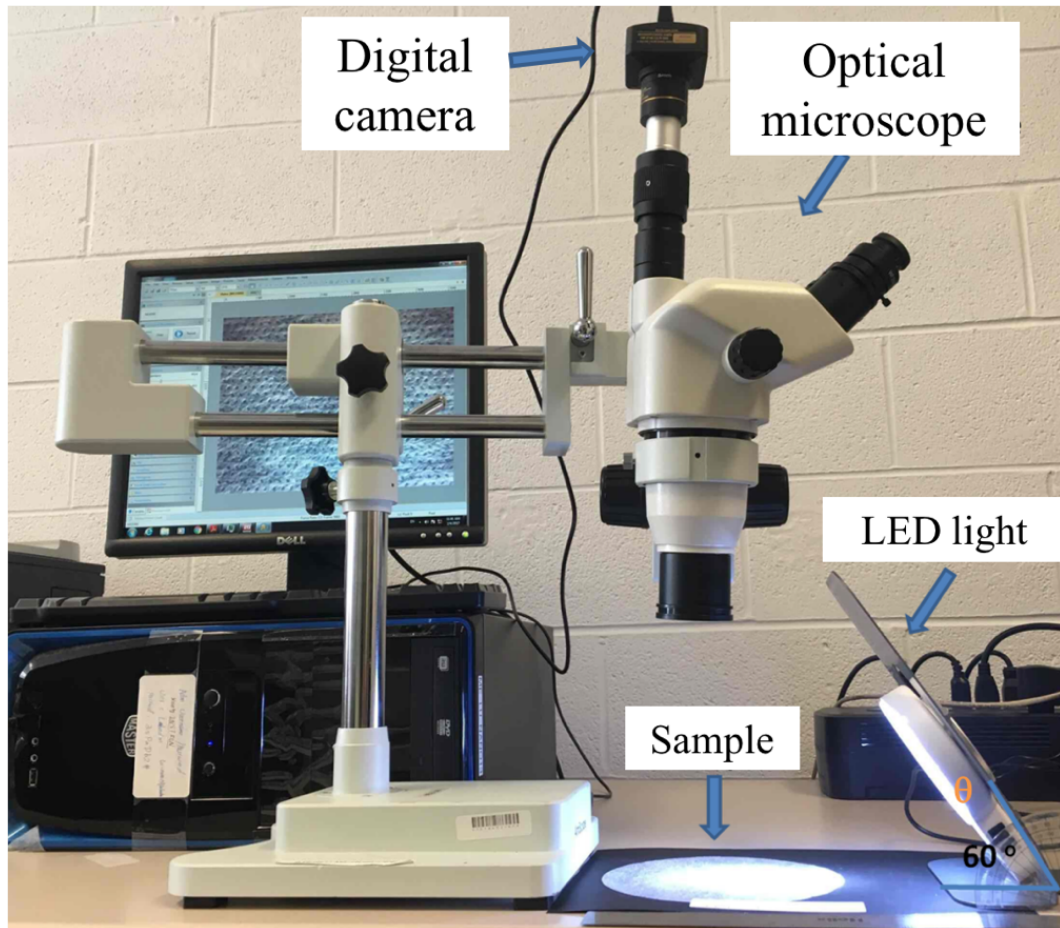


Figure 3.7: Hardware set-up for wavelet analysis. The hardware set-up was composed of an optical microscope, an LED light, a digital camera, and a computer. The magnification of the microscope and the resolution of the camera was matched by a one-time calibration process as described in Section 2. The appropriate magnification of the microscope and camera resolution was such that the region of interest can be imaged to a size of 512 by 512 pixels or larger. This required a digital camera with a resolution of  $0.3 M$  pixels or higher.

The analysis was developed using the computer program MATLAB. First, the image was cropped to a size of  $512 \times 512 \text{ pixels}^2$ , so that it corresponded to the correct area. The image was converted to a gray-scale. As described above, it was determined that the coefficients at the fifth and sixth level would correspond to the



length scales associated with the pills of interest. Then, the coefficients at these levels were extracted by a multilevel,  $2D$ , wavelet-decomposition, and an image containing only the information at these two levels was reconstructed by an inverse wavelet-transform. Finally,  $P$  was obtained, and a similar process was used to obtain  $P_o$  from an undamaged sample, so that the corresponding gray-value ratios could be calculated.

This technique was used on several different surfaces to explore whether it could discriminate between subtle gradations of surfaces that were all nominally white, but clearly had different appearances. Once the discriminatory ability of the technique had been verified, it was applied to micrographs of fabrics that had been worn to different degrees, and compared the ratings we obtained with those of an independent, qualitative evaluation based on ASTM 4970[41].

### 3.4 Results

The gray value,  $P$ , for a pure digital white image that is absolutely uniform, should be zero. However, as shown in Figure 3.8, even nominally untextured surfaces do not have gray values of zero. The gray value contains information about non-uniformities in the image corresponding to the wavelengths of level 5 and level 6. It is interesting that the gray value appears to scale systematically with what an observer might qualitatively describe as a departure from uniformity in the image. In particular, this figure emphasizes the need to normalize gray values by a reference value. In the case of damaged fabrics, the reference value of  $P$  used is that of a nominally undamaged fabric,  $P_o$ .

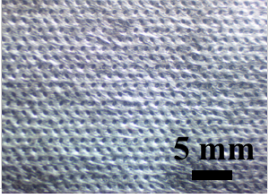
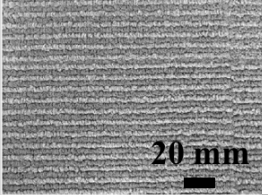
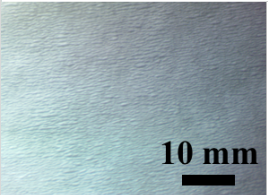
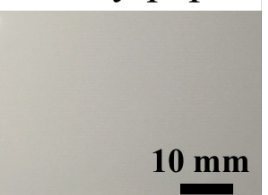

Surface	Gray value
Fabric 	$2.9 \pm 0.3$
Carpet 	$2.4 \pm 0.4$
Tissue paper 	$1.3 \pm 0.1$
Glossy paper 	$0.14 \pm 0.02$
Pure digital white image 	0

Figure 3.8: Gray value,  $P$ , of a pure digital, white image, paper-based materials, and fiber-based materials.

In order to compare our gray-value-ratio rating to a traditional, qualitative rating method[48], the degree of damage on five non-woven fabrics was evaluated by both methods. Fabric samples were abraded on a Martindale abrasion tester by an independent employee at Procter & Gamble, who also read the worn samples using the traditional rating method. For this procedure, the bottom of the non-woven samples was clamped onto a felt layer, and a rubber-covered footer on the top abraded the samples following a Lissajous curve. The resulting damage was then rated by comparing the damage with standard images from 1 (no pilling) to 5 (extreme pilling and destruction of sample). The worn samples were then supplied to the University of Michigan, and evaluated independently by the wavelet analysis described here.

The images were obtained and analyzed as described above, and the results compared with the traditional "Martindale Rating" methods in Figure 3.9. This figure shows that there is excellent consistency between the two methods. The correlation coefficient between the subjective results and the results obtained by the wavelet technique was 0.9025. In conclusion, the technique we have developed not only requires only a limited amount of human interpretation, but also agrees well with the traditional rating method.

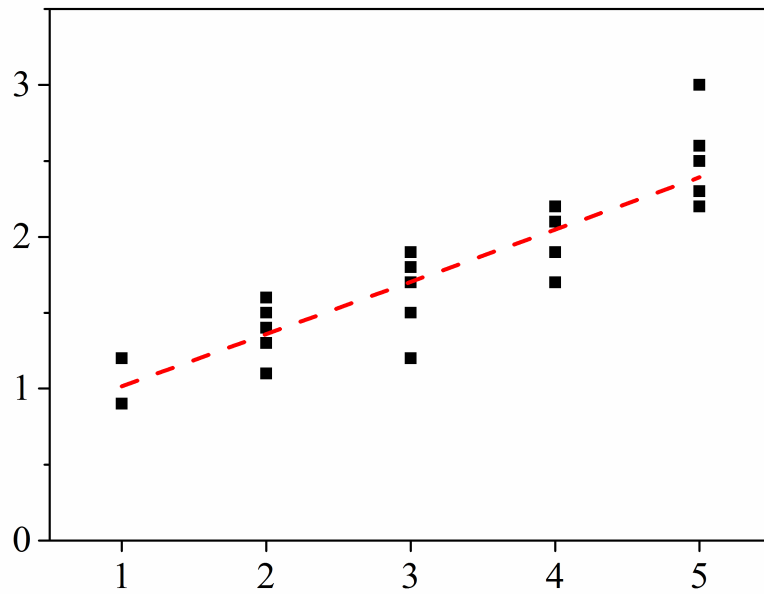


Figure 3.9: The measured gray-value ratio,  $\delta$  correlates well with a traditional rating method. (Independent measurements, the "traditional ratings" are courtesy of P&G.)

### 3.5 Discussion

Two factors that might influence the quantification of wear were also considered: the choice of the mother wavelet, and the rotation of the samples during imaging. To investigate the potential effect of using different forms of wavelet, a range of different wavelets (Figure 3.10) were used to test whether there was any difference in the resultant quantification. The six wavelets chosen came predominately from two wavelet families: Daubechies and Coiflets[22]. The reason for choosing these wavelets was that they are compactly supported and orthonormal, which makes discrete wavelet-analyses practicable[23, 49, 63, 22, 36].

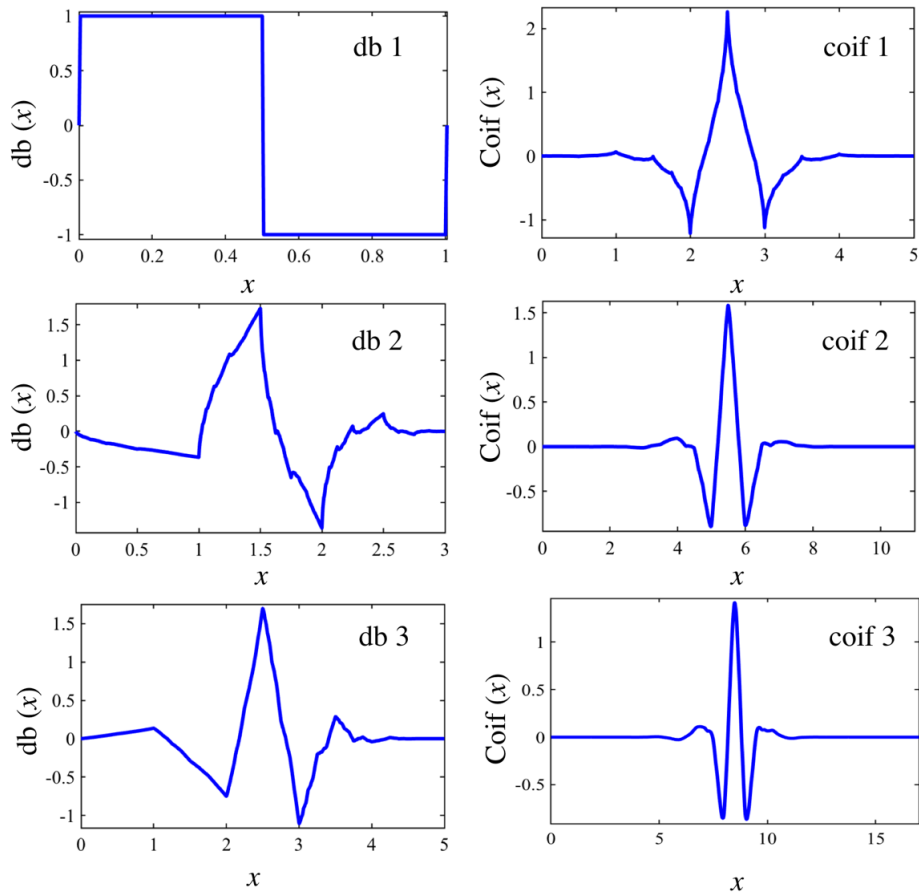


Figure 3.10: Six different mother wavelets used to study the effect of the choice of wavelet.

In addition, other studies have chosen one of these wavelets because they can successfully match the main features of woven fabric textures [82, 47, 48]. The different mother wavelets that we used to detect features of the same size range are shown in Figure 3.10. Similar results were obtained with all forms of the mother wavelets tested (Figure 3.11). The difference in gray-value ratios obtained from all the mother wavelets was only around 4%. Therefore, the choice of wavelet is not critical when investigating pilling in nonwoven fabrics.

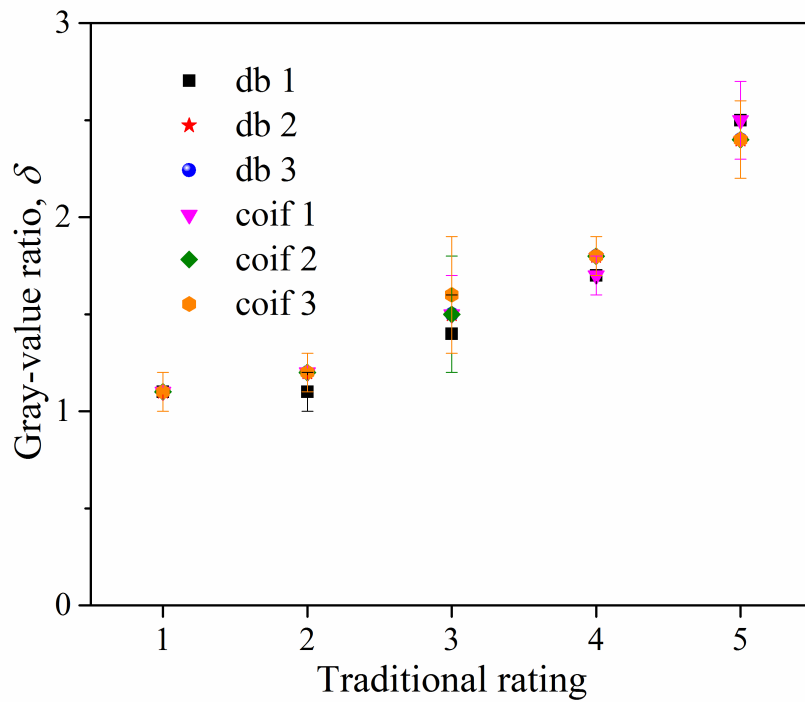


Figure 3.11: In order to further optimize the wavelet analysis for a non-woven fabric, a range of candidate wavelets were used to test the influence of different mother wavelets. The six wavelets chosen were from two wavelet families: Daubechies and Coiflets (see Figure 3.10 in the main text for the key to the shapes of the wavelets). The samples from the five groups analyzed in Figure 3.9 were used for this analysis. The error bars represent one standard deviation for the results from the different samples. The plot shows that the choice of mother wavelet has a negligible effect on the choice of wavelet.

Rotation of the sample should only affect the resulting measurements if the fabric possesses significant anisotropy. Although the periodic structure of nonwoven fabrics is not as obvious as that of woven fabrics, the hexagonal array of the bonding pattern and the manufacturing orientation during fiber lay-down resulted in a certain degree of anisotropy. Also, orientation effects might be introduced by the direction of sliding during abrasion. In order to study this possible effect of anisotropy, we introduced a deliberate rotation into the samples before quantifying the damage. We found that the effect of rotation on the measured gray-value ratio was no more than 6% (Figure

3.12). This lies well within other effects of experimental variability shown in Figure 3.9.

In order to study further how rotation might influence the results, a second experiment was conducted. This experiment involved taking two sheets of white paper, drawing a line in the center of one sheet, and drawing a solid circle in the center of the other sheet. These sheets of paper were rotated through  $0^\circ$ ,  $30^\circ$ ,  $60^\circ$ ,  $90^\circ$ ,  $120^\circ$ ,  $150^\circ$ , and  $180^\circ$ . For the paper with a line, the image was different upon rotation, while the image was invariant for the circle. The difference in gray value for both paper with line and paper with circle before and after rotation was small, also about 4%.

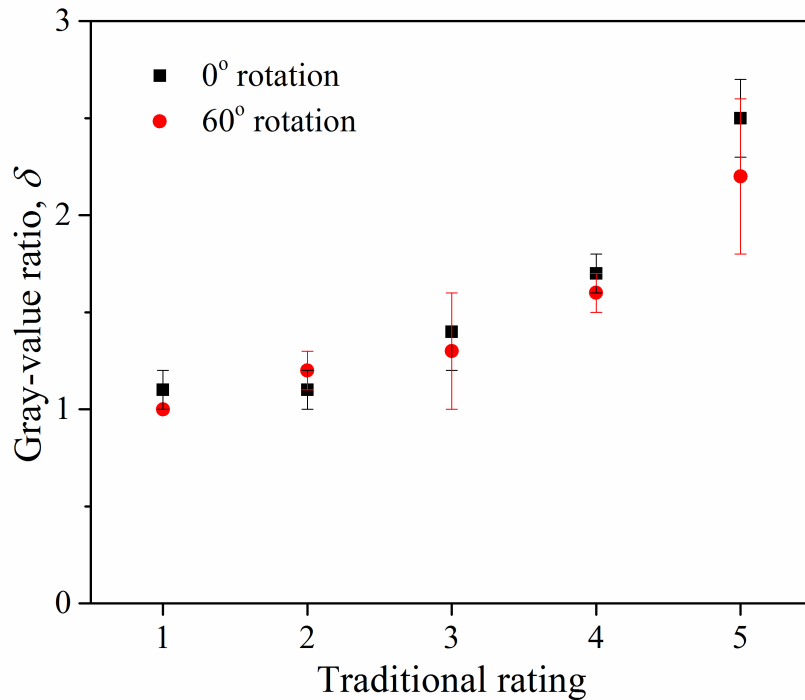


Figure 3.12: Rotation of the fabric had negligible effect on the analysis method. A non-woven does not have as obvious a periodic structure as a woven fabric does. However, for the non-woven fabric in the present studies, there were several factors that could lead to anisotropy. The first was the bonding pattern, which had a hexagonal close packing form. The second was the production orientation, which was along the close packed direction of the bond sites. The third was the wear direction. Despite these effects, the difference of degree of damage before and after rotation was only around 6%. The error bars represent one standard deviation in the variation for the five different specimens analyzed from each of the sets of samples used to obtain the data of Figure 3.9.

### 3.6 Conclusion

A pill-level technique using two-dimensional, discrete-wavelet transforms has been reported to provide an objective measure of pilling for nonwoven fabrics. It has been shown that this approach using the gray-value ratio to quantify pilling correlates very well with a traditional subjective approach. Since the approach we have developed requires minimal human interpretation (human interpretation is needed only during the initial calibration for a specific type of fabric and abrasion conditions),



it is expected that it can form the basis for an automated, integrated and efficient system for evaluation of fabrics within industrial contexts. In addition, it will allow a quantitative description of pilling that can be used for developing wear models.

This method was developed for non-woven fabrics, which lack an underlying periodicity that can be affected by the formation of pills. The loss of periodicity can be used to detect damage in woven fabrics, so the present technique may not be needed for such fabrics. However, it should be noted that the technique could be used for woven fabrics, provided the pills have a scale that can be separated from any underlying scale of the weave pattern. For example, by applying the technique to published images of pills in a knitted fabric[69], it was possible to show that the damage could be quantified by this approach.

## CHAPTER IV

# Generation of Perversions in Fibers with Intrinsic Curvature

### 4.1 Introduction

A recent experimental study of abrasion of non-woven fabrics [78] showed that the formation of pills was generally preceded by individual fiber damage in the form of waviness, twists, kinks and entanglements. Since in general only one side of the fiber is abraded, it seems reasonable to assume that the resulting inelastic deformation leads to a state of intrinsic curvature, and that these shapes are the response of the fiber structure to end constraints or loads.

A simple experiment that illustrates this is as follows: take a hair, a piece of fiber, or a ribbon, keep it taut, and use a finger nail to abrade one surface in a central segment. Now, relax the tension gradually. If the ends were allowed to rotate, the abraded segment would adopt a helical shape, but if they are prevented from rotating it will exhibit two helical segments of opposite chirality separated by a ‘perversion’ [34, 59], as shown in Fig. 4.1.

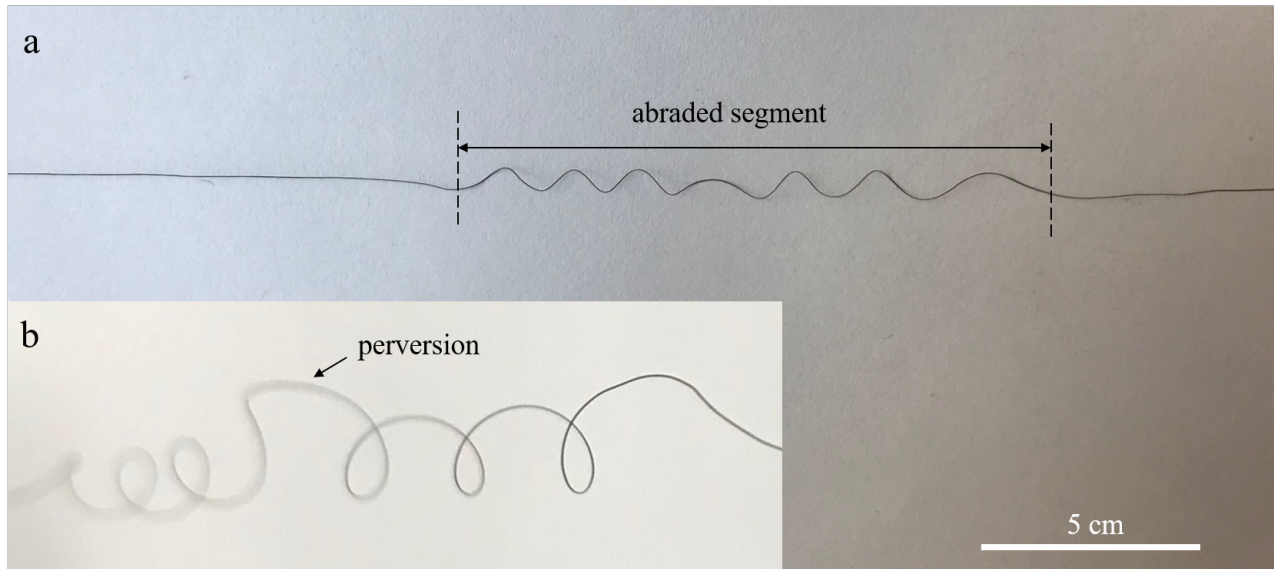


Figure 4.1: (a) The shape of a fiber abraded in a central segment; (b) Enlarged perspective view of the abraded segment showing two helices separated by a perversion.

Long, thin fibers play an important role in many natural and technological systems. Applications range from microstructures such as supramolecular helices [85], nanobelts [25], DNA [62], and polymer chains [81], to macro-structures including animal organs [74], plant tendrils [34, 27, 79], and cables [35].

If a fiber is sufficiently long and thin, its deformation is dominated by bending and twisting, and can be described using the Kirchhoff equations [32, 66, 14]. Analytical solutions exist for an infinitely long fiber under tension or compression without twist [76], and for a fiber with uniform intrinsic curvature under tension deforming into a uniform helix [34, 59, 30]. If a fiber with intrinsic curvature is straightened and the ends are then prevented from rotating during unloading, the requirement that the end-to-end twist be zero causes it to form two equal helices of opposite chirality separated by a perversion, as shown in Fig. 4.1. This was recognized by Darwin, as explained by [71]. Domokos and Healey (2005) investigated and classified the equilibrium configurations for a fiber with intrinsic curvature. They showed that a

state with a single perversion bifurcates stably from the straight configuration as the tension is reduced, and that there are equilibria involving multiple perversions. A more general computational approach for problems of this class was developed by [50].

Goriely and coworkers [59, 34, 31] obtained an approximate description for the shape of a perversion by perturbing the solution for a straight fiber. In particular, they showed that this approach defines a shape that is asymptotically close to the corresponding pure helices. However, it is clear that the shape illustrated in Figure 4.1, as well as those of fibers in abrasion experiments [78], do not generally meet the condition of being almost straight. Therefore, in this paper, we use finite-element solutions and Rayleigh-Ritz approximations to describe the shape of more relaxed fibers. We also show that the resultant shapes are very sensitive to small perturbations in the initial conditions and to the loading history.

## 4.2 Mathematical model

The Kirchhoff model provides a mathematical framework to describe the deformation of a thin fiber in bending and torsion. We assume that the fiber is inextensible, and define a path-length coordinate,  $s$ , such that the location of a point on the fiber is defined by the position vector  $\mathbf{r}(s)$ . We also define a director basis  $\{\mathbf{d}_1(s), \mathbf{d}_2(s), \mathbf{d}_3(s)\}$ , as shown in Figure 4.2, such that  $\mathbf{d}_3(s)$  is the unit vector in direction  $\mathbf{r}'(s)$ , where the prime denotes the derivative with respect to  $s$ . The unit vectors  $\mathbf{d}_1(s)$  and  $\mathbf{d}_2(s)$  are defined so as to align with the principal axes of the cross-section, for which the second moments of area are  $I_1$  and  $I_2$ , respectively. The local curvature and twist of the fiber can be combined in a vector  $\mathbf{k}(s)$ , defined such that

$$(4.1) \quad \mathbf{d}'_i = \mathbf{k} \times \mathbf{d}_i; \quad i = 1, 2, 3.$$

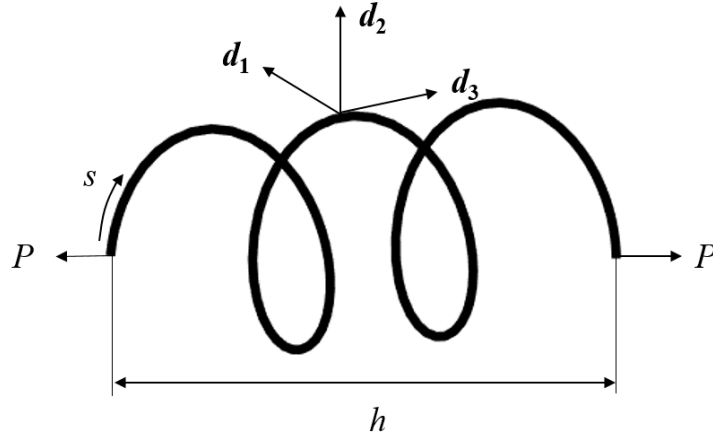


Figure 4.2: A fiber loaded by equal and opposite forces at its ends. We define a path coordinate  $s$  and a director basis  $\{\mathbf{d}_1(s), \mathbf{d}_2(s), \mathbf{d}_3(s)\}$ . We also define the end-to-end distance  $h$ .

In the unloaded state, the shape of the fiber is defined by an intrinsic curvature vector  $\mathbf{k}^{(0)}(s) = \{k_1^{(0)}, k_2^{(0)}, k_3^{(0)}\}$ .

We consider the case where the fiber is loaded only at the ends by equal and opposite forces  $P$ . In this case the equilibrium of internal force  $\mathbf{F}(s)$  and moment  $\mathbf{M}(s)$  leads to the quasistatic Kirchhoff equations

$$(4.2) \quad \mathbf{F}' = \mathbf{0} ; \quad \mathbf{M}' + \mathbf{d}_3 \times \mathbf{F} = \mathbf{0}$$

[59]. The moment  $\mathbf{M}(s)$  is related to the local curvature  $\mathbf{k}(s)$  by the constitutive relation

$$(4.3) \quad \mathbf{M} = EI_1(k_1 - k_1^{(0)})\mathbf{d}_1 + EI_2(k_2 - k_2^{(0)})\mathbf{d}_2 + GK(k_3 - k_3^{(0)})\mathbf{d}_3 ,$$

where  $E$  is Young's modulus,  $G$  is the shear modulus, and  $K$  is the torsional stiffness. If this is substituted into equations (4.2), it is clear that we will have six ordinary differential equations for the six unknowns  $k_1, k_2, k_3, F_1, F_2$  and  $F_3$ .

#### 4.2.1 Dimensionless formulation

It is convenient to introduce dimensionless measures  $\tilde{s}, \tilde{\mathbf{F}}, \tilde{P}, \tilde{\mathbf{M}}, \tilde{\mathbf{k}}$  through the definitions

$$(4.4) \quad s = \tilde{s}/k_o; \quad \mathbf{F} = \tilde{\mathbf{F}}EI_1k_o^2; \quad P = \tilde{P}EI_1k_o^2; \quad \mathbf{M} = \tilde{\mathbf{M}}EI_1k_o; \quad \mathbf{k} = \tilde{\mathbf{k}}k_o,$$

where  $k_o$  is an appropriate scalar measure of intrinsic curvature or twist. Since the numerical calculations that we discuss later are dynamic in nature, we will also introduce a non-dimensional form,  $\tilde{t}$ , for time

$$(4.5) \quad t = \tilde{t}L\sqrt{E/\rho},$$

where  $\rho$  is the density of the fibers. The Kirchhoff equations (4.2) retain the same form with this substitution, and the constitutive relation reduces to

$$(4.6) \quad \tilde{\mathbf{M}} = (\tilde{k}_1 - \tilde{k}_1^{(0)})\mathbf{d}_1 + \Lambda(\tilde{k}_2 - \tilde{k}_2^{(0)})\mathbf{d}_2 + \Gamma(\tilde{k}_3 - \tilde{k}_3^{(0)})\mathbf{d}_3,$$

where  $\Lambda = I_2/I_1$  and  $\Gamma = GK/EI_1$ .

From the equilibrium equation (4.2) and the constitutive law (4.6), we can obtain a relationship between  $k_1, k_2$  and  $k_3$ :

$$(4.7) \quad \Gamma \left( \tilde{k}_3' - \tilde{k}_3^{(0)'} \right) - \left( \tilde{k}_1 - \tilde{k}_1^{(0)} \right) \tilde{k}_2 + \Lambda \left( \tilde{k}_2 - \tilde{k}_2^{(0)} \right) \tilde{k}_1 = 0,$$

where the prime now represents the derivative with respect to  $\tilde{s}$ .

In this paper, we restrict attention to incompressible fibers of circular cross-section with uniform intrinsic curvature, so that

$$(4.8) \quad \mathbf{k}^{(0)} = \left\{ k_1^{(0)}, 0, 0 \right\}; \quad \Lambda = 1; \quad \Gamma = \frac{2}{3}.$$

If we further choose  $k_o = k_1^{(0)}$ ,

$$(4.9) \quad \tilde{k}_3' = -\frac{3}{2}\tilde{k}_2,$$

and the problem is completely characterized by the dimensionless parameters  $\tilde{P}$  and  $k_1^{(0)}L$ , where  $L$  is the length of the fiber.

In this paper, we will also use the result that the elastic strain energy per unit length,  $U$ , is given by

$$(4.10) \quad \tilde{U} \equiv \frac{U}{EI_1 k_0^2} = \frac{1}{2}(\tilde{k}_1 - 1)^2 + \frac{1}{2}\tilde{k}_2^2 + \frac{1}{3}\tilde{k}_3^2.$$

### 4.3 Uniform helix solution

If the ends of a long fiber are pulled apart by a force  $P$ , and are not restrained against rotation, the fiber forms a uniform helix except for a region near the ends. The dimensionless curvature  $\tilde{k}_1$  and twist  $\tilde{k}_3$  of a pure helix are independent of  $\tilde{s}$ , and hence  $\tilde{k}_2 = 0$  from Eqn. 4.9.

The shape of the helix is defined by two parameters: a length scale such as the pitch  $p$  or the coil radius  $r$ , and a dimensionless parameter which could be any one of the helix angle  $\alpha$ , the ratio  $p/r$  or  $h/L$ , where the end-to-end distance  $h$  is defined in Fig. 4.2. Here the curvature  $k_1$  and twist  $k_3$  are chosen as the two parameters, in terms of which [67],

$$(4.11) \quad \hat{h} = \frac{h}{L} = \frac{k_3}{\sqrt{k_1^2 + k_3^2}}.$$

This equation retains the same form when it is expressed in terms of the non-dimensional parameters  $\tilde{k}_1$ ,  $\tilde{k}_2$  and  $\tilde{k}_3$ .

We can express all the variables in terms of  $\tilde{k}_1$  and  $\tilde{k}_3$ . 1. pitch  $p$  and radius  $r$

$$(4.12) \quad p = \frac{k_3}{k_1^2 + k_3^2} \quad r = \frac{k_1}{k_1^2 + k_3^2}$$

The total energy per unit length  $\Pi$  consists of the strain energy,  $U$ , and the potential energy,  $-Ph/L$ , of the applied force  $P$ . The dimensionless total energy for

the uniform helix is therefore [34]:

$$(4.13) \quad \tilde{\Pi} = \tilde{U} - \tilde{P}\hat{h} = \frac{1}{2}(\tilde{k}_1 - 1)^2 + \frac{1}{3}\tilde{k}_3^2 - \tilde{P}\hat{h}$$

from equation (4.10). An equilibrium configuration is one that minimizes the total energy, with

$$(4.14) \quad \frac{d\tilde{\Pi}}{d\tilde{k}_1} = 0; \quad \frac{d\tilde{\Pi}}{d\tilde{k}_3} = 0.$$

Since from equation (4.13) and (4.11), we have

$$(4.15) \quad \tilde{\Pi} = \frac{1}{2}(\tilde{k}_1 - 1)^2 + \frac{1}{3}\tilde{k}_3^2 - \tilde{P} \frac{\tilde{k}_3}{\sqrt{\tilde{k}_1^2 + \tilde{k}_3^2}}$$

Therefore,

$$(4.16) \quad \frac{d\tilde{\Pi}}{d\tilde{k}_1} = \tilde{k}_1 - \tilde{k}_0 + \frac{\tilde{P}\tilde{k}_3\tilde{k}_1}{(\tilde{k}_3^2 + \tilde{k}_1^2)^{3/2}} = 0$$

$$(4.17) \quad \frac{d\tilde{\Pi}}{d\tilde{k}_3} = \frac{2}{3}\tilde{k}_3 - \frac{\tilde{P}\tilde{k}_1^2}{(\tilde{k}_3^2 + \tilde{k}_1^2)^{3/2}} = 0$$

From (4.14) and (4.17), we have

$$(4.18) \quad \tilde{k}_1^2 - \tilde{k}_1 + \frac{2}{3}\tilde{k}_3^2 = 0$$

from (4.18),

$$(4.19) \quad \tilde{k}_3^2 = \frac{3}{2}(\tilde{k}_1 - \tilde{k}_1^2)$$

from (4.17), we have

$$(4.20) \quad \frac{2}{3}\tilde{k}_3 = \frac{\tilde{P}\tilde{k}_1^2}{(\tilde{k}_3^2 + \tilde{k}_1^2)^{3/2}}$$

$$(4.21) \quad \frac{4}{9}\tilde{k}_3^2 = \frac{\tilde{P}^2\tilde{k}_1^4}{(\tilde{k}_3^2 + \tilde{k}_1^2)^3}$$



$$(4.22) \quad \frac{4}{9} \tilde{k}_3^2 (\tilde{k}_3^2 + \tilde{k}_1^2)^3 = \tilde{P}^2 \tilde{k}_1^4$$

from (4.19) and (4.22), we have

$$(4.23) \quad \frac{4}{9} \left( \frac{3}{2} (\tilde{k}_0 \tilde{k}_1 - \tilde{k}_1^2) \right) \left( \left( \frac{3}{2} (\tilde{k}_0 \tilde{k}_1 - \tilde{k}_1^2) \right) + \tilde{k}_1^2 \right)^3 = \tilde{P}^2 \tilde{k}_1^4$$

$$(4.24) \quad (\tilde{k}_0 - \tilde{k}_1) (3\tilde{k}_0 - \tilde{k}_1)^3 = 12\tilde{P}^2$$

This is the final results of  $\tilde{k}_1$  as a function of  $\tilde{P}$ , but I can not have an explicit form. So I solve the  $\tilde{k}_1$  numerically using Matlab ‘vpasolve’. These equations permit all the dimensionless parameters to be expressed in terms of  $\tilde{k}_1$ , and we obtain

$$(4.25) \quad \tilde{P} = \sqrt{\frac{(1 - \tilde{k}_1)(3 - \tilde{k}_1)^3}{12}}; \quad \tilde{k}_3 = \sqrt{\frac{3}{2}(\tilde{k}_1 - \tilde{k}_1^2)}; \quad \tilde{U} = \frac{1 - \tilde{k}_1}{2}$$

[59]. The relations between the normalized curvature,  $\tilde{k}_1$ , twist,  $\tilde{k}_3$ , force,  $\tilde{P}$ , strain energy,  $\tilde{U}$ , and the end-to-end distance,  $\hat{h}$ , are plotted parametrically in Fig. 4.3.

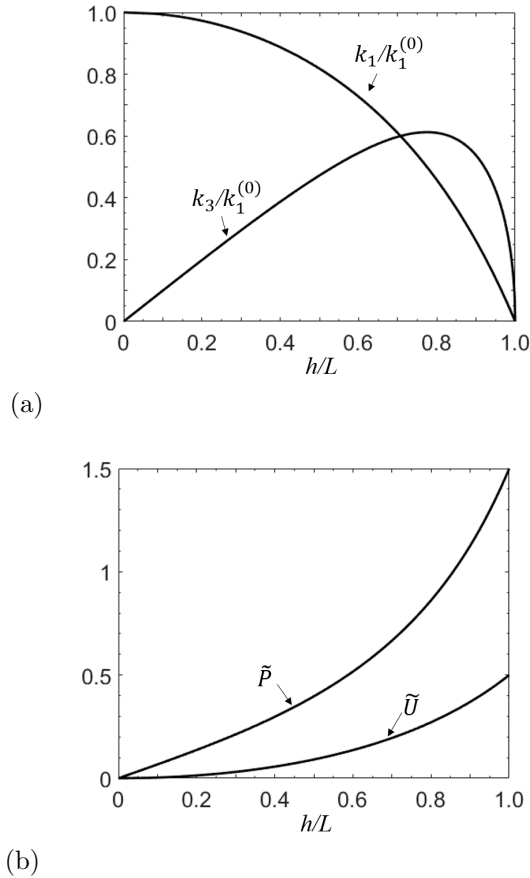


Figure 4.3: (a) Normalized curvature  $\tilde{k}_1$  and twist  $\tilde{k}_3$ , and (b) force  $\tilde{P}$  and strain energy  $\tilde{U}$  for a uniform helix as functions of end-to-end distance  $h/L$ .

#### 4.4 Shape of the perversion

When the tensile force at the end of the fiber is zero, it forms a coil in a plane. Then, as mentioned previously, after the fiber has been pulled into a straight configuration, and the rotation of the ends is prevented as the force  $P$  is reduced again, the fiber deforms into two similar helices of opposite handedness separated by a perversion, as shown in Fig. 4.1. If  $h/L$  is only slightly less than unity, an analytical approximation to the shape of the perversion can be obtained by perturbation methods [59]. For lower values of  $h/L$ , a numerical solution must be used. We will also demonstrate the use of a Rayleigh-Ritz approach in the next section.

Finite-element simulations were conducted using the software ‘ABAQUS/Explicit’ with elastic-beam elements.<sup>1</sup> The ratio between the fiber diameter and length was chosen to be very small ( $10^{-3}$ ), in order to render extensional effects negligible. The quasi-static condition was satisfied by verifying that the kinetic energy was negligible compared to the strain energy throughout the simulation. Automatic time increments and a small damping coefficient were used. A Python script was written to establish the shape of fiber by integrating the curvature. The initial set of numerical results that will be presented were obtained under quasi-static conditions, for which the kinetic energy was always negligible compared to the strain energy. This condition was relaxed in a subsequent set of calculations conducted to explore the effects of rate and noise on the formation of perversions.

To test the accuracy of the finite-element solution, we allowed end rotation so that the shape was a pure helix, except near the ends. The strain energy of a central helical segment is compared to that of the analytical solution in Fig. 4.4, and shows excellent agreement. Notice that in this figure and throughout this section, we present results as functions of  $h/L$  in a helical segment rather than as functions of the force  $\tilde{P}$ , since values for  $h/L$  show less variance than those for  $\tilde{P}$  in the finite-element solutions. The two parameters are related through Eqns. 4.15 and 4.19, which can be solved to give

$$(4.26) \quad \tilde{P} = \frac{6h/L}{(3 - h^2/L^2)^2}.$$

---

<sup>1</sup>A mesh size of about  $0.03k_1^{(0)}$  was used, but a reasonable level of insensitivity to this choice was verified. A similar insensitivity to the choice of damping coefficient was also verified by using values of 0.06 and 0.6. Unless specified otherwise,  $d\tilde{h}/d\tilde{t} = 9.7 \times 10^{-7}$  so as to ensure quasi-static conditions.

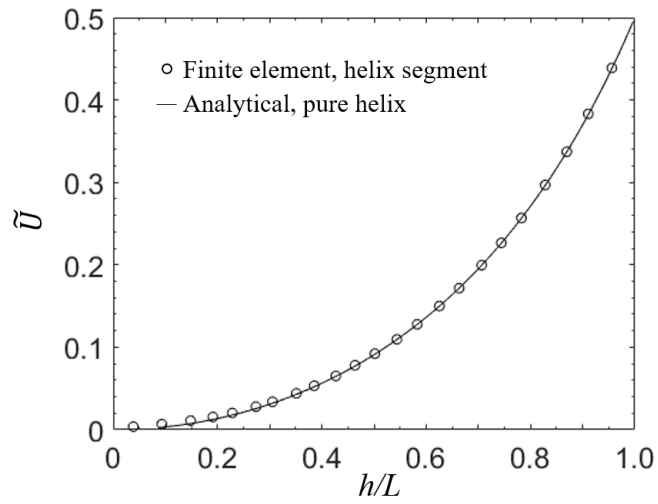


Figure 4.4: The normalized strain energy of a helix segment as a function of the end-to-end distance from finite-element calculations (points) and the analytical solution from Eqn. 4.19(line). The numerical uncertainties in this plot are smaller than the data points.

Figure 4.5 shows two views of the shape of a perversion generated in ABAQUS for the case where  $h/L = 0.78$  for the adjacent helical segments. However, it is easier to characterize the properties of the perversion by plotting  $\tilde{k}_1$ ,  $\tilde{k}_2$  and  $\tilde{k}_3$  as functions of  $\tilde{s}$ .

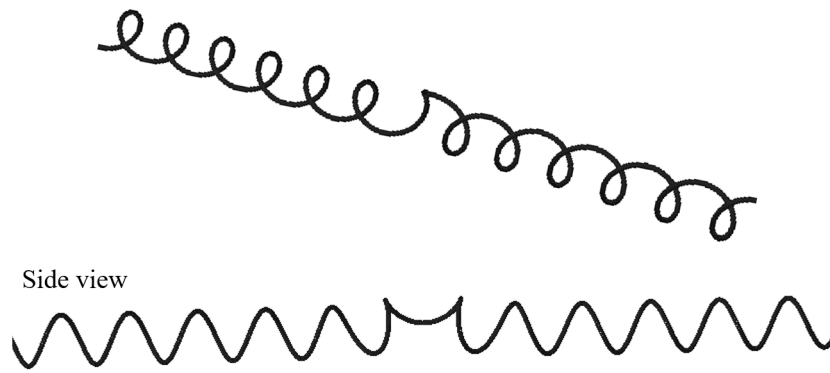


Figure 4.5: Two views of a typical ABAQUS output showing helical coils of opposite chirality separated by a perversion.  $h/L = 0.78$ .

Figure 4.6(a) shows this plot for the case  $h/L = 0.88$ , where the finite-element results are plotted as points. The curvatures  $\tilde{k}_1, \tilde{k}_2$  are symmetric about the midpoint of the perversion, whereas the twist  $\tilde{k}_3$  is anti-symmetric. The finite-element results tend asymptotically to the appropriate values of a pure helix away from the midpoint of the perversion, and the decay is fairly rapid, implying that the form of the perversion is not influenced by the necessarily finite length of the fiber. There is also a noticeable ‘overshoot’ implying oscillatory decay, particularly in the results for  $\tilde{k}_3$ .

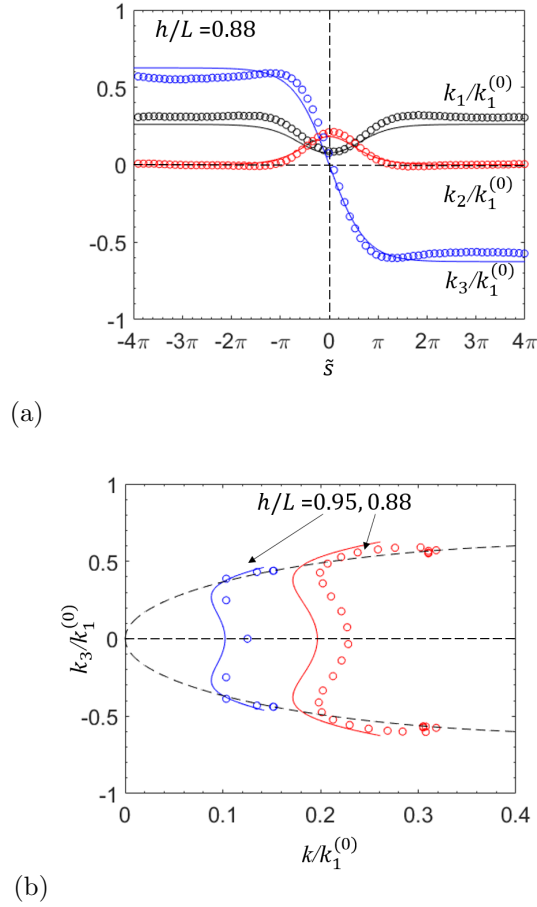


Figure 4.6: (a) Finite-element results (points) for  $\tilde{k}_1$ ,  $\tilde{k}_2$  and  $\tilde{k}_3$  in the perversion segment as functions of  $\tilde{s}$  for  $h/L = 0.88$ . The solid lines are obtained from McMillan and Goriely's perturbation solution for a value of  $\mu = -0.19$ , corresponding to  $h/L = 0.88$ . (b) The same results plotted in  $\tilde{k}_3 - \tilde{k}$  space, where  $\tilde{k} = \sqrt{\tilde{k}_1^2 + \tilde{k}_2^2}$ . The dashed line represents the locus of fixed points defined by the pure helix relation (4.19)<sub>2</sub>. We also present a similar comparison for  $h/L = 0.95$  (corresponding to  $\mu = -0.095$ ), for which the agreement with the perturbation solution is much closer. The numerical uncertainties in this plot are smaller than the data points.

For comparison, the solid lines in Fig. 4.6(a) were obtained using McMillan and Goriely's perturbation solution [59], though we note that the corresponding value of their parameter  $\mu$  is  $-0.19$  (equivalent to  $h/L = 0.88$ ), is outside the range in which they would claim the perturbation procedure provides a good approximation. In particular, notice that the perturbation solution does not capture the oscillatory decay observed in the numerical results.

In Figure 4.6(b), the same results are plotted in  $\tilde{k}_3 - \tilde{k}$  space, where  $\tilde{k} = \sqrt{\tilde{k}_1^2 + \tilde{k}_2^2}$  is the magnitude of the curvature. The dashed line represents the locus of fixed points defined by the relationship for a pure helix (Eqn. 4.19). In this figure, we also show the same comparison for  $h/L = 0.95$  ( $\mu = -0.095$ ), confirming that the perturbation solution gives a much better fit as  $h/L$  approaches unity.

#### 4.4.1 Rayleigh-Ritz approximation to the shape

In their bifurcation analysis to determine the stability of small perturbations from the straight configuration, Domokos and Healey (2005) defined a vector of labels  $w_i \in \{-1, 0, 1\}$ , each component of which essentially characterizes the chirality of a helical segment comprising a single coil of the initial undeformed fiber. The sequence of values  $w_i$  then defines the approximate shape of the deformed fiber. In particular, perversions are identifiable as locations where adjacent segments have opposite values of  $w_i$ .

In our formulation, the chirality of a fiber segment is defined by  $\text{sgn}(\tilde{k}_3(\tilde{s}))$  and a closely related approximation to the shape could be defined by representing  $\tilde{k}_3(\tilde{s})$  as a piecewise constant function. This is equivalent to idealizing the perversion as a point defect, which could lead to useful simplifications in the investigation of more complex patterns. There are clear parallels here with dislocations, and in particular with geometrically necessary dislocations [6, 65], since we have already remarked that at least one perversion must exist under the conditions of loading such as those in Figure 3.1. Dislocation is a concept in material science, it is a defect in the crystal structure which contains the sudden change in the arrangement of atoms. The movement of dislocations allows atoms to glide or slip over each other at low stress

levels.

However, a step function in  $\tilde{k}_3(\tilde{s})$  implies a locally infinite value of  $\tilde{k}_2(\tilde{s})$  from Eqn. 8, and hence implies a non-integrable singularity in strain-energy density. Of course, a similar problem is encountered with a discrete dislocation, and it can be avoided by using an appropriate regularization. For example, in the Peierls-Nabarro dislocation model [43], the relative displacement of the two halves of the crystal is approximated by an arctan function. In the next section, we shall propose appropriate regularizations for the functions  $\tilde{k}_1(\tilde{s}), \tilde{k}_2(\tilde{s}), \tilde{k}_3(\tilde{s})$  near a perversion, and determine the values of the corresponding parameters using the Rayleigh-Ritz method.

### 3.1. Rayleigh-Ritz approximation to the shape

The results in Fig. 4.6 that the functions  $\tilde{k}_1(s), \tilde{k}_2(s)$  might be approximated by

$$(4.15) \quad \tilde{k}_1(\tilde{s}) = a_1 \exp(-b_1 \tilde{s}^2) \cos(c_1 \tilde{s}) + \tilde{k}_1^{\text{helix}}(\hat{h})$$

$$(4.16) \quad \tilde{k}_2(\tilde{s}) = a_2 \exp(-b_2 \tilde{s}^2) \cos(c_2 \tilde{s}),$$

where  $\tilde{k}_1^{\text{helix}}(\hat{h})$  corresponds to the uniform helix value plotted in Fig. 3(a) and  $a_1, b_1, c_1, a_2, b_2, c_2$  are parameters to be determined. These expressions tend asymptotically to the uniform helix values from Eqns. 10 and 13 with increasing  $|\tilde{s}|$ .

Equation (4.9) can be integrated to give

$$(4.17) \quad \tilde{k}_3(\tilde{s}) = -\frac{3}{2} \int_0^{\tilde{s}} \tilde{k}_2(\tilde{s}) d\tilde{s} = -\frac{3\sqrt{\pi}a_2}{4\sqrt{b_2}} \exp\left(-\frac{c_2^2}{4b_2}\right) \Re\left\{\text{erf}\left(\sqrt{b_2}\tilde{s} + \frac{ic_2}{2\sqrt{b_2}}\right)\right\},$$

and, since  $\tilde{k}_3(\tilde{s})$  must tend to the limiting value  $\tilde{k}_3^{\text{helix}}(\hat{h})$  as  $|\tilde{s}| \rightarrow \infty$ , we obtain

$$(4.18) \quad a_2 = -\frac{4\sqrt{b_2}\tilde{k}_3^{\text{helix}}(\hat{h})}{3\sqrt{\pi} \exp(-c_2^2/4b_2)},$$



which reduces the number of free parameters (degrees of freedom) in Eqns. 4.15, 4.16 and 4.17 to five  $(a_1, b_1, c_1, b_2, c_2)$ .

The Rayleigh-Ritz approximation is then obtained by substituting these trial functions into Eqn. 4.10, integrating with respect to  $\tilde{s}$ , and then minimizing the total energy  $\tilde{\Pi}$  with respect to the free parameters. We used the MatLab ‘fminsearch’ package which is based on the Nelder-Mead simplex direct-search algorithm. If the variation of the shape of the perversion is tracked as the tensile force,  $\tilde{P}$ , or the end-to-end length,  $h/L$ , is reduced, it is efficient to use the values of the parameters at the previous step as an initial guess for the search algorithm. Computationally, the Rayleigh-Ritz algorithm is about 100 times faster than the direct finite-element solution.

Figure 4.7 compares the Rayleigh-Ritz approximation (solid lines) with finite-element results (points) for  $h/L = 0.88$  and  $0.78$ . The agreement is clearly excellent.

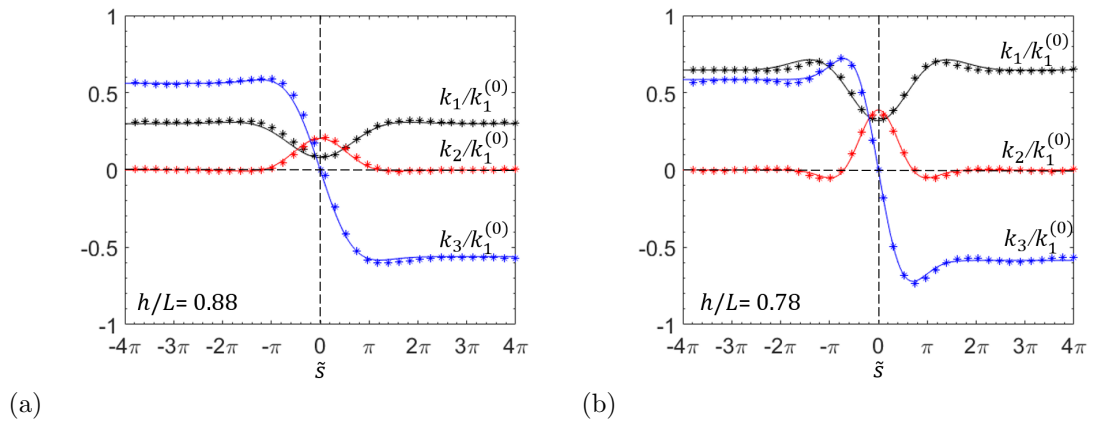


Figure 4.7: Rayleigh-Ritz approximations with five parameters for the curvature and twist functions  $\tilde{k}_1$ ,  $\tilde{k}_2$  and  $\tilde{k}_3$  (lines) compared with finite element results (points) for (a)  $h/L = 0.88$  and (b)  $h/L = 0.78$ . The numerical uncertainties in these plots are smaller than the data points.

This is confirmed by a comparison of the three-dimensional shapes for  $h/L = 0.78$

in Fig. 4.8.

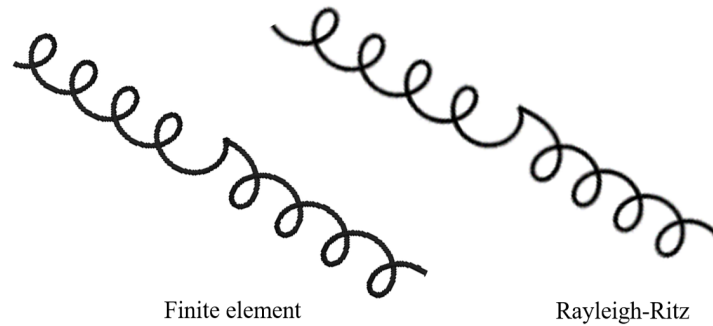


Figure 4.8: Comparison of the predicted fiber morphology from finite element and Rayleigh-Ritz calculations for  $h/L = 0.78$ .

#### Lower values of $h/L$

The Rayleigh-Ritz approximation of Eqns. 4.15, 4.16 and 4.17 provides a good fit to the finite-element results in the range  $0.65 < h/L < 1$ , but significant errors are obtained for lower values. Figure 4.9(a) compares the solutions for  $h/L = 0.32$ . It can be seen that the finite-element results exhibit several cycles of oscillation that are not captured by the Rayleigh-Ritz solution, and the asymptotic approach to the helix value is slower. This should be compared to the good agreement seen at larger values of  $h/L$  in Fig. 4.7.

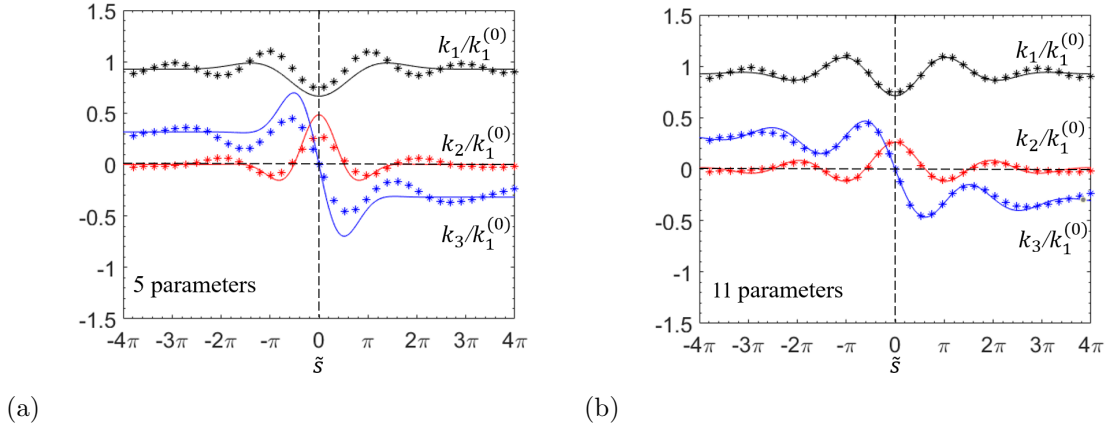


Figure 4.9: Rayleigh-Ritz solution (solid line) (a) using Eqns. 4.15, 4.16 and 4.17 with five parameters, and (b) using Eqns. 4.19, 4.20 and 4.21 with eleven parameters, compared with finite-element results (points) for  $h/L = 0.32$ . The numerical uncertainties in these plots are smaller than the data points.

An improved fit at these lower values of  $h/L$  can be obtained by using a trial function with more degrees of freedom. For example, Fig. 4.9(b) shows the fit using the expressions

$$(4.19) \quad \tilde{k}_1 = a_{11} \exp(-b_{11}\tilde{s}^2) \cos(c_{11}\tilde{s}) + a_{12} \exp(-b_{12}\tilde{s}^2) \cos(c_{12}\tilde{s}^2) + \tilde{k}_1^{\text{helix}}(\hat{h})$$

$$(4.20) \quad \tilde{k}_2 = a_{21} \exp(-b_{21}\tilde{s}^2) \cos(c_{21}\tilde{s}) + a_{22} \exp(-b_{22}\tilde{s}^2) \cos(c_{22}\tilde{s}^2)$$

$$(4.21) \quad \tilde{k}_3(\tilde{s}) = -\frac{3}{2} \int_0^{\tilde{s}} \tilde{k}_2(\tilde{s}) d\tilde{s}.$$

As with Eqns. 4.15, 4.16 and 4.17, we can eliminate one parameter by enforcing the condition that  $\tilde{k}_3(\tilde{s}) \rightarrow \tilde{k}_3^{\text{helix}}(\hat{h})$  as  $|\tilde{s}| \rightarrow \infty$ .

#### 4.4.2 Energetic considerations

One of the obvious questions that arises when considering the introduction of perversions into a coil, is whether the introduction of perversions is energetically favorable or not. In this context, it is important to appreciate that the key concept as

to whether a defect such as a perversion is introduced into a body is always the change in total energy,  $\Delta\Pi$ , rather than the change in strain energy,  $\Delta U$ . In this particular situation the number of helical coils in the fiber is generally going to be sufficiently large for them to control the relation between the end-to-end length and the force. This means that even if the remote ends of the fiber are subject to displacement-control, the local process of introducing a perversion must be considered as occurring under force-control. The energy penalty associated with the introduction of a perversion must include a potential-energy term, with the change in total energy being given by  $\Delta\Pi = \Delta U - P\Delta h$ , where  $\Delta h$  is the change in end-to-end length associated with the introduction of a perversion. To explore this expression, we evaluated the *difference* between the properties of a fiber segment containing a perversion and those of a segment of equal length but in the form of a pure helix. The asymptotic behavior exhibited by Figs. 4.7 and 4.9 shows that these differences can be evaluated by integrating over a modest region of the fiber near the perversion.

The first question we addressed was the difference in the end-to-end length of a fiber associated with the introduction of a perversion,  $\Delta h$ . This is plotted in Fig. 4.10, in which  $\Delta h$  is normalized by the intrinsic curvature, *i.e.*,  $\Delta\tilde{h} = k_1^{(0)}\Delta h$ . This calculation was performed numerically, and by using both the 5-parameter and the 11-parameter Rayleigh-Ritz approximation. As can be seen in this figure, the 5-parameter approximation provides an excellent description of the shape for  $h/L \geq 0.7$ , while the 11-parameter approximation provides an excellent description of the shape down to at least  $h/L > 0.3$ . The important thing to note from this plot is that while the introduction of a perversion causes an increase in  $h$  while  $h/L > 0.5$ , the introduction of a perversion causes the ends of the fiber to move together when  $h/L < 0.5$ .

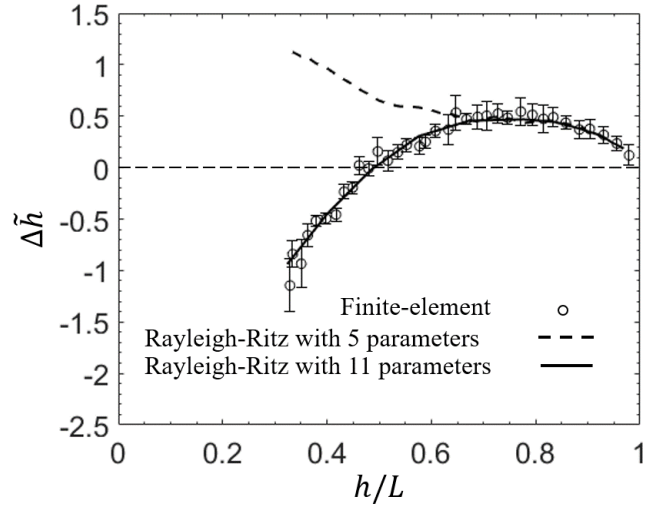


Figure 4.10: The change in normalized end-to-end distance  $\Delta\tilde{h} = k_1^{(0)}\Delta h$  between a pure helix and a coil with a perversion, showing results obtained by both finite-element calculations and the Rayleigh-Ritz method. The introduction of a perversion causes shrinkage of the fiber if  $h/L$  is less than about 0.5. It should also be noted that the 5-parameter Rayleigh-Ritz solution works very well for values of  $h/L$  greater than about 0.7.

Figure 4.11(a) shows the difference in the normalized strain energy,  $\Delta\tilde{U}$ , between a segment of fiber containing a perversion and one that does not. Again, the plot compares the numerical results with the 5- and 11-parameter approximations, showing the agreement of each being in the same range as before. It will be noted that Fig. 4.11(a) shows that the introduction of a perversion always increases the strain energy in the range  $h/L > 0.325$  over which it was feasible to do the numerical calculations, but it also indicates that the strain-energy change may be negative if  $h/L < 0.3$ . However, as discussed above, it is not the change in strain energy that controls the energetics of introducing a perversion, but the change in total energy. Figure 4.10 indicates that the potential energy change associated with the introduction of a perversion is positive when  $h/L < 0.5$ . This effect is bigger than any negative change in the strain energy, resulting in the plot of Fig. 4.11(b) for

the change in total energy. From this plot we can conclude that a perversion is energetically unfavorable for all values of  $h/L$ .

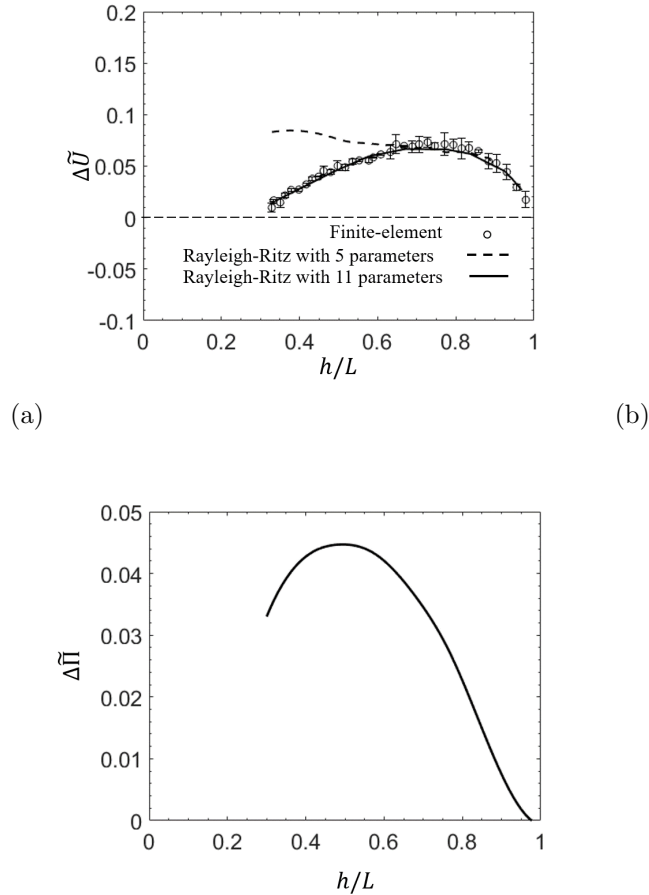


Figure 4.11: (a) The difference in strain energy between a purely helical portion of the fiber and the same length of fiber containing a single perversion. Once again, the results are well described by the 5-parameter Rayleigh-Ritz approximation of Eqns. 4.15, 4.16 and 4.17) for  $0.65 < h/L < 1$ , and by the 11-parameter approximation below this range. (b) The difference in total energy between a purely helical portion of the fiber and the same length of fiber containing a single perversion. This plot is calculated using the 11-parameter Rayleigh-Ritz solution.

#### 4.5 Persistence of perversions

Figure 4.11(b) shows that there is always a positive energy cost associated with a perversion, suggesting that only geometrically-necessary perversions should be observed. However, it can be seen from this figure that the energy cost is small when

the fiber is almost straight ( $h/L$  very close to unity). In practice, this means that there is a range of  $h/L$  where the energy costs of a perversion can be small compared to numerical or experimental noise. This can lead to the generation of additional perversions. In this section, we explore the persistence of these perversions as  $h/L$  is reduced, and the energy cost of the perversions increases.

The formation and persistence of perversions was studied using our finite-element code to generate examples of coiled fibers. Before presenting the results we first note from Fig. 4.7 (for example) that  $\tilde{k}_1$  and  $\tilde{k}_2$  experience an excursion at a perversion, but then return to the original helix value, whereas  $\tilde{k}_3$  changes sign, because a perversion separates two segments of opposite chiralities. In more complex morphologies, a perversion is therefore most easily characterized by a change in sign in the twist  $\tilde{k}_3$ , so in this section we plot this parameter as a function of distance along the fiber length.

Figure 4.12 shows a typical progression of a finite-element plot of  $\tilde{k}_3$  for a fiber of length  $L = 80\pi/k_1^{(0)}$  (*i.e.*, a fiber that would present 40 plane coils if the ends were unloaded) as  $h/L$  is reduced from 1 to 0.967. Additional perversions, beyond the single geometrically necessary one, were formed in this case, because a much longer fiber was used than for the earlier results, probably allowing some entropic effects to play a role. In the first plot for  $h/L = 0.990$ , sign changes for  $\tilde{k}_3$ , representing perversions, can be identified at the points A, B, C, D, E and F. The noise associated with the numerical algorithm can be seen in this plot, and when  $h/L \approx 1$  the variation associated with noise was similar to that associated with a perversion; this is the stage at which perversions were generated. Figures 4.12(b), (c) and (d) show the evolution of the pattern as  $h/L$  is reduced. The perversion at A moves to the end of the fiber and has disappeared at  $h/L = 0.976$ . The ‘opposite’ perversions at D and

E move closer together as the fiber is relaxed. They have annihilated each other [56] by the time  $h/L = 0.967$ . However, if  $h/L$  is reduced further, down to  $h/L = 0.40$ , no further annihilation is observed, even though the energetically optimal solution would involve only a single perversion.

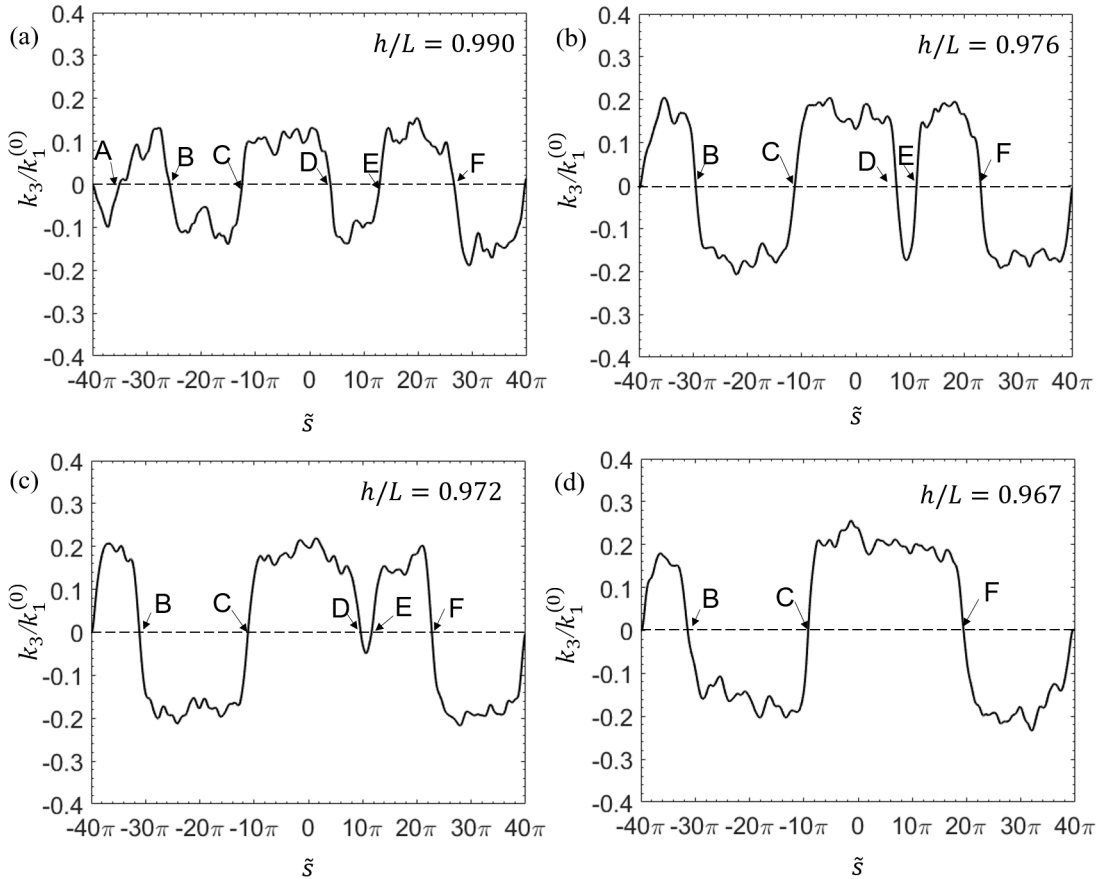


Figure 4.12: Perversions are identified by sign changes in  $\tilde{k}_3(\tilde{s})$ . Those at A D and E are annihilated as  $h/L$  is reduced.

When two perversions are widely separated (*i.e.*, beyond the range in which they interact), there is no energetic advantage in their moving together, so they are expected to persist under unloading. The process of reaching the most energetically favorable state is also impeded by the fact that the net twist, and hence the area under the curves in Fig. 4.12, must be zero. Thus, for example, B and C cannot sim-



ply move closer together in Fig. 4.12(d) without a corresponding motion of  $F$ , since otherwise this would increase the net area under the curve. Notice that when  $D$  and  $E$  annihilate each other in passing from Figs. 4.12(a) to (d), there is a corresponding motion of  $F$  to the left, to preserve the zero-net-twist condition.

### Reloading

Figure 4.13 shows the evolution of  $\tilde{k}_3(\tilde{s})$  for the same fiber as  $h/L$  is decreased from 0.972 to 0.953, and then increased again to 0.972. Notice that the perversions  $D$  and  $E$  in Figure 4.13(a) are not regenerated on reloading, and indeed the perversion at  $B$  moves towards the left end and has disappeared by the time  $h/L$  returns to 0.972 in Fig. 4.13(e). Thus, the fiber morphology exhibits significant loading-history dependence.

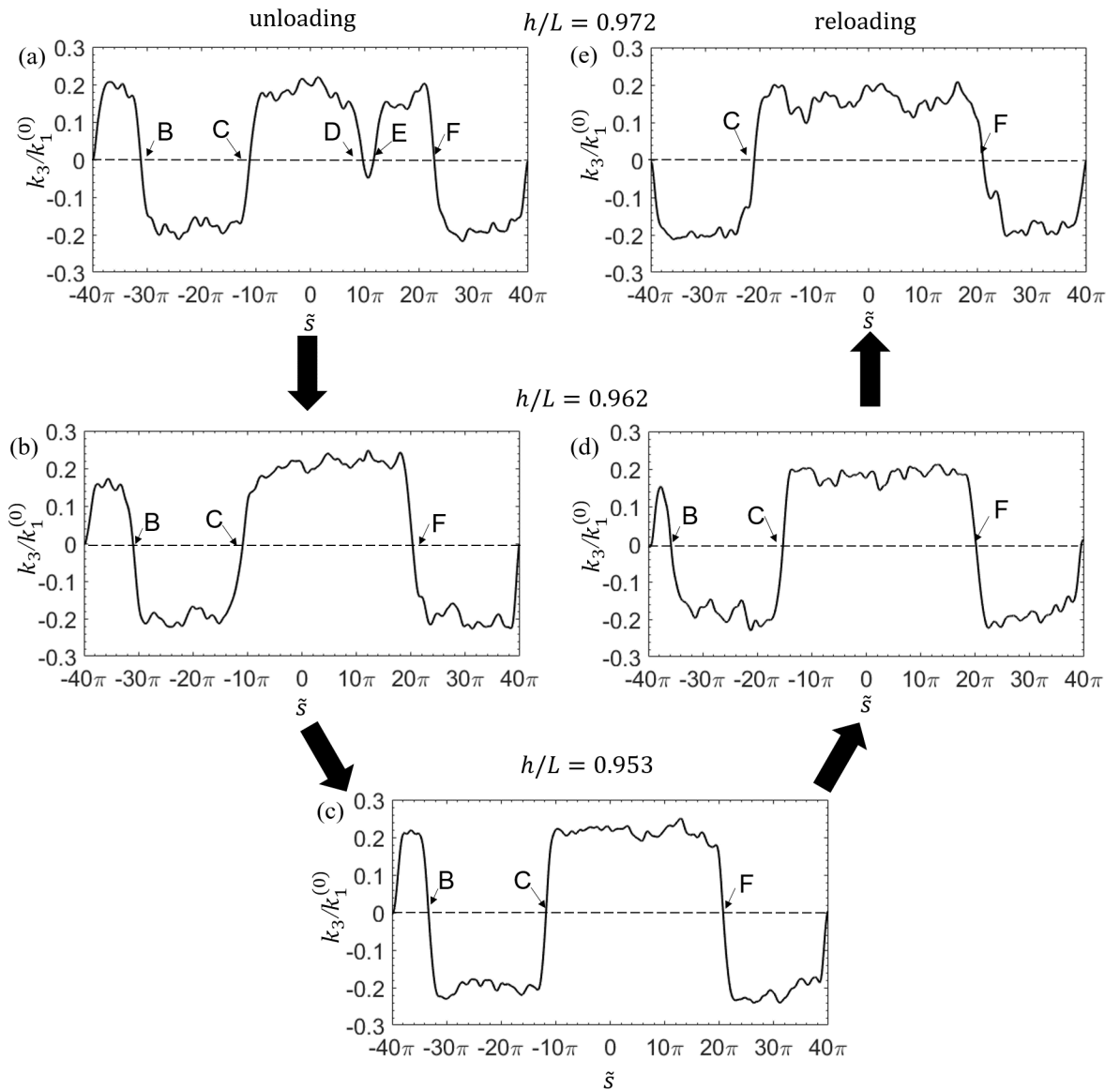


Figure 4.13: Evolution of perversions during unloading to  $h/L = 0.953$  followed by reloading to  $h/L = 0.972$ . Notice that perversions D and E are not regenerated during reloading, and B moves to the left-hand end and disappears.

### Effects of noise and quenching

The numerical results presented so far in this paper can be thought of as having been obtained under quasi-static conditions, but with enough noise to generate perversions when the fiber is almost straight and the energy barrier is low. This raises

the possibility of a potentially interesting future study of how these topological defects might be influenced by noise, and whether there are any analogies to the effects of temperature for defects in materials. Although a detailed study is beyond the scope of this present paper, we present some preliminary observations.

The first set of studies were done to look at the effect of what might be an analogy to quenching. In this context, quenching can be thought of in the following terms. When  $h/L$  is close to 1, the energetic distinction between the helical coils and perversions is small, and the probability of forming multiple perversions is high. As  $h/L$  is reduced, the energy penalty of a perversion is increased, but coordinated motion of the defects is needed for them to annihilate each other. Quenching would correspond to a relaxation rate at which the perversions formed when  $h/l \approx 1$  are effectively frozen into the fiber.

The effect of quenching was explored by varying  $d\tilde{h}/d\tilde{t}$  over about two orders of magnitude, between  $3.50 \times 10^{-7}$  and  $2.43 \times 10^{-5}$ . The corresponding results for the distributions of  $k_3$  for  $h/L = 0.5$  are shown in Fig. 4.14. It was noted that at the lower speeds corresponding to quasi-static conditions, the number of perversions formed seemed to be constant, although the location of the defects varied slightly. Unfortunately, numerical limitations associated with computational time prevented exploring whether three perversions is an asymptotic limit for this length of fiber for quasi-static conditions, or if a single perversion might ever be formed at slow-enough relaxation rates. However, it can be seen unambiguously that rapid relaxation results in many more perversions, and the number of defects increases with relaxation rate. Having shown that quenching appears to result in additional defects being frozen into the structure, the second question that arises is whether these can be annealed by mechanical oscillations, which might be an analogy of temperature. The effects

of vibration were explored by imposing an oscillating displacement on one end of the fiber after it had been relaxed to  $h/L = 0.5$  at different speeds. The results suggested that a sufficiently strong mechanical vibration could induce the perversions to move and to annihilate each other, but no obvious consistency between the magnitude of the oscillations and the resultant defect density was observed.

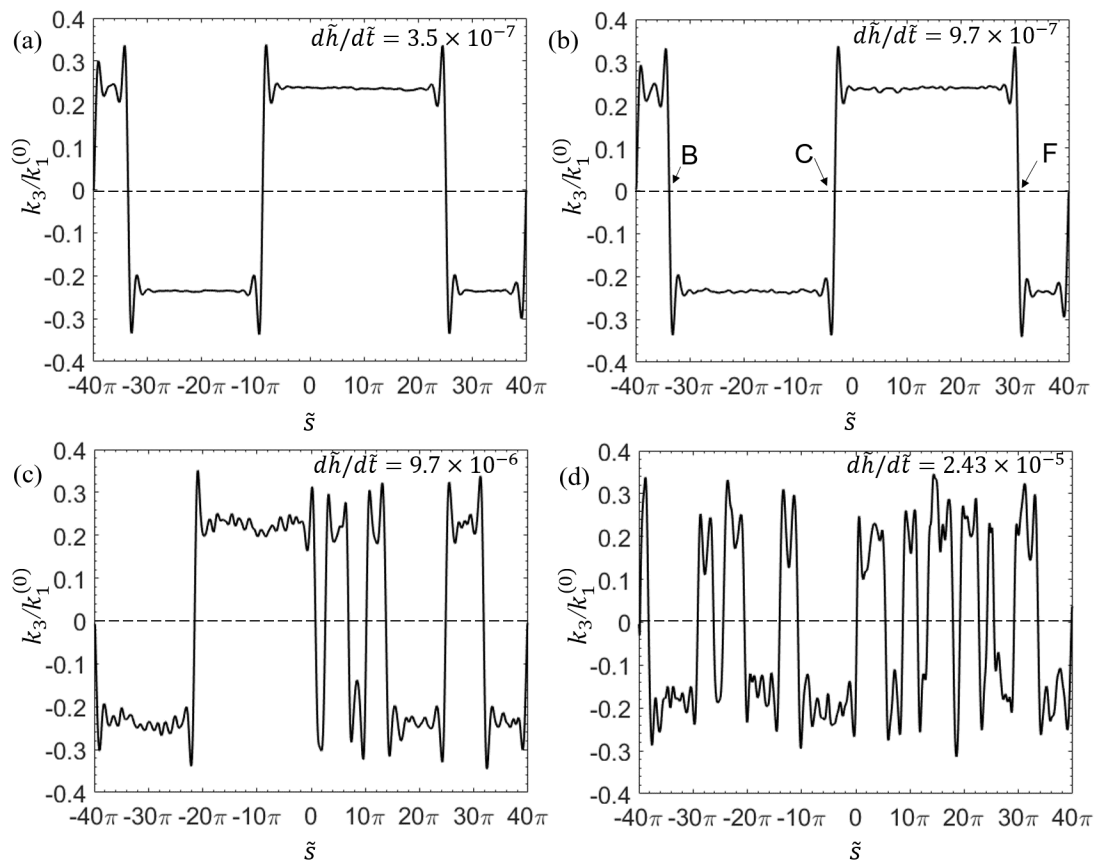


Figure 4.14: The velocity at which the ends of the fiber are relaxed influences the number of perversions that are retained at  $h/L = 0.5$ .  $d\tilde{h}/d\tilde{t} =$  (a)  $3.5 \times 10^{-7}$ , (b)  $9.7 \times 10^{-7}$ , (c)  $9.7 \times 10^{-6}$  and (d)  $2.43 \times 10^{-5}$ . Notice that (b) corresponds to the conditions under which Fig. 4.12 was obtained, and the perversions B, C and F have been retained down to  $h/L = 0.5$ .

## 4.6 Conclusions

We have investigated the generation and evolution of perversions between helical segments of a fiber with uniform intrinsic curvature when the ends are restrained against rotation. The twist function  $\tilde{k}_3(\tilde{s})$  changes sign in passing through a perversion and this provides a convenient way to identify and approximate the morphology in more complex situations.

The shape of an isolated perversion is well approximated by a simple Rayleigh-Ritz trial function, and this method also gives accurate results for the associated changes in strain energy and end-to-end length, with a considerable saving in computational time relative to a direct finite-element solution.

The lowest energy state is one in which perversions occur only when they are geometrically necessary because of the end restraint against rotation. However, the energy differential is small when the fiber is almost straight, so additional perversions may be introduced by noise in the early stages of unloading when the fiber is almost straight. If the fiber is further unloaded, perversion pairs may approach and annihilate each other, but if the perversions are too far from each other or from the fiber ends, an effective energy barrier exists so that they may persist well below the loading conditions where the energy differential is significant. A sufficiently rapid unloading resulted in a higher density of perversions being frozen into the fiber, than that obtained by slower rates of unloading, suggesting an analogy to the retention of defects in solids after thermal quenching.

The numerical results in this paper can be thought of as having been obtained under quasi-static conditions, with relatively little noise, but with enough to generate perversions when the fiber is almost straight and the energy barrier is low. This raises

the possibility of a potentially interesting future study of how the physics of these topological defects might be influenced by the level of noise in the system.

## CHAPTER V

# Fabric Design Based on Finite Element Method

### 5.1 Introduction

After we understand the behavior of individual fiber, now we can design next-generation fabric.

### 5.2 Conditional random walk to generate fibers

In order to ensure the smoothness of fibers, we add conditions on our random walk by controlling the angle in the nodal point  $i + 1$  as follows (Figure 5.1):

$$(5.1) \quad \theta_{i+1} = \alpha(\theta_i + rand)$$

where  $\alpha$  is the coefficient to adjust orientation of fiber. *Rand* is the random angle used to adjust the waviness of fiber, we use the normal distribution to generate the random numbers.

From this algorithm, it is obvious that the variation along  $x$  and  $y$  will be

$$(5.2) \quad dx = L \cos(\theta) \quad dy = L \sin(\theta)$$

where  $L$  is the step length. Therefore,

$$(5.3) \quad x_{i+1} = x_i + dx \quad y_{i+1} = y_i + dy$$

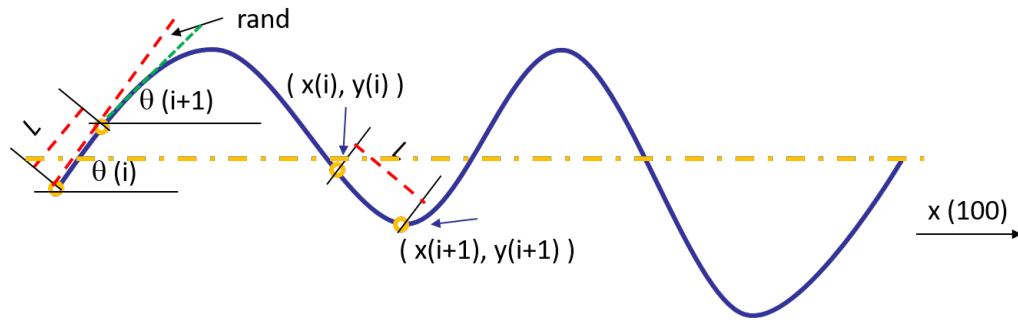


Figure 5.1: Random walk to generate natural fibers.

To generate fabric with rectangular shape, we add more constrain along the  $x$ ,  $y$  and  $z$  axis as shown in Figure 5.2. Further we need to add some constrain along the  $y$  and  $x$  axis to obtain a rectangular shape of fabric. We first generate the coordinates of nodes by random walk, and then we pick up nodes which belong to the range of  $\Delta x$  and  $\Delta y$  that we required. The fiber will be more natural and also the number of nodes & the initial point for each fiber will not be fixed.

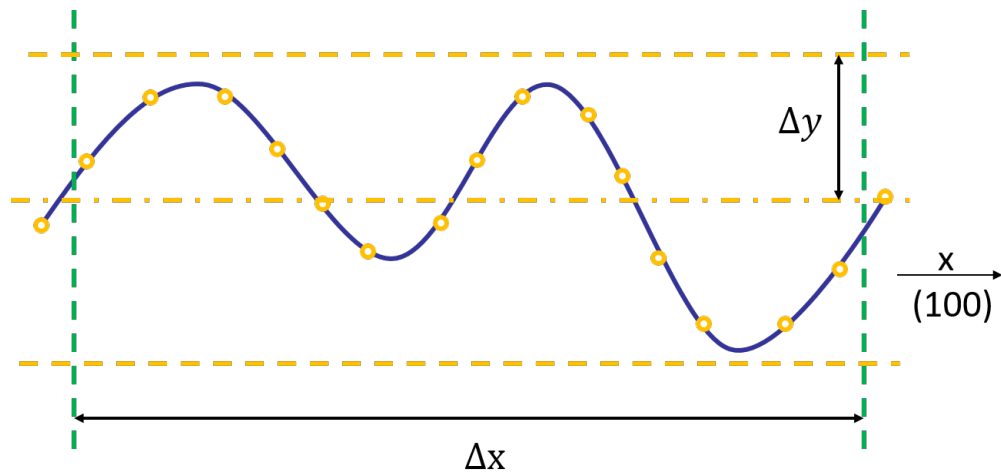


Figure 5.2: Conditional random walk to generate a piece of fabric.

Here is one example of fabric that we generated using our algorithm (Figure 5.3). To generate a piece of fabric, several parameters need to be defined. Here we consider fabric with 50 fibers. The nodal number for each fiber is in the range of 12 to 18.



And the standard deviation for rand number is  $\pi/6$  and the coefficient  $\alpha$  is 0.95.

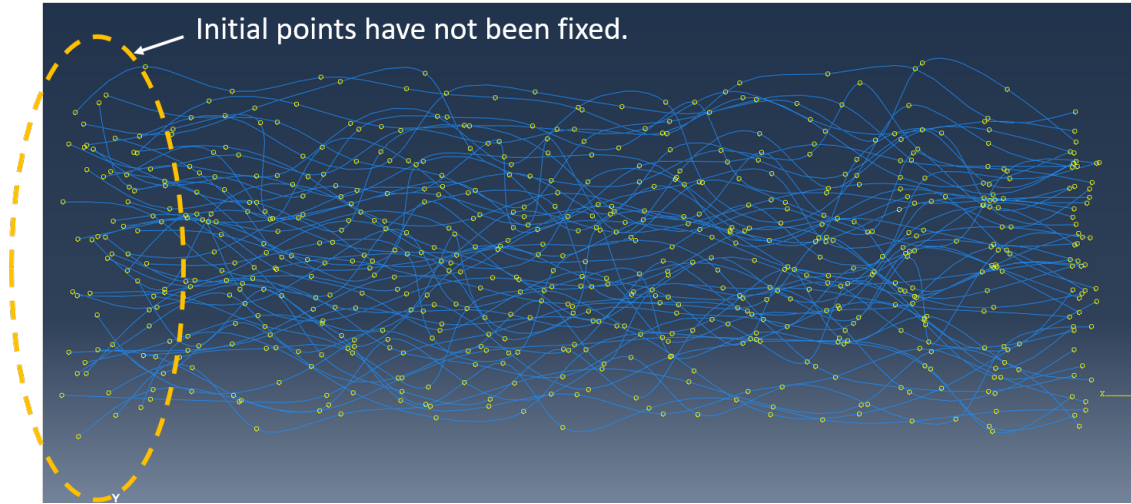


Figure 5.3: The algorithm to generate the fabric.

### 5.3 Algorithm of generating bonding site

After we can generate natural fibers, the next question is how we can generate a proper bonding site so that we can maintain the properties of fabric and also save the computational time. If we use bonding pattern from previous design in the industry, the data are obtained from *P&G* and the SEM images (Figure 3.4). The shape of individual bonding site is elliptical. And if we define the first row as odd row and second row as even row, the rotation angle of first row and the second row are opposite ( $60^\circ$  or  $-60^\circ$ ). In addition, every row has certain offset compared to adjacent row.

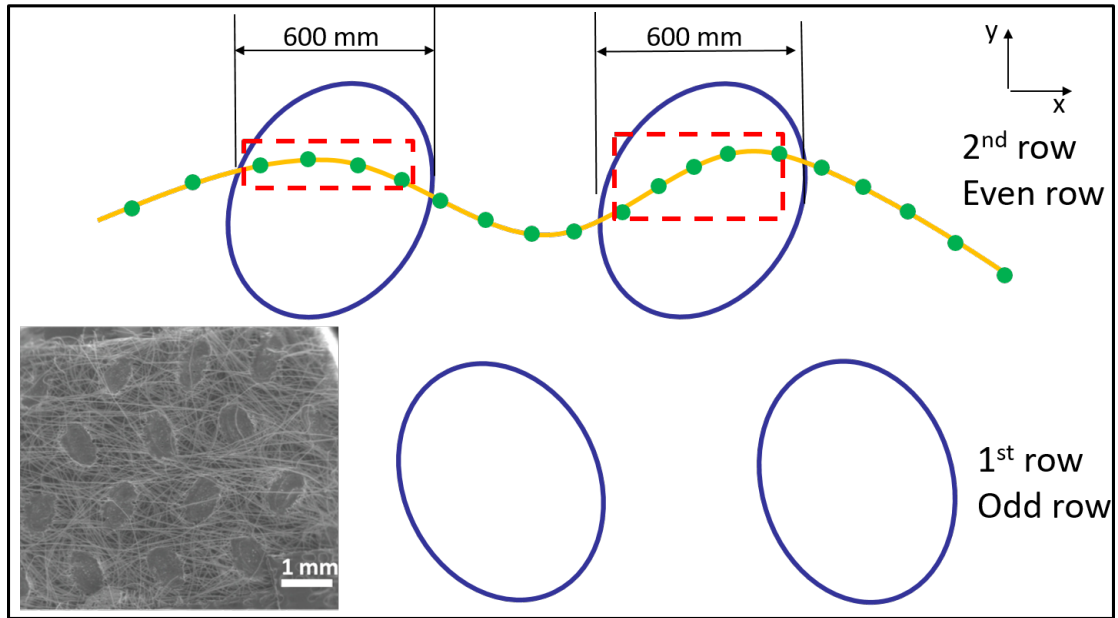


Figure 5.4: Algorithm of generating bonding site

Figure 5.5 is one example how we generate the bonding site. First we establish the bonding sites using elliptical shape as we mentioned previously and mesh the ellipse by beam element. Second we merge the nodal points of fibers by using the merge function in ABAQUS. Third we merge fibers and bonding sites by the criterion of distance between the nodes. If the distance satisfy the distance we set, then these points will be merged into one point and be treated as a bonding point. The density of the bonding site, the shape of bonding site and also size of bonding site can be easily changed based on the design.

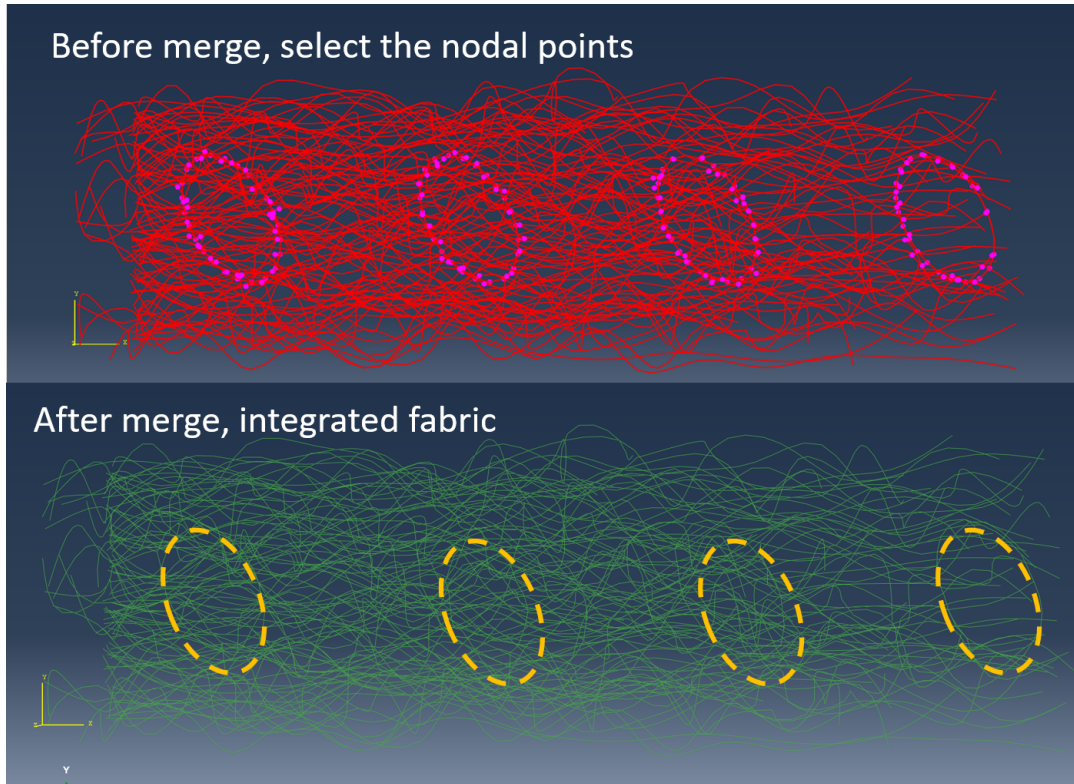


Figure 5.5: Here is one example of bonding site used in the simulation before and after merge in ABAQUS. Bonding site can be easily changed based on the design.

#### 5.4 The average material properties of fabric

The average material property of individual fiber is obtained from the experimental results (Figure 3.6). More than 100 tensile tests are conducted to obtain the average Young's modulus under the Dynamic Mechanical Analysis. The average properties of plasticity and fracture from experiment directly input into the model in the ABAQUS. The normal hard contact and tangential contact with friction coefficient of 0.1 are assumed in the model. The material properties can be changed if we consider different materials like polyethylene or the core-shell structure of polyethylene/polypropylene.

Elastic properties (we can also add viscoelasticity into the model)

Young's modulus	Poisson's ratio
1300 MPa	0.45

Plastic properties

Yield stress	Plastic strain
16 MPa	0
125 MPa	0.24

Fracture

Fracture strain	Strain rate
0.25	0.01

Density and contact

Material	Density	Normal	Tangential
Polypropylene	946 kg/m <sup>3</sup>	Hard contact	Friction coefficient: 0.1

Figure 5.6: Material properties of individual fiber are obtained from the test and then are added into the ABAQUS model. The material properties can also be changed based on the design.

#### 5.4.1 Different material properties for fiber and bonding site

Even the material of the fiber and bonding site are both polypropylene, the heat treatment can change the material properties. To include the influence of heat treatment, different sets for each individual fiber and bonding site are defined in the model. Further we can consider a stronger or a weaker bonding site compared to the properties of individual fiber.

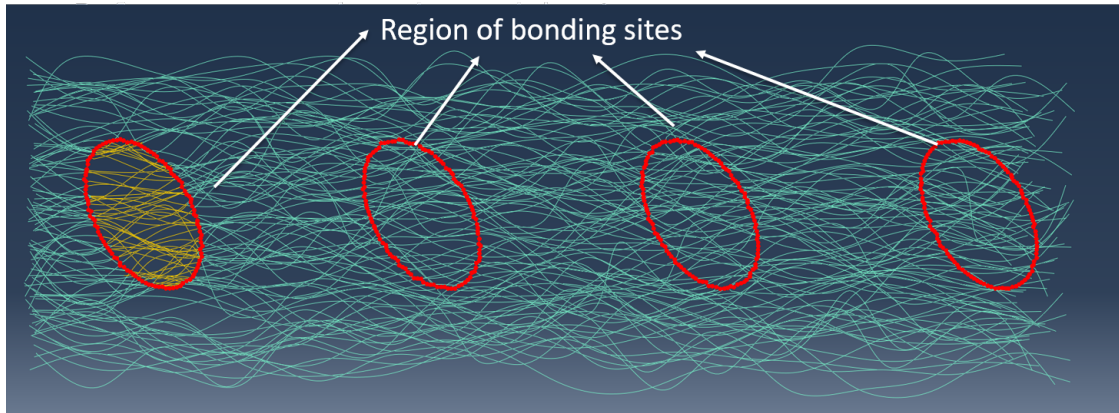


Figure 5.7: Material properties of individual fiber are obtained from the test and then are added into the ABAQUS model. The material properties can also be changed based on the design.

**5.4.2 Different material properties between individual fibers**

Similarly, the material properties of fiber can not be the same. Therefore, the variation of individual fiber are considered. Here a table of material properties of each element using normal distribution are defined by MATLAB. Only a small standard deviation are used so that each element have small variations in material properties. Based on the design, elasticity, plasticity and fracture properties can be defined by different distribution functions.

Number of rows for this table =

Element numbers

	Young's Modulus	Poisson's Ratio	Field 1
1	2000.53766713955	0.45	1E-006
2	2001.8338850146	0.45	2E-006
3	1997.741153139	0.45	3E-006
4	2000.86217332037	0.45	4E-006
5	2000.31876523986	0.45	5E-006
6	1998.69231170369	0.45	6E-006
...			

Normal distribution  
(or other functions):  
Elasticity  
Plasticity  
Fracture

Figure 5.8: Normal distribution of material properties of individual fiber.

After the material properties are defined, the names of fields are defined in both MATLAB and FORTRAN code. The fields in ABAQUS are assigned by FORTRAN code 'VUSDFLD' so that each element can have its own material properties. The material properties can be changed based on the distribution functions.

1. Define **consistent filed name** in both MATLAB and FORTRAN file;

2. Fields in ABAQUS are assigned by 'VUSDFLD' so that each element can have its own material properties.

3. Our fabric could have certain material properties distribution **based on the function we defined.**

	Young's Modulus	Poisson's Ratio	Field 1
1	2000.53766713955	0.45	1E-006
2	2001.8338850146	0.45	2E-006
3	1997.741153139	0.45	3E-006
4	2000.86217332037	0.45	4E-006
5	2000.31876523986	0.45	5E-006
6	1998.69231170369	0.45	6E-006

Figure 5.9: The fields in ABAQUS are assigned by FORTRAN code 'VUSDFLD' so that each element can have its own material properties. The material properties can be changed based on the distribution functions.

### 5.4.3 Abrasion models considering different abrasants

As mentioned in the experiments, different abrasants will lead to different morphology. For example, fabric rubbing against toothbrush will lead to the formation of fuzziness and pilling, while fabric rubbing against silicon carbide only cause the damage of individual fiber. We also consider different abrasants in the simulation.

The first model we proposed is fabric rub against toothbrush which is consistent with one of our experiments (Figure 5.10 ). The up and bottom board are defined with the properties of steel or rigid body. The up and bottom board and both ends of each fibers are fixed. The toothbrush are in the middle to remove the edge effect



and back and forth movement is applied for the abrasion simulation.

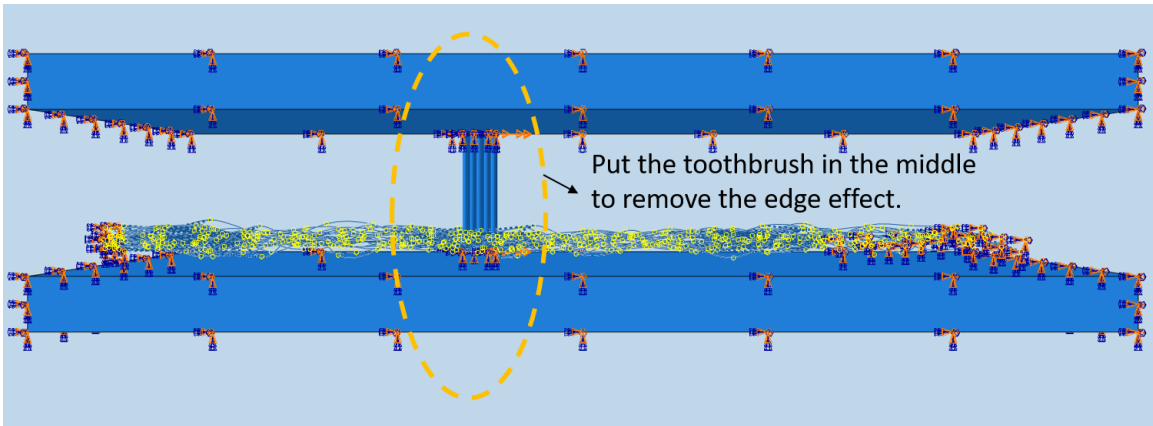


Figure 5.10: Abrasion model with abradant of toothbrush.

To mimic the properties of skin for the application of baby's diaper, Figure 5.11 shows the abrasion model with abradant of silicon rubber. This model is also consistent with the Martindale test, which is a traditional test method used in the industry. The up and bottom board with the properties of rigid body are defined with the properties of steel or rigid body. A piece of silicon rubber are put on the top of fabric and apply back and forth movement with a constant pressure on the top of fabric. We can control the amount of pressure (0.025, 0.05, 0.1 psi) in the model.

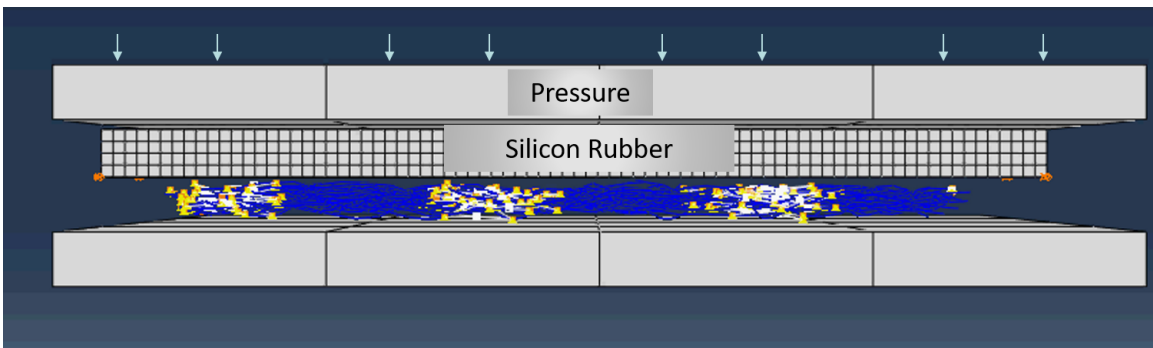


Figure 5.11: Abrasion model with abradant of silicon rubber.

## 5.5 Quantification method for degree of fuzziness and degree of damage

Since we observed both fuzziness and pillings during the experiment, both degree of fuzziness and damage are considered in the simulation.

### 5.5.1 Degree of fuzziness

The first quantification parameter we defined is the degree of fuzziness. One of the phenomenon we expected from both experiment and simulation is the formation of fuzziness. Figure 5.12 demonstrates that the morphology of fabric after abrasion from our simulation are similar to experimental results, where obvious fuzziness is observed on the surface of fabric.

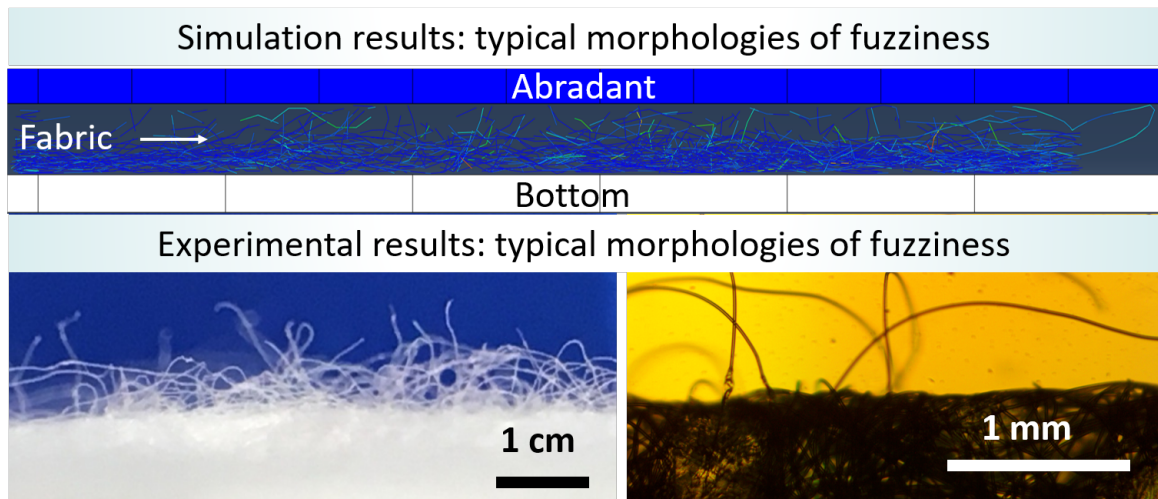


Figure 5.12: The morphology of fabric after abrasion from our simulation are similar to experimental results, where obvious fuzziness is observed on the surface of fabric.

This inspired us to draw the distribution of height of individual fibers before and after the abrasion. Figure 5.13 shows the height of fiber which is the  $z$  coordinate before abrasion (black line) approximately obeys the normal distributions. After abrasion, the heights of  $z$  coordinate increase, which are shown in the orange region. Therefore, we can use  $\Delta z$  to represent the degree of fuzziness.



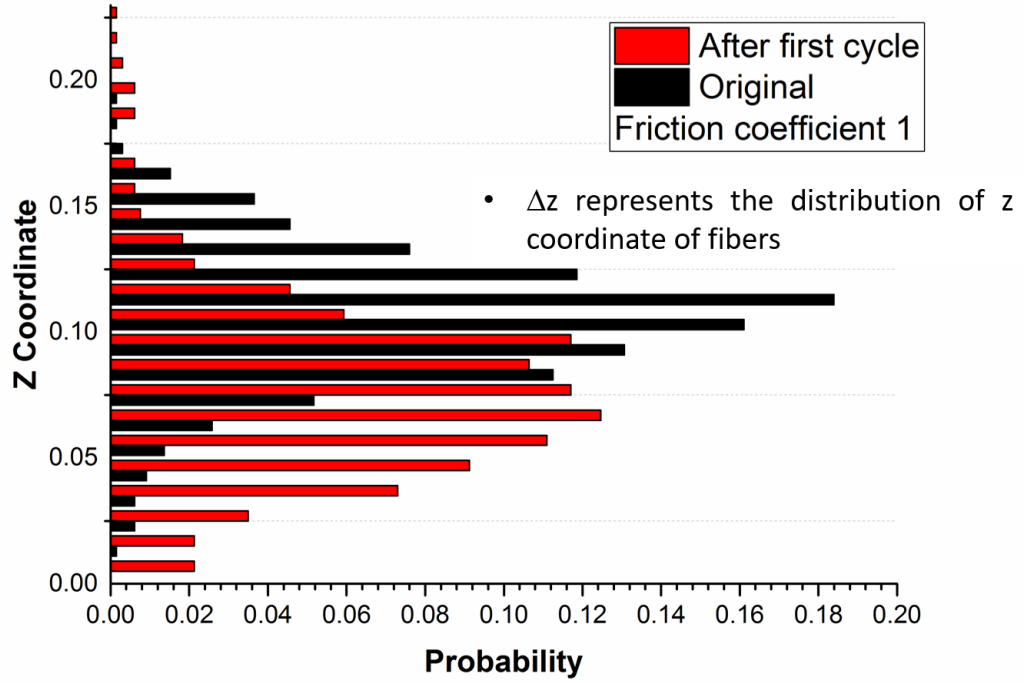


Figure 5.13: Degree of fuzziness using distribution of fiber height after abrasion.

### 5.5.2 Degree of damage

After we establish our models, a parameter to quantify degree of damage are proposed. Since we use the ductile metal model to define the material properties of our fibers, we can use the parameter  $D$ , Which demonstrates the damage of individual element in the finite-element model. When  $D$  is large than 0, it means the damage start to initiate for this element. And when  $D$  equals 1, it means the maximum degradation and element removal. To evaluate the degree of damage, we define  $D_a$  as follow:

$$(5.4) \quad D_a = \frac{\sum D(N)}{N}$$

where  $D(N)$  is the degree of damage for each element, and  $N$  is the number of elements in the model. For example if all the elements have been damaged then  $D$  will be 1 which means 100% damage. While we obtain a number from 0 to 1 to

represent the percentage of damage of fabric.

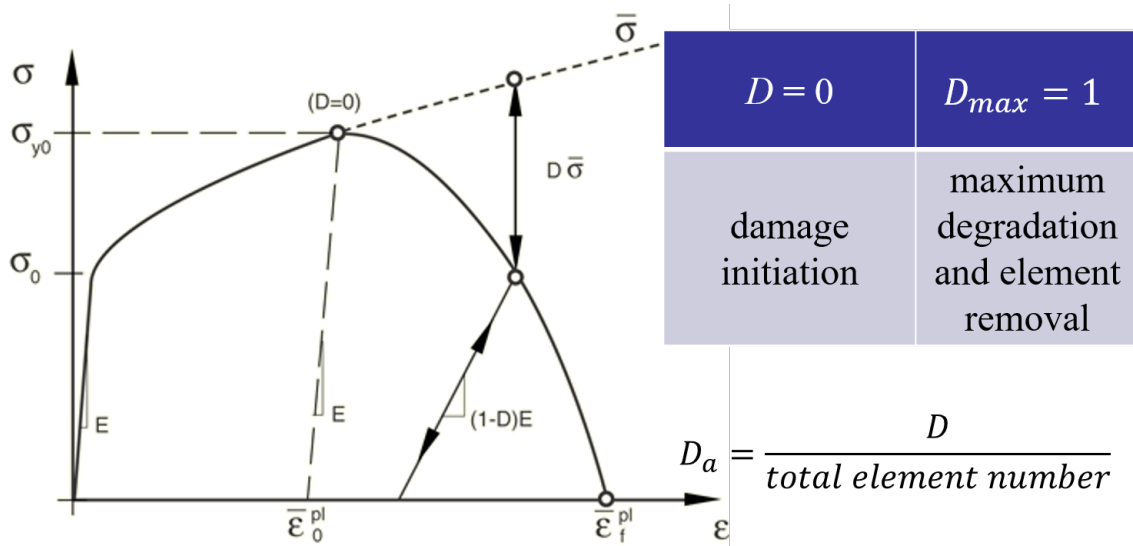


Figure 5.14: Degree of damage using the average damage of all elements.

## 5.6 Design of simulations

To design next-generation fabric, lot of parameters can be considered in the model. Based on the fiber level, fiber diameter, friction coefficient, curl ratio, orientation and properties can be considered. While based on the fabric level, the influence of bond spacing, bond size, bond orientation and also properties can be investigated. And a set of optimization parameters can be provided to the lab for the design and manufacturing of fabric.

- Fiber
  - Fiber diameter; (20  $\mu\text{m}$ , 200  $\mu\text{m}$  ...)
  - Fiber friction coefficient; (0, 0.1, 0.3...)
  - Fiber curl ratio;
  - Fiber orientation;
  - Fiber properties;
  
- Fabric
  - Bond spacing; (1.2 mm, 2.4 mm ...)
  - Bond size;
  - Bond orientation.
  - Bond properties;

Figure 5.15: Design of simulation and parameter optimization using abrasion model.

## 5.7 Conclusion

Conditional random walk are considered to generate the individual fibers. Different parameters can vary to control the material properties of fibers. And merge function are used to generate the bonding site. Based on the needs, different fabric can be designed in the model. Different material properties are considered between bonding site/individual fibers and also between fiber/fiber. Different abrasion models are proposed with two quantification parameters in the ABAQUS, the optimized parameters can be provided based on the design of simulations.

## CHAPTER VI

### Conclusion and Preliminary Results for Future Work

#### 6.1 Conclusion

Our main goals have been accomplished during five-year troubleshooting process. To solve certain problems, first we ask why it happened and which parameters control this events. And then we discover the dominant factors and the way to quantify those factors. Last but most importantly, we further investigated what kind of actions or design we will use to minimize the damage. Here I want to mention some excited moments and results during my research.

In chapter 2, two *in-situ* experimental set-up have been designed and performed in nonwoven fabric to study the evolution of abrasion process during usage. Using the *in-situ*, we found different damage morphology based on our systematical study. The formation of fuzziness and pilling appears in fiber-based abradant while damage in individual fibers are shown in non-fiber based abradant. The interconnection between macro and micro mechanisms are investigated and the dominant fiber-level mechanisms for the formation of fuzziness and pilling are discovered during the experiment. We found the stage of precursors before the formation of pillings which will have more discussion in chapter 4 and also future work. Two types of pillings are discovered after the formation of pills, which obviously benefit from the *in-situ* ex-

perimental set-up. To make the *in-situ* set-up work, we spend a lot of time to discuss and design. One of experience I have is to try and do not afraid of failure even you do not have experience. At certain stage, you should push yourself to manufacturing the set-up instead of making it perfect since it will not be perfect. I am glad that I had the experience to design the set-up even it is difficult at the beginning (I tried strain gauge and see the difference between cheap and expensive motors) which also make my work and Ph.D. innovative and unique.

In chapter 3, an objective measure of fabric abrasion based on the wavelet analysis has been developed with minimum human interpretation. A quantification parameter is defined based on the coefficient of wavelet analysis at specific levels. The factors that might influence the quantification parameters are discussed including the type of wavelets, the rotation of images. Both hardware and software are established so that the method can be used in the company. Because of previous experience, I had the confidence to establish the set-up and also I am not afraid of learning something that is new. I would say the excited moment is not I saw it works but I realized I can learn the techniques that other people developed quickly and use them into my research.

In chapter 4, the shape of an isolated perversion is well approximated by a simple Rayleigh-Ritz trial function, and this method also gives accurate results for the associated changes in strain energy and end-to-end length, with a considerable saving in computational time. Fiber perversions are energetically unfavorable except when geometrically necessary. The energy differential is small when the fiber is almost straight, so additional perversions may be introduced by noise. If the fiber is now unloaded, perversion pairs may approach and annihilate each other, but perversions can persist in ranges where the energy cost is significant. I will also extend this work

to fiber with intrinsic twist and maybe the combination of twist and curvature in the future work.

In chapter 5, conditional random walk and merge function are used to generate fabric, and then different material properties for bonding site and individual fibers are established, and two different models are proposed with two quantification parameters in the ABAQUS. Using the models we established, we can calculate a set of optimization parameters for the next-generation fabric. And we can also run the analysis to see which parameters influence the abrasion properties most.

## **6.2 Limitation**

While the work here represents a significant advance in the understanding of nonwoven fabric in the context of both experiments and simulations, there are some limitations that should be considered.

In the experimental part, our materials are limited in polypropylene and polyethylene, but other materials can be considered and might lead to a little bit different behaviors. Maybe different precursors will be observed when different materials are used in the fabric.

In the image-processing part, we only considered fabric that are used in the industry. All the samples need to be taken images and input into our software manually. The automatic software will be more helpful. In the near future, people may use machine learning technique to extend the database and predict the degree of damage based on the database we established now.

In the simulation part, although viscoelastic properties are measured by Dynamic Mechanical Analysis, we did not put them into the model. We only considered elasticity for simplicity.

### 6.3 Future work

There are a lot of work can be done in the future.

For the experimental part, one of things can be done is to establish a small database using the *in-situ* set-up so that people can use this database to choose the materials based on their need. Here we only considered the mechanical properties, however, in reality, people care the softness, smoothness and also some other surface properties of fabric. Study the interaction between different properties and how to optimize them together is a good research topic to follow up.

For the image processing part, since the current method still needs to take images as inputs for our software, in the future, we might be able to take advantage of machine learning or deep learning and build algorithms based on sample data or training data so that we can predict or evaluate the comprehensive performance, such as the abrasion, smoothness of a fabric. Further we might be able to establish a database, so that people can search for the right fabric based on their demands.

For the simulation part, we can extend our fiber-level model into a fabric-level model. We can design the fabric based on the parameter optimization. After we get a set of optimized parameters, we can further analyze the influence of different parameters on the performance of fabric. Therefore, only important parameters will be considered so that computational time can be saved in the simulation. However, if we need to design the fabric in a larger parameter space, another direction extended from current model is to consider the supervised machine learning. As you can see, if we extend the parameter space, the simulation process will be time-consuming and machine learning will be a good way to fulfill such study. Based on the training, supervised learning algorithms learn a function that can be used to predict the output

(the performance of fabric) associated with new inputs.

However, it is actually pretty exciting in chapter 4 that we can use mathematical model to study the individual fiber with intrinsic curvature and also semi-analytical solutions for perversions. In the future we can focus on the intrinsic curvature to get a semi-analytical solution for the interaction of perversions. Or we can focus on the fiber with intrinsic twist and even mixture of curvature and twist.

Here is some preliminary results for fiber with intrinsic twist.

## 6.4 Fiber-level model for intrinsic twist

### 6.4.1 Dynamic or static Kirchhoff equation

We can use both dynamic and static approach to proof that helical solution is not stable. Based on the Kirchhoff theory, a perturbation scheme can be established [33]. The basis itself can be expanded in powers of  $\epsilon$  and demand that to first order so that the new basis (perturbed basis) remains an orthonormal basis. All the other parameters can be defined in the both unperturbed basis and perturbed basis.

$$(6.1) \quad \mathbf{d}_i = \mathbf{d}_i^{(0)} + \epsilon \mathbf{d}_i^{(1)} + O(\epsilon^2), \quad i = 1, 2, 3$$

The correction  $\mathbf{d}_i^{(1)}$  are defined in the unperturbed basis.

$$(6.2) \quad \mathbf{d}_i^{(1)} = \sum_{j=1}^3 A_{ij} \mathbf{d}_j^{(0)}, \quad i = 1, 2, 3.$$

where  $A$  is an anti-symmetric matrix (The detailed proof are in section 1.2.3) and  $A$  only have 3 degree of freedom, we can define a vector  $\boldsymbol{\alpha}$  and use the cross product to define  $\mathbf{d}_i^{(1)}$  as follow. Therefore, the director basis takes the form

$$(6.3) \quad \mathbf{d}_i = \mathbf{d}_i^{(0)} + \epsilon (\boldsymbol{\alpha} \times \mathbf{d}_i^{(0)}) + O(\epsilon^2), \quad i = 1, 2, 3$$

where

$$(6.4) \quad \mathbf{d}_i^{(1)} = \boldsymbol{\alpha} \times \mathbf{d}_i^{(0)}$$



where

$$(6.5) \quad \boldsymbol{\alpha} = \alpha_1 \mathbf{d}_1^{(0)} + \alpha_2 \mathbf{d}_2^{(0)} + \alpha_3 \mathbf{d}_3^{(0)}$$

Therefore, we can transfer the perturbed basis into unperturbed basis (original basis) using  $\boldsymbol{\alpha}$  and  $\boldsymbol{\alpha}$  is defined in the unperturbed basis.

A quantity  $\mathbf{V}$  can be expressed in either unperturbed basis or perturbed basis. We found the relationship between the perturbed and unperturbed basis for a quantity.

$$(6.6) \quad \mathbf{V}^{(1)} = (\boldsymbol{\alpha} \times v_i^{(0)} \mathbf{d}_i^{(0)}) + v_i^{(1)} \mathbf{d}_i^{(0)}$$

where  $\mathbf{V}^{(1)} = V_i^{(1)} \mathbf{d}_i^{(0)}$  is a correction vector of parameter  $\mathbf{V} = \mathbf{V}^{(0)} + \epsilon \mathbf{V}^{(1)}$  in the unperturbed basis, and vector  $\boldsymbol{\alpha}$  is defined in the previous section,  $v_i = v_i^{(0)} + \epsilon v_i^{(1)}$  is a scalar that defined in the perturbed basis.

$$(6.7) \quad V_i^{(1)} \mathbf{d}_i^{(0)} = (\boldsymbol{\alpha} \times v_i^{(0)} \mathbf{d}_i^{(0)}) + v_i^{(1)} \mathbf{d}_i^{(0)}$$

Now all the parameters are in the unperturbed basis, but note that  $V_i^{(1)}$  and  $v_i^{(1)}$  are different.

For example  $k$ :

$$(6.8) \quad \mathbf{K}^{(1)} = \boldsymbol{\alpha}' + \boldsymbol{\alpha} \times \mathbf{k}^{(0)}$$

We also have this relationship

$$(6.9) \quad \mathbf{K}^{(1)} = (\boldsymbol{\alpha} \times k_i^{(0)} \mathbf{d}_i^{(0)}) + k_i^{(1)} \mathbf{d}_i^{(0)}$$

Therefore

$$(6.10) \quad k_i^{(1)} \mathbf{d}_i^{(0)} = \boldsymbol{\alpha}'$$

### 6.4.2 Newton's equation

$$(6.11) \quad \mathbf{F}'' = \ddot{\mathbf{d}}_3$$

1. Linear expansion:

$$(6.12) \quad \mathbf{F} = \mathbf{F}^{(0)} + \epsilon \mathbf{F}^{(1)} \quad \mathbf{d}_3 = \mathbf{d}_3^{(0)} + \epsilon \mathbf{d}_3^{(1)}$$

From equation 6.11 and 6.12, we get

$$(6.13) \quad (\mathbf{F}^{(1)})'' = \ddot{\mathbf{d}}_3^{(1)}$$

$$(6.14) \quad \ddot{\mathbf{d}}_3^{(1)} = \ddot{\alpha}_2 \mathbf{d}_1^{(0)} - \ddot{\alpha}_1 \mathbf{d}_2^{(0)}$$

$f^{(0)}$  and  $f^{(1)}$  is defined in the current basis, and is scalar.

3 PDEs in each direction about  $\mathbf{F}$  are obtained.

$$(6.15) \quad (\ddot{\alpha}_2) \mathbf{d}_1^{(0)} =$$

$$(f_1^{(1)})'' + (\alpha_2'' f_3^{(0)} + \alpha_2' f_3^{(0)'} + \alpha_2' f_3^{(0)'} + \alpha_2 f_3^{(0)''} - \alpha_3'' f_2^{(0)} - \alpha_3' f_2^{(0)'} - \alpha_3' f_2^{(0)'} - \alpha_3 f_2^{(0)''}) \mathbf{d}_1^{(0)}$$

$$+ 2(f_2^{(1)'} + (\alpha_3' f_1^{(0)} + \alpha_3 f_1^{(0)'} - \alpha_1' f_3^{(0)} - \alpha_1 f_3^{(0)'}) (-k_3^{(0)} \mathbf{d}_1^{(0)})$$

$$+ 2(f_3^{(1)'} + (\alpha_1' f_2^{(0)} + \alpha_1 f_2^{(0)'} - \alpha_2' f_1^{(0)} - \alpha_2 f_1^{(0)'}) (k_2^{(0)} \mathbf{d}_1^{(0)})$$

$$+ (f_1^{(1)} + (\alpha_2 f_3^{(0)} - \alpha_3 f_2^{(0)})) ([-(k_3^{(0)})^2 - (k_2^{(0)})^2] \mathbf{d}_1^{(0)})$$

$$+ (f_2^{(1)} + (\alpha_3 f_1^{(0)} - \alpha_1 f_3^{(0)})) (k_1^{(0)} k_2^{(0)} \mathbf{d}_1^{(0)})$$

$$+ (f_3^{(1)} + (\alpha_1 f_2^{(0)} - \alpha_2 f_1^{(0)})) (k_1^{(0)} k_3^{(0)} \mathbf{d}_1^{(0)})$$

$$\begin{aligned}
(6.16) \quad & -(\ddot{\alpha}_1)\mathbf{d}_2^{(0)} = \\
& +(f_2^{(1)''} + (\alpha_3''f_1^{(0)} + \alpha_3'f_1^{(0)'} + \alpha_3'f_1^{(0)'} + \alpha_3f_1^{(0)''} - \alpha_1''f_3^{(0)} - \alpha_1'f_3^{(0)'} - \alpha_1'f_3^{(0)'} - \alpha_1f_3^{(0)''}))\mathbf{d}_2^{(0)} \\
& \quad + 2(f_1^{(1)'} + (\alpha_2'f_3^{(0)} + \alpha_2f_3^{(0)'} - \alpha_3'f_2^{(0)} - \alpha_3f_2^{(0)'})))(k_3^{(0)}\mathbf{d}_2^{(0)}) \\
& \quad + 2(f_3^{(1)'} + (\alpha_1'f_2^{(0)} + \alpha_1f_2^{(0)'} - \alpha_2'f_1^{(0)} - \alpha_2f_1^{(0)'})))(-k_1^{(0)}\mathbf{d}_2^{(0)}) \\
& \quad + (f_1^{(1)} + (\alpha_2f_3^{(0)} - \alpha_3f_2^{(0)}))(k_1^{(0)}k_2^{(0)}\mathbf{d}_2^{(0)}) \\
& \quad + (f_2^{(1)} + (\alpha_3f_1^{(0)} - \alpha_1f_3^{(0)}))([-(k_1^{(0)})^2 - (k_3^{(0)})^2]\mathbf{d}_2^{(0)}) \\
& \quad + (f_3^{(1)} + (\alpha_1f_2^{(0)} - \alpha_2f_1^{(0)}))(k_2^{(0)}k_3^{(0)}\mathbf{d}_2^{(0)})
\end{aligned}$$

$$\begin{aligned}
(6.17) \quad & (0)\mathbf{d}_3^{(0)} = \\
& (f_3^{(1)''} + (\alpha_1''f_2^{(0)} + \alpha_1'f_2^{(0)'} + \alpha_1'f_2^{(0)'} + \alpha_1f_2^{(0)''} - \alpha_2''f_1^{(0)} - \alpha_2'f_1^{(0)'} - \alpha_2'f_1^{(0)'} - \alpha_2f_1^{(0)''}))\mathbf{d}_3^{(0)} \\
& \quad + 2(f_1^{(1)'} + (\alpha_2'f_3^{(0)} + \alpha_2f_3^{(0)'} - \alpha_3'f_2^{(0)} - \alpha_3f_2^{(0)'})))(-k_2^{(0)}\mathbf{d}_3^{(0)}) \\
& \quad + 2(f_2^{(1)'} + (\alpha_3'f_1^{(0)} + \alpha_3f_1^{(0)'} - \alpha_1'f_3^{(0)} - \alpha_1f_3^{(0)'})))(k_1^{(0)}\mathbf{d}_3^{(0)}) \\
& \quad + (f_1^{(1)} + (\alpha_2f_3^{(0)} - \alpha_3f_2^{(0)}))(k_1^{(0)}k_3^{(0)}\mathbf{d}_3^{(0)}) \\
& \quad + (f_2^{(1)} + (\alpha_3f_1^{(0)} - \alpha_1f_3^{(0)}))(k_2^{(0)}k_3^{(0)}\mathbf{d}_3^{(0)}) \\
& \quad + (f_3^{(1)} + (\alpha_1f_2^{(0)} - \alpha_2f_1^{(0)}))([-(k_1^{(0)})^2 - (k_2^{(0)})^2]\mathbf{d}_3^{(0)})
\end{aligned}$$

### 6.4.3 Moment equation

$$\begin{aligned}
(6.18) \quad & (\mathbf{M}^{(1)})' + \mathbf{d}_3^{(0)} \times \mathbf{F}^{(1)} + \mathbf{d}_3^{(1)} \times \mathbf{F}^{(0)} \\
& = \mathbf{d}_1^{(0)} \times \ddot{\mathbf{d}}_1^{(1)} + \mathbf{d}_1^{(1)} \times \ddot{\mathbf{d}}_1^{(0)} + \mathbf{d}_2^{(0)} \times \ddot{\mathbf{d}}_2^{(1)} + \mathbf{d}_2^{(1)} \times \ddot{\mathbf{d}}_2^{(0)}
\end{aligned}$$

3 PDEs in each direction about  $\mathbf{M}$  are obtained as follows:

(6.19)

$$\begin{aligned}
& (\alpha_1'' - \alpha_2' k_3^{(0)} + \alpha_2' \Gamma k_3^{(0)}) \mathbf{d}_1^{(0)} \\
& + (\alpha_2' + \alpha_1 k_3^{(0)} - \alpha_1 \Gamma k_3^{(0)}) (-k_3^{(0)} \mathbf{d}_1^{(0)}) \\
& + (\Gamma(\alpha_3' - \alpha_1 k_2^{(0)} + \alpha_2 k_1^{(0)}) + \alpha_1 k_2^{(0)} - \alpha_2 k_1^{(0)}) (k_2^{(0)} \mathbf{d}_1^{(0)}) \\
& - (f_2^{(1)} + (\alpha_3 f_1^{(0)} - \alpha_1 f_3^{(0)})) \mathbf{d}_1^{(0)} \\
& - \alpha_1 f_3^{(0)} \mathbf{d}_1^{(0)} \\
& = \ddot{\alpha}_1 \mathbf{d}_1^{(0)}
\end{aligned}$$

(6.20)

$$\begin{aligned}
& (\alpha_2'' + \alpha_1' k_3^{(0)} - \alpha_1' \Gamma k_3^{(0)}) \mathbf{d}_2^{(0)} \\
& + (\alpha_1' - \alpha_2 k_3^{(0)} + \alpha_2 \Gamma k_3^{(0)}) (k_3^{(0)} \mathbf{d}_2^{(0)}) \\
& + (\Gamma(\alpha_3' - \alpha_1 k_2^{(0)} + \alpha_2 k_1^{(0)}) + \alpha_1 k_2^{(0)} - \alpha_2 k_1^{(0)}) (-k_1^{(0)} \mathbf{d}_2^{(0)}) \\
& + (f_1^{(1)} + (\alpha_2 f_3^{(0)} - \alpha_3 f_2^{(0)})) \mathbf{d}_2^{(0)} \\
& - \alpha_2 f_3^{(0)} \mathbf{d}_2^{(0)} \\
& = \ddot{\alpha}_2 \mathbf{d}_2^{(0)}
\end{aligned}$$

(6.21)

$$\begin{aligned}
& (\Gamma(\alpha_3'' - \alpha_1' k_2^{(0)} + \alpha_2' k_1^{(0)}) + \alpha_1' k_2^{(0)} - \alpha_2' k_1^{(0)}) \mathbf{d}_3^{(0)} \\
& + (\alpha_1' - \alpha_2 k_3^{(0)} + \alpha_2 \Gamma k_3^{(0)}) (-k_2^{(0)} \mathbf{d}_3^{(0)}) \\
& + (\alpha_2' + \alpha_1 k_3^{(0)} - \alpha_1 \Gamma k_3^{(0)}) (k_1^{(0)} \mathbf{d}_3^{(0)}) \\
& \alpha_2 f_2^{(0)} \mathbf{d}_3^{(0)} + \alpha_1 f_1^{(0)} \mathbf{d}_3^{(0)} \\
& = 2\ddot{\alpha}_3 \mathbf{d}_3^{(0)}
\end{aligned}$$

If we use linear perturbation, we assume that:

$$(6.22) \quad L(\mathbf{k}^{(0)}, \mathbf{f}^{(0)})\boldsymbol{\mu} = 0$$

$$(6.23) \quad \boldsymbol{\mu} = (\alpha_1, \alpha_2, \alpha_3, f_1^{(1)}, f_2^{(1)}, f_3^{(1)})$$

$$(6.24) \quad (k_1^{(0)}, k_2^{(0)}, k_3^{(0)}, f_1^{(0)}, f_2^{(0)}, f_3^{(0)}) = (0, k, \tau, 0, (\Gamma - 1)k\tau, (\Gamma - 1)\tau^2)$$

Assume the solution is

$$(6.25) \quad \boldsymbol{\mu} = \boldsymbol{\xi}_n \exp(\sigma_n t + i n s)$$

$$\begin{pmatrix} L_{11} & L_{12} & L_{13} & L_{14} & L_{15} & L_{16} \\ L_{21} & L_{22} & L_{23} & L_{24} & L_{25} & L_{26} \\ L_{31} & L_{32} & L_{33} & L_{34} & L_{35} & L_{36} \\ L_{41} & L_{42} & L_{43} & L_{44} & L_{45} & L_{46} \\ L_{51} & L_{52} & L_{53} & L_{54} & L_{55} & L_{56} \\ L_{61} & L_{62} & L_{63} & L_{64} & L_{65} & L_{66} \end{pmatrix}$$

(6.26)

$$L_{11} = 2in(\Gamma - 1)\tau(k^2 + \tau^2); \quad L_{12} = -\sigma_n^2 - \tau^2(\Gamma - 1)(n^2 + \tau^2 + k^2);$$

$$L_{13} = k\tau(\Gamma - 1)(\tau^2 + k^2 + n^2); \quad L_{14} = -(\tau^2 + k^2 + n^2);$$

$$L_{15} = -2in\tau; \quad L_{16} = 2ink;$$

(6.27)

$$\begin{aligned}
L_{21} &= \tau^2(\Gamma - 1)(n^2 + \tau^2 + k^2) + \sigma_n^2; & L_{22} &= 2in\tau^3(\Gamma - 1); \\
L_{23} &= -2ink\tau^2(\Gamma - 1); & L_{24} &= 2in\tau; \\
L_{25} &= -n^2 - \tau^2; & L_{26} &= k\tau;
\end{aligned}$$

(6.28)

$$\begin{aligned}
L_{31} &= -k\tau(\Gamma - 1)(k^2 + \tau^2 + n^2) & L_{32} &= -2ink\tau^2(\Gamma - 1); \\
L_{33} &= 2ink^2\tau(\Gamma - 1); & L_{34} &= -2ink; \\
L_{35} &= k\tau; & L_{36} &= -k^2 - n^2;
\end{aligned}$$

(6.29)

$$\begin{aligned}
L_{41} &= -n^2 - \sigma_n^2 + (1 - \Gamma)k^2 + (\Gamma - 1)\tau^2; & L_{42} &= (\Gamma - 2)in\tau; \\
L_{43} &= \Gamma ink; & L_{44} &= 0; \\
L_{45} &= -1; & L_{46} &= 0;
\end{aligned}$$

(6.30)

$$\begin{aligned}
L_{51} &= (2 - \Gamma)in\tau; & L_{52} &= -n^2 - \sigma_n^2 + (\Gamma - 1)\tau^2; \\
L_{53} &= -(\Gamma - 1)k\tau; & L_{54} &= 1; \\
L_{55} &= 0; & L_{56} &= 0;
\end{aligned}$$

(6.31)

$$\begin{aligned}
L_{61} &= -\Gamma ink; & L_{62} &= 0 \\
L_{63} &= -\Gamma n^2 - 2\sigma_n^2; & L_{64} &= 0; \\
L_{65} &= 0; & L_{66} &= 0;
\end{aligned}$$

We found that the helical solution is not stable since we can get positive  $\sigma$  (Figure 6.1).

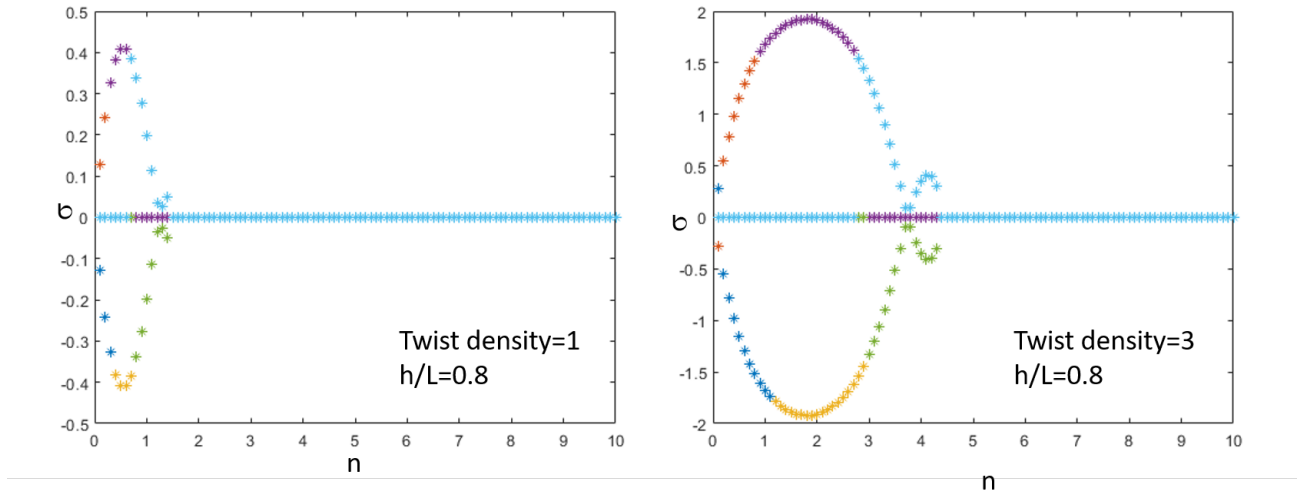


Figure 6.1: Positive  $\sigma$  are found so that the helical solution is not stable.

#### 6.4.4 Energy method

Here the idea is to consider the static Kirchhoff equation, and then perturb the solution a little bit and see whether we can get a configuration that has lower total energy. Therefore we compare the energy of pure helix with the energy after perturbation.

Since we fixed the end-to-end distance, we do not have the change of potential

energy and for pure helix, the strain energy is

$$(6.32) \quad E_{(helix)} = \frac{\tilde{k}_1^2}{2} + \frac{\tilde{k}_2^2}{2} + \frac{\tilde{k}_3^2}{3} = \frac{\tilde{k}^2}{2} + \frac{\tilde{\tau}^2}{3}$$

For the perturbed shape, the strain energy is

$$(6.33) \quad E_{(helix)} = \frac{\tilde{k}_1^2}{2} + \frac{\tilde{k}_2^2}{2} + \frac{\tilde{k}_3^2}{3} = \frac{(\epsilon \tilde{k}_1^{(1)})^2}{2} + \frac{(\tilde{k} + \epsilon \tilde{k}_2^{(1)})^2}{2} + \frac{(\tilde{\tau} + \epsilon \tilde{k}_3^{(1)})^2}{3}$$

5.

$$(6.34) \quad \mathbf{k}_1^{(1)} = (\alpha'_1 - \alpha_2 k_3^{(0)} + \alpha_3 k_2^{(0)}) \mathbf{d}_1^{(0)}$$

$$(6.35) \quad \mathbf{k}_2^{(1)} = (\alpha'_2 + \alpha_1 k_3^{(0)} - \alpha_3 k_1^{(0)}) \mathbf{d}_2^{(0)}$$

$$(6.36) \quad \mathbf{k}_3^{(1)} = (\alpha'_3 - \alpha_1 k_2^{(0)} + \alpha_2 k_1^{(0)}) \mathbf{d}_3^{(0)}$$

$$(6.37) \quad \alpha_1 = \xi_1 \exp(ins) \quad \alpha_2 = \xi_2 \exp(ins) \quad \alpha_3 = \xi_3 \exp(ins)$$

For the perturbed shape, the strain energy is

$$(6.38) \quad E_{(perturbed)} = \int \left( \frac{(\epsilon \tilde{k}_1^{(1)})^2}{2} + \frac{(\tilde{k} + \epsilon \tilde{k}_2^{(1)})^2}{2} + \frac{(\tilde{\tau} + \epsilon \tilde{k}_3^{(1)})^2}{3} \right)$$

$$(6.39) \quad E_{(perturbed)} = \int \frac{(\epsilon \exp(ins)(in\xi_1 - \xi_2\tau + \xi_3k))^2}{2} + \frac{(\tilde{k} + \epsilon \exp(ins)(in\xi_2 + \xi_1\tau))^2}{2} + \frac{(\tilde{\tau} + \epsilon \exp(ins)(in\xi_3 - \xi_1k))^2}{3}$$

We also found lower energy state which means that helical solution is not stable.

Therefore we can further use both RR and FE method to study the fiber with intrinsic twist and investigate the shape evolution of fiber.



## BIBLIOGRAPHY

- [1] I Abdullah, R S Blackburn, S J Russell, and J Taylor. Abrasion phenomena in twill tencel fabric. *Journal of applied polymer science*, 102(2):1391–1398, 2006.
- [2] W Albrecht. How can pilling be avoided in articles from polyester spun fibres either through construction or from a fibre viewpoint. *Chemiefasern*, 20(5):387–396, 1970.
- [3] W Albrecht, H Fuchs, and W Kittelmann. *Nonwoven fabrics: raw materials, manufacture, applications, characteristics, testing processes*. John Wiley & Sons, 2006.
- [4] P A Annis. Surface wear analysis of fabrics. *ASTM Standardization News*, 33(9):30, 2005.
- [5] S Armon, E Efrati, R Kupferman, and E Sharon. Geometry and mechanics in the opening of chiral seed pods. *Science*, 333(6050):1726–1730, 2011.
- [6] A Arsenlis and D M Parks. Crystallographic aspects of geometrically-necessary and statistically-stored dislocation density. *Acta Materialia*, 47(5):1597–1611, 1999.
- [7] D J Atherton. The aetiology and management of irritant diaper dermatitis. *Journal of the European Academy of Dermatology and Venereology*, 15(s1):1–4, 2001.
- [8] M E Baird, P Hatfield, and G J Morris. 12—pilling of fabrics: A study of nylon and nylon blended fabrics. *Journal of the Textile Institute Transactions*, 47(4):T181–T201, 1956.
- [9] J R Barber. *Intermediate Mechanics of Materials*, volume 175. Springer Science & Business Media, 2010.
- [10] R L Barker and R C Heniford. Factors affecting the thermal insulation and abrasion resistance of heat resistant hydro-entangled nonwoven batting materials for use in firefighter turnout suit thermal liner systems. *Journal of Engineered Fibers and Fabrics*, 6(1):1–10, 2011.
- [11] J Bijwe, J Indumathi, and A K Ghosh. On the abrasive wear behaviour of fabric-reinforced polyetherimide composites. *Wear*, 253(7-8):768–777, 2002.
- [12] J Bijwe, J Indumathi, J J Rajesh, and M Fahim. Friction and wear behavior of polyetherimide composites in various wear modes. *Wear*, 249(8):715–726, 2001.
- [13] J Bijwe and R Rattan. Carbon fabric reinforced polyetherimide composites: Optimization of fabric content for best combination of strength and adhesive wear performance. *Wear*, 262(5-6):749–758, 2007.
- [14] A C Callan-Jones, P T Brun, and B Audoly. Self-similar curling of a naturally curved elastica. *Physical Review Letters*, 108(17):174302, 2012.
- [15] X Chen and X B Huang. Evaluating fabric pilling with light-projected image analysis. *Textile Research Journal*, 74(11):977–981, 2004.
- [16] I L Ciesielska-Wrobel and L Van Langenhove. The hand of textiles—definitions, achievements, perspectives—a review. *Textile Research Journal*, 82(14):1457–1468, 2012.

- [17] W D Cooke. 2—the influence of fibre fatigue on the pilling cycle part i: Fuzz fatigue. *Journal of the Textile Institute*, 73(1):13–19, 1982.
- [18] W D Cooke. 10—the influence of fibre fatigue on the pilling cycle part ii: Fibre entanglement and pill growth. *Journal of the Textile Institute*, 74(3):101–108, 1983.
- [19] W D Cooke. 21—fibre fatigue and the pilling cycle part iii: Pill wear-off and fabric attrition. *Journal of the Textile Institute*, 75(3):201–211, 1984.
- [20] W D Cooke. Pilling attrition and fatigue. *Textile Research Journal*, 55(7):409–414, 1985.
- [21] W D Cooke and D F Arthur. 10—a simulation model of the pilling process. *Journal of the Textile Institute*, 72(3):111–120, 1981.
- [22] I Daubechies. Orthonormal bases of compactly supported wavelets. *Communications on pure and applied mathematics*, 41(7):909–996, 1988.
- [23] Z Deng, L Wang, and X Wang. An integrated method of feature extraction and objective evaluation of fabric pilling. *The Journal of The Textile Institute*, 102(1):1–13, 2011.
- [24] H M Elder and A S Ferguson. 18—the abrasion-resistance of some woven fabrics as determined by the accelerotor abrasion tester. *Journal of the Textile Institute*, 60(7):251–267, 1969.
- [25] P X Gao, Y Ding, W J Mai, W L Hughes, C S Lao, and Z L Wang. Conversion of zinc oxide nanobelts into superlattice-structured nanohelices. *Science*, 309(5741):1700–1704, 2005.
- [26] J D Gates. Two-body and three-body abrasion: a critical discussion. *Wear*, 214(1):139–146, 1998.
- [27] S J Gerbode, J R Puzey, A G McCormick, and L Mahadevan. How the cucumber tendril coils and overwinds. *Science*, 337(6098):1087–1091, 2012.
- [28] D Gintis and E J Mead. The mechanism of pilling. *Textile Research Journal*, 29(7):578–585, 1959.
- [29] R E Goldstein, A Goriely, G Huber, and C W Wolgemuth. Bistable helices. *Physical Review Letters*, 84(7):1631, 2000.
- [30] A Goriely. *The mathematics and mechanics of biological growth*, volume 45. Springer, 2017.
- [31] A Goriely and M Tabor. New amplitude equations for thin elastic rods. *Physical Review Letters*, 77:3537–3540, Oct 1996.
- [32] A Goriely and M Tabor. Nonlinear dynamics of filaments i. dynamical instabilities. *Physica D: Nonlinear Phenomena*, 105(1):20–44, 1997.
- [33] A Goriely and M Tabor. Nonlinear dynamics of filaments. iii. instabilities of helical rods. *Proceedings of the Royal Society of London. Series A: Mathematical, Physical and Engineering Sciences*, 453(1967):2583–2601, 1997.
- [34] A Goriely and M Tabor. Spontaneous helix hand reversal and tendril perversion in climbing plants. *Physical Review Letters*, 80(7):1564–1567, 1998.
- [35] S Goyal, N C Perkins, and C L Lee. Nonlinear dynamics and loop formation in kirchhoff rods with implications to the mechanics of dna and cables. *Journal of Computational Physics*, 209(1):371–389, 2005.
- [36] MATLAB User’s Guide. The mathworks. *Inc., Natick, MA*, 5:333, 1998.
- [37] K H Hong, S C Kim, T J Kang, and K W Oh. Effect of abrasion and absorbed water on the handle of nonwovens for disposable diapers. *Textile research journal*, 75(7):544–550, 2005.

- [38] C H Hsi, R R Bresee, and P A Annis. Characterizing fabric pilling by using image-analysis techniques. part i: Pill detection and description. *Journal of the Textile Institute*, 89(1):80–95, 1998.
- [39] J S Huang, J Liu, B Kroll, K Bertoldi, and D R Clarke. Spontaneous and deterministic three-dimensional curling of pre-strained elastomeric bi-strips. *Soft Matter*, 8(23):6291–6300, 2012.
- [40] ASTM International. Astm d3512 / d3512m-16, standard test method for pilling resistance and other related surface changes of textile fabrics: Random tumble pilling tester. *West Conshohocken, PA*, 2016.
- [41] ASTM International. Astm d4970/d4970m-16. standard test method for pilling resistance and other related surface changes of textile fabrics: Martindale tester. *West Conshohocken, PA*, 2016.
- [42] B S Jeon, J H Bae, and M W Suh. Automatic recognition of woven fabric patterns by an artificial neural network. *Textile Research Journal*, 73(7):645–650, 2003.
- [43] B Joos and M S Duesbery. The peierls stress of dislocations: an analytic formula. *Physical Review Letters*, 78(2):266, 1997.
- [44] N A Kalebek and O Babaarslan. A study of abrasion and frictional behaviour of nonwoven interlining produced with different coating methods. *Fibers and Polymers*, 12(3):371, 2011.
- [45] N A Kalebek and O Babaarslan. Fiber selection for the production of nonwovens. *Non-woven Fabrics*, page 1, 2016.
- [46] T J Kang, D H Cho, and S M Kim. Objective evaluation of fabric pilling using stereovision. *Textile research journal*, 74(11):1013–1017, 2004.
- [47] S Kim and C K Park. Evaluation of fabric pilling using hybrid imaging methods. *Fibers and Polymers*, 7(1):57, 2006.
- [48] S C Kim and T J Kang. Image analysis of standard pilling photographs using wavelet reconstruction. *Textile Research Journal*, 75(12):801–811, 2005.
- [49] A Konda, L C Xin, M Takadera, Y Okoshi, and K Toriumi. Evaluation of pilling by computer image analysis. *Journal of the textile Machinery Society of Japan*, 36(3):96–107, 1990.
- [50] A Kumar and T J Healey. A generalized computational approach to stability of static equilibria of nonlinearly elastic rods in the presence of constraints. *Computer Methods in Applied Mechanics and Engineering*, 199(25-28):1805–1815, 2010.
- [51] C Kuo, C Shih, C Huang, and Y Wen. Image inspection of knitted fabric defects using wavelet packets. *Textile Research Journal*, 86(5):553–560, 2016.
- [52] M Latifi and H S Kim. Characterizing fabric pilling due to fabric-to-fabric abrasion. *Textile Research Journal*, 71(7):640–644, 2001.
- [53] J H Lin, C W Lou, C H Lei, and C Y Lin. Processing conditions of abrasion and heat resistance for hybrid needle-punched nonwoven bag filters. *Composites Part A: Applied Science and Manufacturing*, 37(1):31–37, 2006.
- [54] S Lin and B G Xu. Evaluating fabric fuzziness using wavelet transforms. *Optical Engineering*, 39, 2000.
- [55] J Liu, J S Huang, T X Su, K Bertoldi, and D R Clarke. Structural transition from helices to hemihelices. *PLoS One*, 9(4):e93183, 2014.

- [56] S P Liu, Z W Yao, K Chiou, S I Stupp, and M O De La Cruz. Emergent perversions in the buckling of heterogeneous elastic strips. *Proceedings of the National Academy of Sciences*, 113(26):7100–7105, 2016.
- [57] S R Malkan. Improving the use of polyolefins in nonwovens. In *Polyolefin Fibres*, pages 285–311. Elsevier, 2017.
- [58] ABAQUS User’s Manual and II Volume. Version 6.4. *Abaqus Inc*, 1080, 2003.
- [59] T McMillen and A Goriely. Tendril perversion in intrinsically curved rods. *Journal of Nonlinear Science*, 12(3):241–281, 2002.
- [60] K R Mecklenburg and R J Benzing. Testing for adhesive wear. In *Selection and Use of Wear Tests for Metals*. ASTM International, 1976.
- [61] N A Memon. Nonwovens: global demand is expected to reach 9.1 million tonnes in 2017. *Korea: technical textiles & nonwovens*, 233:217–174, 2016.
- [62] N H Mendelson. Helical bacillus subtilis macrofibers: morphogenesis of a bacterial multicellular macroorganism. *Proceedings of the National Academy of Sciences*, 75(5):2478–2482, 1978.
- [63] M Misiti, Y Misiti, G Oppenheim, and J Poggi. Wavelet toolbox. *The MathWorks Inc., Natick, MA*, 15:21, 1996.
- [64] S Neukirch, G H M van der Heijden, and J M T Thompson. Writhing instabilities of twisted rods: from infinite to finite length. *Journal of the Mechanics and Physics of Solids*, 50(6):1175–1191, 2002.
- [65] J F Nye. Some geometrical relations in dislocated crystals. *Acta metallurgica*, 1(2):153–162, 1953.
- [66] S D Olson, S Lim, and R Cortez. Modeling the dynamics of an elastic rod with intrinsic curvature and twist using a regularized stokes formulation. *Journal of Computational Physics*, 238:169–187, 2013.
- [67] B O’Neill. *Elementary Differential Geometry*. Elsevier, 2006.
- [68] N Özdil, G Ö Kayseri, and G S Mengüç. Analysis of abrasion characteristics in textiles. In *Abrasion resistance of materials*. IntechOpen, 2012.
- [69] S Palmer and X G Wang. Objective classification of fabric pilling based on the two-dimensional discrete wavelet transform. *Textile Research Journal*, 73(8):713–720, 2003.
- [70] S Palmer and X G Wang. Evaluating the robustness of objective pilling classification with the two-dimensional discrete wavelet transform. *Textile Research Journal*, 74(2):140–145, 2004.
- [71] P Pieranski, J Baranska, and A Skjeltorp. Tendril perversion — a physical implication of the topological conservation law. *European Journal of Physics*, 25:613–621, 2004.
- [72] K Porter. Nonwoven fabrics: Growth point in a depressed textile industry. *Physics in Technology*, 8(5):204, 1977.
- [73] Y Rong, D He, and Y C Lin. Rapid detection method for fabric defects based on machine vision. In *2010 International Conference on Computer Application and System Modeling (ICCA SM 2010)*, volume 10, pages V10–662. IEEE, 2010.
- [74] T Savin, N A Kurpios, A E Shyer, P Florescu, H Y Liang, L Mahadevan, and C J Tabin. On the growth and form of the gut. *Nature*, 476(7358):57–62, 2011.
- [75] J Ukponmwan, A Mukhopadhyay, and K N Chatterjee. Pilling. *Textile progress*, 28(3):1–57, 1998.

- [76] G H M van der Heijden, S Neukirch, V G A Goss, and J M T Thompson. Instability and self-contact phenomena in the writhing of clamped rods. *International Journal of Mechanical Sciences*, 45(1):161–196, 2003.
- [77] H Wada. Hierarchical helical order in the twisted growth of plant organs. *Physical Review Letters*, 109(12):128104, 2012.
- [78] D D Wang, M D Thouless, W Lu, and J R Barber. In-situ observations of abrasion mechanisms of nonwoven fabric. *Wear*, 432:202945, 2019.
- [79] J S Wang, G Wang, X Q Feng, T Kitamura, Y L Kang, S W Yu, and Q H Qin. Hierarchical chirality transfer in the growth of towel gourd tendrils. *Scientific Reports*, 3:3102, 2013.
- [80] X Y Wang, R H Gong, Z Dong, and I Porat. Abrasion resistance of thermally bonded 3d nonwoven fabrics. *Wear*, 262(3-4):424–431, 2007.
- [81] J J Wie, K M Lee, T H Ware, and T J White. Twists and turns in glassy, liquid crystalline polymer networks. *Macromolecules*, 48(4):1087–1092, 2015.
- [82] B J Xin, J L Hu, and H J Yan. Objective evaluation of fabric pilling using image analysis techniques. *Textile Research Journal*, 72(12):1057–1064, 2002.
- [83] B G Xu. Identifying fabric structures with fast fourier transform techniques. *Textile Research Journal*, 66(8):496–506, 1996.
- [84] B G Xu. Instrumental evaluation of fabric pilling. *The Journal of The Textile Institute*, 88(4):488–500, 1997.
- [85] Y Yang, Y J Zhang, and Z X Wei. Supramolecular helices: chirality transfer from conjugated molecules to structures. *Advanced Materials*, 25(42):6039–6049, 2013.
- [86] M Yao, W R Yu, W L Xu, and B G Xu. Evaluating fabric fuzziness using laser range sensing. *Optical Engineering*, 47(1):013603, 2008.
- [87] J M Zhang, X G Wang, and S Palmer. Objective pilling evaluation of wool fabrics. *Textile research journal*, 77(12):929–936, 2007.
- [88] O C Zienkiewicz, R L Taylor, P Nithiarasu, and J Z Zhu. *The finite element method*, volume 3. McGraw-hill London, 1977.